UC Irvine

UC Irvine Electronic Theses and Dissertations

Title

Impact of Low-Resolution Quantization in Oversampled Massive MIMO Receivers

Permalink

https://escholarship.org/uc/item/5cw1s8n7

Author

Rao, Shilpa

Publication Date

2021

Peer reviewed|Thesis/dissertation

UNIVERSITY OF CALIFORNIA,
IRVINE

Impact of Low-Resolution Quantization in Oversampled Massive MIMO Receivers

DISSERTATION

submitted in partial satisfaction of the requirements
for the degree of

DOCTOR OF PHILOSOPHY

in Electrical Engineering

by

Shilpa Rao

Dissertation Committee:
Professor A. Lee Swindlehurst, Chair
Professor Ender Ayanoglu
Professor Hamid Jafarkhani

2021

DEDICATION

To my family for their infinite and unconditional love

TABLE OF CONTENTS

LIST OF FIGURES

LIST OF TABLES

ACKNOWLEDGMENTS

I would like to wholeheartedly thank Prof. Lee for taking me on as his student and giving me the opportunity to write this dissertation. I have been immensely fortunate to receive his guidance and I am grateful for his unlimited patience. His astute observations have enabled me to progress as a researcher, and his kindness has helped me grow as a person. I have benefited greatly from his prompt and acute feedback. His efforts to nurture our group and to encourage collaboration among individuals are truly admirable. I am thankful for his words of wisdom in times of need, and the lessons he imparted to me are ones I will carry with me for life.

I am honored to have had the opportunity to work with Prof. Gonzalo. His technical expertise, passion and disciplined work ethic has been inspiring to me. I am grateful for the thought-provoking conversations with him, his invaluable contributions to our group and his inputs which greatly helped improve the quality of my work.

I would like to express my gratitude towards Amine who patiently motivated and guided me during my early Ph.D. days. His encouragement and supervision has been vital to my progress. I will forever remember his mentorship and I thank him for his generosity in lending me a copy of his own dissertation. My sincerest thanks also to Dr. Alexei and Dr. Hong at Nokia Bell Labs for hiring me, for teaching me the tricks of the trade, and for giving me an unforgettable experience during my internship.

Several friends and colleagues have made my graduate life awesome. I consider it a great privilege to have a colleague and friend in Hessam Pirzadeh. I thank him for his efforts in coauthoring papers with me and for promptly responding to my texts at all times during the day. I have enjoyed our numerous discussions and the time we spent debugging each others' code. His ability to remain light-hearted even in times of setbacks has been a significant source of comfort to me. I have also learned a great deal from my friend Lu Liu who selflessly helped our group run codes efficiently. I admire her for being a compassionate friend and for keeping every conversation interesting with her witty sense of humor. I also thank Nicole, Deying and Gary for all the good times during our board game nights and tennis sessions. Thanks also to Van Ly and Kunchao for their valuable contributions to our group, Bao and Nanda for being available to grab innumerable cups of coffee with me over the years. Thank you, Mahitha and Manju, for your friendship and company, Isma and Roopesh for our many movie nights and numerous racquetball sessions.

VITA

Shilpa Rao

EDUCATION

Doctor of Philosophy in Electrical Engineering	**2021**
University of California, Irvine	*Irvine, CA*
Master of Science in Electrical Engineering (cum laude)	**2015**
Delft University of Technology	*Delft, Netherlands*
Bachelor of Engineering in Electronics & Communications	**2012**
Visvesvaraya Technological University	*Belgaum, India*

RESEARCH EXPERIENCE

Graduate Research Assistant	**2017–2021**
University of California, Irvine	*Irvine, CA*
Summer Intern	**2018**
Nokia Bell Labs	*Murray Hill, NJ*

TEACHING EXPERIENCE

Teaching Assistant, EECS 50: Discrete-time Signals & Systems	**2019**
University of California, Irvine	*Irvine, CA*
Teaching Assistant, EECS 152B: DSP Lab	**2020**
University of California, Irvine	*Irvine, CA*

REFEREED JOURNAL PUBLICATIONS

Channel estimation in one-bit massive MIMO systems: Angular versus unstructured models   **2019**
IEEE Journal of Selected Topics in Signal Processing

Massive MIMO channel estimation with low-resolution spatial sigma-delta ADCs   **2021**
IEEE Access

Direction finding with low-resolution spatial sigma-delta ADCs in the presence of modeling errors
Journal in preparation

REFEREED CONFERENCE PUBLICATIONS

Massive MIMO channel estimation with 1-bit spatial sigma-delta ADCs   **May 2019**
IEEE Int. Conf. on Acoustics, Speech and Signal Processing, Brighton UK

Spatial sigma-delta massive MIMO: Improved channel estimation and achievable rates   **Oct. 2020**
Asilomar Conf. on Signals, Systems, and Computers, Pacific Grove, CA

ABSTRACT OF THE DISSERTATION

Impact of Low-Resolution Quantization in Oversampled Massive MIMO Receivers

By

Shilpa Rao

Doctor of Philosophy in Electrical Engineering

University of California, Irvine, 2021

Professor A. Lee Swindlehurst, Chair

Massive multiple-input multiple-output (MIMO) technology employs arrays with a large number of antennas, of the order of 100 or more, at the base station (BS) to meet the data rate and user demands of next generation wireless systems. To cope with the power consumption problem due to an increased number of receive antennas, the idea of equipping one-bit analog-to-digital converters (ADCs) at the base station has been proposed. This thesis will focus on the topic of channel estimation which is key to exploiting the potential gains of massive MIMO.

In this first part of the thesis, performance bounds on the channel estimation of one-bit millimeter-wave (mmWave) massive MIMO receivers for different types of channel models are established. The Cramér-Rao bound (CRB), which sets a benchmark for the design of channel estimators, is considered for both a structured channel model for a single user where the channel is composed of a superposition of multipaths characterized by path delays and directions-of-arrival (DOAs), and an unstructured channel model where the channel is a generic FIR filter. The Bayesian CRB when the array response is imperfectly known and is affected by perturbations in the sensor pattern or position is also derived. The CRBs are evaluated numerically and the effects of various system parameters on the CRB are studied. The results show that increasing the bandwidth or the oversampling factor decreases the

estimation error variance due to improved temporal resolution.

Spatial oversampling could also be used, instead of, or in addition to temporal oversampling. In the second part of this dissertation, spatial Sigma-Delta ($\Sigma\Delta$) architectures, to shape the quantization noise away from users in some angular sector, are considered. A linear minimum mean squared error (LMMSE) channel estimator based on the so-called Bussgang decomposition is developed and the uplink achievable rate with linear receivers is analyzed. Finally, the problem of direction finding when the BS is equipped with a rectangular antenna array and spatial $\Sigma\Delta$ ADCs is considered. The impact of array response and noise modeling errors on the estimation errors of Bartlett beamformers and the multiple signal classification (MUSIC) algorithm is studied.

Chapter 1

Introduction

A world without mobile connectivity has become unimaginable. Over the last several years, there has been an extreme densification of nodes per unit area and an exponential growth in mobile traffic. Over 60% of the global population is connected to the internet with approximately half of the website traffic arising from mobile users. This proliferation of mobile devices has enabled us to usher in a new era of remote work with millions of us teleworking and participating in online classes. The large-scale use of data intensive and low latency applications like video and cloud computing has solidified the need for reliable and efficient techniques of mobile communications to improve the capacity. Nevertheless, the rapid growth of products and services could not have occurred without significant developments in the fields of estimation and detection theory, information theory and digital communications. The aim of this dissertation is to give a better understanding of *massive multiple-input multiple-output (MIMO) systems*- a key technology that meets the traffic demands of next generation wireless systems. In this dissertation, the practical implementations of massive MIMO and their effect on parameter estimation, a problem that is at the heart of many signal processing applications, will be discussed.

1.1 Background and Prior Work

MIMO technology, emerged from research in the 1990s [1] and uses multiple transmitting and receiving antennas to exploit multipath propagation. It has become an essential element of modern wireless standards including WiFi and Long Term Evolution (LTE). Multiple antennas allow for multiple spatial dimensions to become available and the entries of the channel matrix exhibit enough statistical independence to increase the spectral efficiency [2, 3]. In multi-user version of MIMO (MU-MIMO), each base station (BS) can communicate with several users concurrently. However, the initial implementations of MU-MIMO had BSs equipped with a relatively small number of antennas (less than 10) and so, the extent to which MIMO could be leveraged was limited.

In order to further improve the gains in spectral efficiency, the concept of massive MIMO was proposed in [4]. Massive MIMO refers to a system in which the BS is equipped with a large number of antennas, 100 or more, much larger than the number of users/terminals active at any point. Without requiring additional bandwidth, massive MIMO has the potential to increase the data rate by orders of magnitude while simultaneously requiring lesser power [5, 6]. The main advantages are:

- *Spectral efficiency:* Enormous improvements in spectral efficiency due to spatial multiplexing.

- *Energy efficiency:* Ability to generate narrow focused beams towards users, therefore improving the energy efficiency.

- *Effects of small-scale fading:* Small-scale randomness is averaged out due to the law of large numbers, brought about by the vast spatial diversity. The asymptotics of random matrix theory smooth out the channel responses and thus, the effects of uncorrelated noise are virtually eliminated.

- *Simple signal processing:* Since the number of active users compared to the number of antennas at the BS is small, their channels are quasi-orthogonal and even simple linear receivers like maximum ratio combining (MRC) and zero-forcing (ZF) receivers have near-optimal performance.

Other technologies have also been considered to increase the data throughput and coverage. For instance, cell shrinking allows for the reuse of spectrum across a geographical area since the number of users vying for BS resources decreases. In cell-free massive MIMO [7, 8], the antennas are distributed over an area. These systems have a greater probability of coverage since they are able to exploit their diversity against shadow fading.

Going to *millimeter-wave (mmWave)* frequencies is another way to achieve dramatic gains in data rate and capacity [9]. The main reason is that vast amounts of unused spectrum are available at frequencies in the range 30-300 GHz that can be used to support high data-rate transmissions [10]. However, mmWave signals suffer from rather hostile propagation effects and the severe signal attenuation encountered at these frequencies reduce the effective communication distance, making them more suitable for covering small cells that span a few hundred meters. The strong path loss, atmospheric absorption, the low penetration in concrete, and diffraction around objects make mmWave communication unsuitable for non-light-of-sight (NLOS) scenarios. Specular propagation means that mmWave channels are characterized by the directions-of-arrival (DOA) of the prominent line-of-sight (LOS) paths.

The combination of mmWave and massive MIMO technologies can have a symbiotic effect [11]. Since the antenna array size is proportional to the wavelength, communication at mmWave frequencies implies that a large number of antennas can be accommodated in a limited physical space. Furthermore, the ability to generate highly focused beams with massive MIMO can help in overcoming the mmWave path loss. Both indoor and outdoor implementations of mmWave [12, 13] and of massive MIMO [14, 15] are promising.
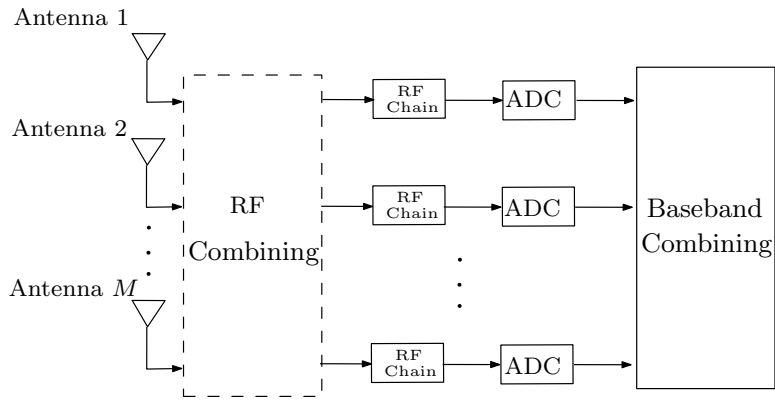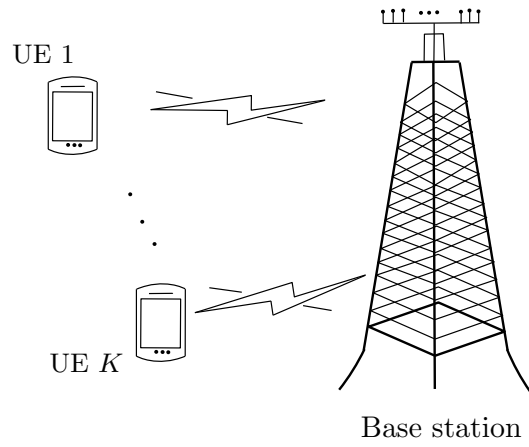
Figure 1.1: Massive MIMO uplink system model.
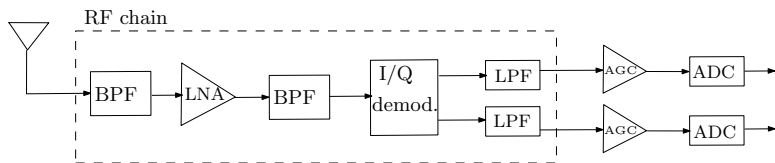
Figure 1.2: Single RF chain.

Although physically feasible, the notion of massive MIMO poses some difficulties, particularly in terms of communication hardware aspects. Consider for example, the massive MIMO uplink system model in Fig. 1.1 and Fig. 1.2. In the uplink, the receiver chain consists of an RF combiner in mmWave applications, an RF chain equipped with band pass filters (BPFs) and low pass filters (LPF), low-noise amplifiers (LNAs), demodulator, and analog-to-digital converters (ADCs) before the digital baseband signal processing. The mapping of analog to digital data (or vice versa) is performed by the ADC (or digital-to-analog convertor DAC). The circuit is composed of a sample-and-hold device for time-domain conversion and a quantizer for amplitude conversion. An ADC with a sampling frequency of, say, f_s Hz and resolution of b bits has $2^b f_s$ conversion steps per second and 2^b quantization levels. The exorbitant power consumption of the ADCs/DACs for sampling rates higher than 100 MHz poses a crucial problem for mmWave systems and is a bottleneck in RF chains [16]. Although deployment of a large number of antennas is required to overcome the path loss issue, equipping each antenna with expensive fully digital beamformers is unfeasible and conventional analog phase shifters [17, 18, 19] or hybrid structures [20, 21, 22, 23] where groups of antennas share an ADC/DAC are better suited. However, the implementation for wideband systems is complex since phase shifters have to be designed for each frequency band. An alternative to analog or hybrid architectures is to use low-resolution ADCs/DACs that maintain an acceptable power budget. In the extreme case, one-bit ADCs/DACs (zero-threshold comparators) may be used since they are simple to implement [24]. One-bit converters have negligible power consumption compared to other components in the front-end- for instance, a one-bit ADC operating at sampling frequency 240GS/s consumes around 10mW [25]. An additional benefit is that the hardware complexity is simplified since an automatic gain control (AGC) is not needed. The low SNR capacity gap between one-bit and infinite resolution ADC is only 1.96dB [26] and an inevitable error floor at high SNRs [27] because the quantization error does not reduce with the SNR. However, the performance loss from coarse one-bit quantization can be compensated for by increasing

the number of antennas [28, 29, 30].

The notion of one-bit quantization has challenged the way we think about communications. There has been a surge of research into one-bit converters in recent years with focus on the impact of nonlinearity on the performance of communication systems. For instance, the optimal symbol constellation is discrete- 2-PAM is capacity achieving for single-input single-output (SISO) real-valued Gaussian channel whereas QPSK is optimal for complex valued Gaussian channels [16]. Capacity bounds are derived in [31] for channel state information (CSI) available at both the transmitter and receiver, the uplink throughput when the BS is equipped with one-bit ADCs is analyzed in [32], a near maximum-likelihood (ML) detector is devised in [33], linear detectors in [29, 32], precoding [34, 35, 36] and the use of dithered signals [37, 38]. The impact on spectral and energy efficiency of massive MIMO systems equipped with one-bit converters have been analyzed in [27, 39, 40, 41, 42, 43, 44, 45, 46]. The combination of low and high resolution ADCs has been studied and shown to have a performance similar to that of unquantized systems [47, 48].

The focus of this dissertation is to study the problem of estimation using low-resolution quantizers. The inference of information from a given set of data is the main objective in many signal processing systems. *Channel estimation* is an important topic in wireless communications and refers to estimating the propagation path values that represent the combined effects of scattering, fading and path loss. Massive MIMO based channel estimation using one-bit ADCs have been studied in [33] using ML, in [27, 38, 49] for frequency-flat channels, for frequency-selective channels in [27, 50], and for wideband systems in [48, 51]. Some recent works [52, 53, 54, 55] study non-linear and learning-based detection methods foregoing the channel estimation stage. Since the scattering environment at mmWave frequencies is not dense but rather sparse with LOS and a few reflected propagation paths contributing to the effective channel, much of the work is focused on direction-of-arrival (DOA) based channel estimation. Whereas mmWave channel estimation methods that exploit the sparsity in the

6

delay/angle domain have been studied in [20, 56, 57, 58, 59, 60, 61], mmWave estimation aided with one-bit ADCs have been proposed in [62, 63, 64, 65]. More recent works study the problem of DOA estimation with one-bit ADCs [66, 67, 68, 69, 70, 71].

Despite the development of several robust estimators, several questions come to mind. How close are the estimated parameters to the true values? What is the minimum variance that an estimator can attain? The formal theory of statistical inference attempts to answer such questions, and was developed by Fisher who introduced the theory of ML [72]. The main reason for the popularity of ML is its "asymptotic efficiency" i.e. its error variance decreases to a minimum value as the signal-to-noise (SNR) or the number of observations goes to infinity. The concept of "efficient" estimators, though, is related to the presence of some performance bounds that determine how good an estimator can be. If an algorithm can achieve a certain performance bound, then no other estimator can do better and the existence of such a bound indicates the impossibility of achieving a lower error than the one predicted by the bound itself. It also reveals the complex inter-dependencies of the parameters at hand and can help us design estimators that can attain the approximate bound in some sense. Several such bounds exist, one of which is the *Cramér-Rao bound* (CRB) [73, 74]. In [75], a lower bound on the Fisher information matrix (FIM) for the exponential family of distributions is derived and the ML estimator based on the "pessimistic" CRB for the DOA parameter is derived in [76]. In [77] and [78], the CRB for the channel parameterized by DOAs and path gains is derived when the channel and the array responses are frequency flat. However, in the above-mentioned DOA-based channel models, it is assumed that the inter-element time delay between antennas in the array is small compared to the inverse signal bandwidth. For mmWave massive MIMO systems, this assumption will typically not be true. This effect, sometimes referred to as (beam) "squint", has been observed to cause a serious mismatch in the array response, and if ignored can significantly degrade performance [79, 80, 81, 82]. The above works do not consider oversampling and the modeling errors that are inevitable in any estimation process are ignored. This will be the focus of

the first part of this dissertation.

The research into one-bit ADCs has revealed an important message- that temporal *oversampling*, or sampling the converter at a frequency higher than the Nyquist rate, can alleviate some of the loss due to coarse quantization. In fact, Nyquist-rate sampling is not necessarily optimal and higher capacity rates can be achieved by oversampling [35, 36, 83, 84, 85, 86, 87, 88, 89, 90]. A well-known technique that combines one-bit quantization and oversampling is the $\Sigma\Delta$ ADC, which to date has primarily found application in ultrasound imaging, automotive radar and pulse-coded modulation for audio encoding. It consists of an over-sampled modulator, responsible for digitization of the analog signal, followed by a negative feedback loop that shapes the quantization noise with a simple high-pass filter. The quantization noise can then be removed in favor of the desired signal using a digital lowpass filter and decimation. The temporal $\Sigma\Delta$ architecture has been extensively studied [91, 92, 93], and higher-order implementations exist that can provide additional frequency-selective noise shaping. The use of $\Sigma\Delta$ ADCs in parallel architectures for MIMO systems has been studied in [94, 95]. The Bussgang theorem [96] is used to analyze the noise shaping effect of temporal $\Sigma\Delta$ modulators, and Price's theorem [97] is used in [98] to predict the noise floor. Higher-resolution ADCs and temporal oversampling can improve performance with only a moderate increase in power consumption, but they significantly increase the required fron-thaul throughput compared with one-bit quantization.

While temporal $\Sigma\Delta$ systems have been studied for decades, there is relatively little work on corresponding spatial implementations. This will be the focus of the second part of this dissertation. Only recently has the noise shaping characteristics of first and second-order spatial and cascaded space-time $\Sigma\Delta$ architectures been studied for a few array processing applications. In particular, applications have been considered for massive MIMO [99, 100, 101, 102, 103], phased arrays [104, 105], interference cancellation [95], and spatio-temporal $\Sigma\Delta$ circuit implementations [106, 107]. Only [108] has studied channel estimation for spatial

8

$\Sigma\Delta$ massive MIMO systems, and the approach of [108, 109] was limited to estimating the angles of arrival and departure for a rank-one line-of-sight channel.

1.2 Summary of Contributions

As mentioned earlier, although CRBs for channel estimation with one-bit ADCs were considered in [75, 76, 77, 78], these works ignore oversampling and modeling errors, and the squint effect. The main contributions on this topic are summarized below:

- Channel models that are either "structured" (DOA-based, arbitrary delays) or "unstructured" (FIR, uniformly-spaced delays) are considered, and the resulting CRBs for the channel estimates are compared. Under the structured channel model, it is assumed that the channel is parameterized by the multipath fading coefficient, the DOA, and the delay associated with each of the paths.

- Perturbations to the array response when the array response does not exactly match the assumed array model will be taken into account, similar to the array perturbation studies of [110, 111, 112]. In particular, the level of array calibration accuracy needed for DOA-based methods to maintain their advantage compared with less parsimonious unstructured models is of interest.

- Under the unstructured model, the channel is modeled as having a finite duration impulse response composed of a discrete number of arbitrary delays. The squint effect, where for wideband signals the time delay from one end of the array to the other cannot simply be represented as a phase shift, is also taken into account. Incorporating these temporal shifts is important because the end-to-end delay for the antenna array is of the same order as the symbol duration.

- A dictionary-based channel model used in the compressive sensing literature [20, 57, 63] is also considered. The dictionary is based on a discrete set of DOAs and path delays obtained from a grid, where the grid size is greater than the number of antennas. This formulation is commonly used in mmWave channel estimation since compressive sensing based algorithms which exploit the underlying sparse multipath structure can be used. A "dictionary mismatched" channel model is considered, where the multipath DOAs and delays are matched to the nearest grid point and the difference between the dictionary and the true source parameters, or the grid mismatch, are parameters to be estimated.

- A number of numerical experiments are performed to evaluate the CRBs, and a comparison of the structured, unstructured and dictionary-based channels as a function of the SNR is performed. The effects of perturbation, bandwidth, the channel delay-tap length, and the number of receive antennas on the CRBs of the one-bit quantized system are also studied. Comparisons with the CRB obtained when there is no quantization error are included. The numerical results provide insight into the relative impact of the various factors that influence of the channel estimate, including the precision of the array calibration, the model parsimony, the one-bit quantization, size of the array, SNR, bandwidth, etc.

The second part of this dissertation is the analysis of massive MIMO systems with first-order one-bit or two-bit spatial $\Sigma\Delta$ ADCs. The initial results on the channel estimation problem were derived using a vector-wise Bussgang decomposition similar to the analysis for standard one-bit quantization in [27]. However, as shown in Chapter 4, this approach leads to a mathematical model in which the quantization error vector is defined to be uncorrelated with the input vector to the $\Sigma\Delta$ quantizer, which is not consistent with the traditional definition of quantization noise. A more meaningful definition of the quantization noise is to use an element-wise implementation of the Bussgang decomposition as defined in [103]

in order to find an equivalent linear signal-plus-quantization-noise model. This approach explicitly takes into account the spatial correlation between the quantized outputs of the $\Sigma\Delta$ ADC array.

- An optimal linear minimum mean squared error (LMMSE) channel estimator is developed. The channel model also includes the impact of mutual coupling, including also the fact that the noise becomes spatially correlated when the receiver antennas are closely spaced.

- The structure of the $\Sigma\Delta$ array is exploited to find a recursive solution for the covariance matrices required to compute the LMMSE channel estimate, and a practical algorithm is derived for doing so.

- The analytical expressions for the resulting covariance matrix of the channel estimation error is derived. The analysis can be extended for a $\Sigma\Delta$ array implemented with two-bit quantization, and similar extensions are possible for higher resolution ADCs. The resulting estimators have low complexity and the simulated estimation error closely matches the derived analytical expressions.

- The spectral efficiency of one-bit $\Sigma\Delta$ arrays was recently analyzed in [103, 113] with and without mutual coupling, respectively, but only for the case where the channel is perfectly known. The analysis of [103, 113] is extended to derive a lower bound on the uplink achievable rate using the maximal ratio combining (MRC), zero-forcing (ZF) and LMMSE receivers when implemented with imperfect channel state information (CSI) obtained using the LMMSE channel estimate.

Finally, the problem of direction finding with $\Sigma\Delta$ ADCs is studied. More specifically, the estimation of elevation and azimuth angles when the BS is equipped with a rectangular array is considered. DOA estimation using one-bit ADCs and conventional beamforming

11

has been studied in [66], using sparse linear arrays [67, 68] and using compressed sensing measurements [69, 70]. In [71], the authors propose a DOA estimation method based on multiple signal classification (MUSIC) [114] by reconstructing the input covariance matrix from the covariance matrix of the one-bit quantized output. Most of the prior literature on mmWave channel estimation and DOA estimation with one-bit or few-bit ADCs focus on one-dimensional angle estimation using linear arrays [62, 67, 68, 71]. Although mmWave MIMO channel model based DOA estimation with these estimators were considered in [108, 109], the authors did not consider a planar BS array as in this case, their model ignored the presence of mutual coupling, and an analysis of the asymptotic estimation error was not carried out. The extension to the two-dimensional angular estimation is not straightforward for various wireless scenarios. For instance, antenna arrays are mounted on top of a tower in a typical sectorized cellular case and while the desired field of view is wide in the azimuth domain, it is relatively narrow in the elevation domain since most users are on the ground. Even in indoor settings, antenna arrays are mounted on a wall and most users are concentrated around a small angular sector in the elevation domain. Thus, a 2-D array architecture in which the spatial $\Sigma\Delta$ processing occurs only along the vertical dimension of the array is proposed. While the initial results on this problem were presented in [115], the system model did not include the effects of array response and additive noise perturbations. The main contributions are as follows:

- The signal model incorporates the fact that, in addition to having only a finite amount of noisy data available, there are often other sources of estimation error. For instance, the array response and the mutual coupling matrix (MCM) may be imprecisely known and the noise modeling may be inaccurate. Similar to the perturbation studies in [116, 117], the second-order statistics of the estimation error is dependent on the aggregate of these modeling errors.

- The covariance matrix of the estimation error of two well-known DOA estimation

12

methods, the conventional Bartlett beamformer and the MUSIC algorithm is derived. The closed-form expression for the covariance matrix of the estimation error is based on a first-order Taylor expansion of the objective function, assuming that the various sources of errors are uncorrelated.

- The simulation results show that the analysis is accurate and that the estimators based on the output of $\Sigma\Delta$ ADCs outperform those based on standard low resolution (1-2 bits) ADCs. The covariance matrix is simplified for the special case when array perturbations are the dominant sources of error and it is shown that for higher levels of array perturbation, the estimation error achieved with both one and two-bit $\Sigma\Delta$ ADCs is identical to that achieved with ideal ADCs.

- The analysis is simplified for the estimation of elevation angles only with uniform linear arrays (ULAs). The high-SNR error floor is shown to be significantly lower than that achieved with conventional 1-2 bits ADCs.

1.3 Outline of Dissertation

This dissertation is divided in two parts. In the first part, standard quantization is considered and performance bounds for channel estimation with one-bit ADCs are derived. In Chapter 2, the statistical theory of quantization and one-bit ADCs is described and the Cramér- Rao bound is introduced. Equivalent linear models to describe the one-bit operation. Narrowband and wideband channel models used in this dissertation are also listed.

In Chapter 3, CRB performance bounds on the channel estimation of one-bit mmWave massive MIMO receivers for different types of channel models, namely, the structured, unstructured, and dictionary-mismatched channels, are established. Numerical evaluations of the CRBs are performed and the different CRBs are compared.

In the second part of this dissertation, spatial implementations of the $\Sigma\Delta$ modulator are considered. In Chapter 4, the working of the well-known temporal $\Sigma\Delta$ modulator as well as its spatial analog are described. The extension of the Bussgang decomposition to spatial $\Sigma\Delta$ arrays is explained, along with the necessity for an element-wise Bussgang decomposition for a better modeling of the cross-correlation between the ADC input and the quantization noise. A description of the mutual coupling model used in Chapters 5 and 6 is provided.

In Chapter 5, the equivalent linear models developed in Chapter 4 are used to derive an LMMSE channel estimator. Linear receivers based on the LMMSE channel estimate are derived and expressions for the achievable spectral efficiency are derived. The performance of the low-resolution $\Sigma\Delta$ ADC array is evaluated and compared against that of standard low-resolution ADCs and infinite precision ADCs.

The problem of direction finding with a rectangular array employing spatial $\Sigma\Delta$ modulation is considered in Chapter 6. The asymptotic covariance matrix of the estimation error of both the elevation and azimuth angles of arrival estimated with two well-known algorithms- the Bartlett beamformer and the MUSIC algorithm, is derived. The system model also takes into account array perturbations and errors in modeling the spatial covariance matrix of the additive receiver noise.

Chapter 7 concludes the dissertation with a summary of chief findings and ideas for future expansion of this work are suggested.

Part I

Standard quantization: background and the Cramér-Rao bound

Chapter 2

Preliminaries and Analog-to-Digital Conversion

In this chapter, some concepts that will be used in the remainder of this dissertation will be reviewed. In particular, the commonly used notation will be listed followed by a discussion on the statistical theory of quantization and one-bit ADCs, the Cramér- Rao bound (CRB), and channel models that will be used throughout this dissertation.

2.1 Notation

The mathematical notation used frequently are listed here. Boldface lowercase $\mathbf{x}$ denotes a vector and boldface uppercase $\mathbf{X}$ denotes a matrix. $\mathbf{X}^T$, $\mathbf{X}^H$ and $\mathbf{X}^*$ are the transpose, Hermitian transpose, and conjugate of $\mathbf{X}$, respectively. $\mathrm{Tr}\,(\mathbf{X})$ is the trace of the matrix $\mathbf{X}$ and $\mathbf{X}^\dagger$ denotes pseudo-inverse of $\mathbf{X}$. The matrix $\mathbf{I}_M$ denotes a $M \times M$ identity matrix. The ith element of $\mathbf{x}$ and the (i,j)th entry of $\mathbf{X}$ are represented by x_i and $[\mathbf{X}]_{ij}$ respectively. The Hadamard (element-wise) product is represented by $\odot$, the Kronecker product by $\otimes$ and the

convolution operation by $\circledast$. The operation $\text{vec}(\cdot)$ denotes the vectorization operation, i.e. the stacking of the columns of a matrix one below the other. Real and imaginary parts are given by $\text{Re}(\cdot)$ and $\text{Im}(\cdot)$ respectively. $\mathbb{E}[\cdot]$ is the expectation operator. The ith row and jth column of the matrix $\mathbf{X}$ are given by $\mathbf{X}^{(i,)}$ and $\mathbf{X}^{(,j)}$ respectively. $\mathbf{X} \succeq \mathbf{Y}$ and $\mathbf{X} \succ \mathbf{Y}$ mean that $\mathbf{X} - \mathbf{Y}$ is positive semidefinite and positive definite respectively. The function $\text{mod}_M(\cdot)$ represents the modulo-M operator, and $\lfloor z \rfloor$ is the largest integer smaller than z. A circularly symmetric complex Gaussian vector with mean $\mathbf{a}$ and covariance matrix $\mathbf{B}$ is denoted by $\mathbf{x} \sim \mathcal{CN}(\mathbf{a}, \mathbf{B})$. The cumulative distribution function (cdf) and the standard normal density are given by $\Psi(x)$ and $\Psi'(x)$, respectively, and $p(x)$ denotes the probability density function (pdf) of x. $\text{Ci}(x) = \eta + \log(x) + \int_0^x \frac{\cos t - 1}{t} dt$ and $\text{Si}(x) = \int_0^x \frac{\sin t}{t} dt$ are the cosine and sine integral functions, respectively, where η is the Euler–Mascheroni constant. The unit step function is denoted by $u(\cdot)$, the Dirac-delta function is denoted by $\delta(\cdot)$ and the Kronecker-delta function is denoted by $\delta[\cdot]$.

2.2   Theory of quantization

Sampling and quantization are operations applied to analog signals in order to convert them into digital signals. A typical sampling and quantization system is shown in Fig. 2.1 and consists of a sample and hold circuit that operates with a sampling frequency f_s and converts the continuous time signal $x(t)$ to its discrete-time version $x[n]$ whereas the analog-to-digital (A/D) converter performs a discretization in amplitude. The digital-to-analog converter (DAC) performs the reverse operation: it converts the input digital signal to the analog domain. If the sampling theorem is satisfied i.e., the sampling frequency f_s is at least twice the highest bandwidth present in the signal $x(t)$ and if the number of quantization levels is large enough, the signal $y[n]$ is a good approximation of $x(t)$ as in Fig. 2.2 and the error introduced from quantization can be neglected. For coarse quantization, however, the
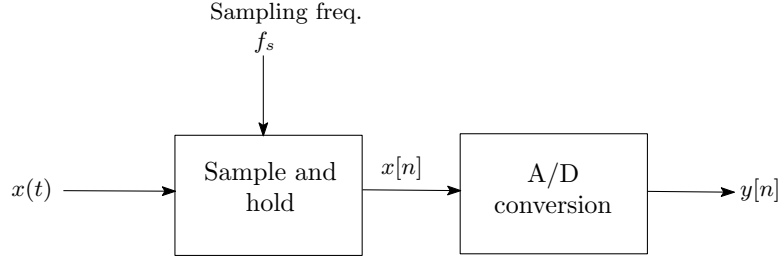
Figure 2.1: Sampling and quantization.
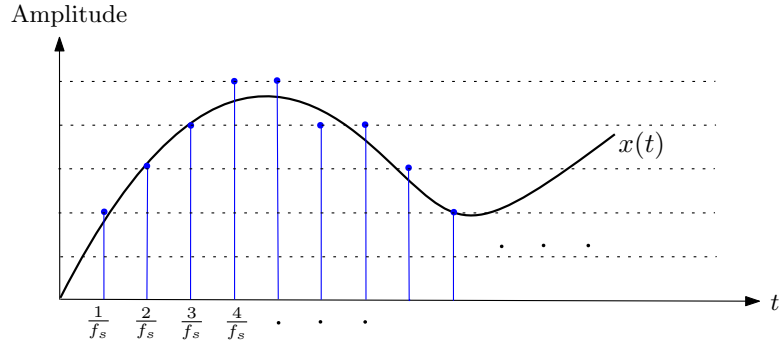
Figure 2.2: Example of an analog signal $x(t)$ and its digital version $y[n]$ shown in blue. The various quantization levels are illustrated with dotted lines.

effects of quantization are relevant and should be taken into consideration while designing communication systems. Practical ADCs present several undesired effects such as imperfect filtering and noise that can cause distortion and jitter. In this dissertation, only on the non-linear effects of quantization are studied and the filtering effects are taken to be part of the linear channel.

The quantization operation is represented by the function $\mathcal{Q}(\cdot)$. Fig. 2.3 shows two examples of regular quantizers- a uniform quantizer where the thresholds are uniformly spaced and a non-uniform regular quantizer where the threshold spacings are variable. A more general form not illustrated here is the non-regular quantizer that implements a many-to-one mapping and a quantization level may be assigned to several disjoint input-level intervals. However, this form is rarely preferred in practice since they are harder to implement. A regular quantizer is characterized by its resolution b bits, the 2^b quantization levels are represented by $\nu_i, i \in \{1, 2, \ldots, 2^b\}$ and the corresponding quantization intervals are $\left(\nu_i^{\text{lo}}, \nu_i^{\text{hi}}\right)$.

18
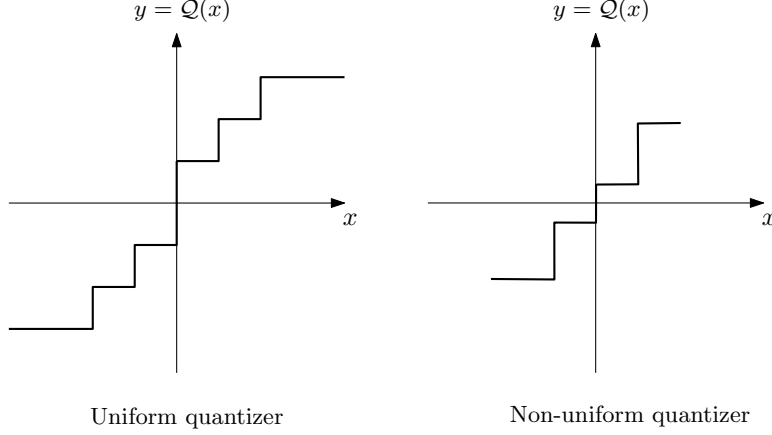
Figure 2.3: Uniform and non-uniform quantizers.
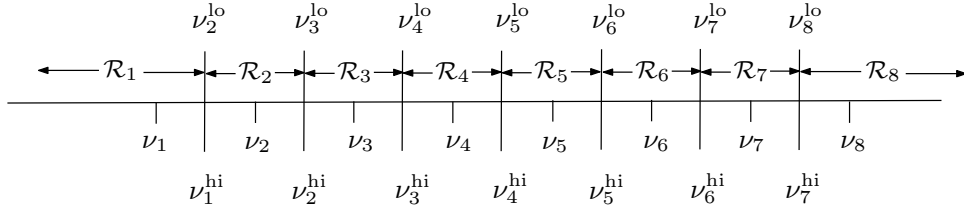
Figure 2.4: Quantization levels and regions.

The intervals satisfy $\nu_i^{\text{lo}} = \nu_{i-1}^{\text{hi}}$, $\nu_1^{\text{lo}} = -\infty$ and $\nu_{2^b}^{\text{hi}} = \infty$. Fig. 2.4 shows the example of a three-bit eight-level quantizer. Then, the general form of $\mathcal{Q}(x)$ is given by

$$\mathcal{Q}(x) = \sum_{i=1}^{2^b} \nu_i \left(u(x - \nu_i^{\text{hi}}) - u(x - \nu_i^{\text{lo}}) \right), \tag{2.1}$$

where $u(\cdot)$ is the unit-step function.

A commonly used approach to select the quantization levels and thresholds is to minimize the mean-squared error (MSE) or distortion between the input and the output of the quantizer given a number of quantization levels and was studied by Lloyd [118] and Max [119]. Mathematically, the MSE is given by

$$\mathbb{E}\left[(\mathcal{Q}(x) - x)^2\right] = \int_{-\infty}^{\infty} (\mathcal{Q}(x) - x)^2 \, p(x) dx = \sum_{i=1}^{2^b} \int_{\nu_i^{\text{lo}}}^{\nu_i^{\text{hi}}} (\nu_i - x)^2 \, p(x) dx, \tag{2.2}$$

where $p(x)$ is the pdf of x. Minimizing the above MSE with respect to ν_i and ν_i^{lo}, ν_i^{hi} leads

19

to the so-called *Lloyd-Max* conditions:

1. The boundaries of the quantization regions are given by the midpoints of the quantization levels.

$$\nu_i^{\text{lo}} = \nu_{i-1}^{\text{hi}} = \frac{\nu_i + \nu_{i-1}}{2}.$$

2. The quantization levels are the centroid points between two successive quantization decision thresholds

$$\nu_i = \frac{\int_{\nu_i^{\text{lo}}}^{\nu_i^{\text{hi}}} x p(x) dx}{\int_{\nu_i^{\text{lo}}}^{\nu_i^{\text{hi}}} p(x) dx}.$$

For a Gaussian random variable variable with variance σ_x^2, the above condition can be simplified to

$$\nu_i = \frac{\sigma_x}{\sqrt{2\pi}} \frac{\exp\left(-\frac{(\nu_i^{\text{lo}})^2}{2\sigma_x^2}\right) - \exp\left(-\frac{(\nu_i^{\text{hi}})^2}{2\sigma_x^2}\right)}{\Psi\left(\frac{\nu_i^{\text{lo}}}{\sigma_x}\right) - \Psi\left(\frac{\nu_i^{\text{hi}}}{\sigma_x}\right)}.$$

The above procedure results in a non-uniform quantization levels in general. Since the above non-linear equations have to be solved simultaneously, they are usually solved by an iterative Newton-type method with an arbitrary initialization of quantization levels. Table 2.1 shows the optimal quantization levels and thresholds obtained from the Lloyd-Max algorithm. Furthermore, the above equations also show that the output levels of the quantizer should vary as per the variations in the input, given by the standard deviation σ_x. That is, the quantizer should be designed such that it is responsive to a set of possible inputs rather than for a single set of input values, otherwise some of the input samples may get clipped. This is achieved with the help of an automatic gain control (AGC) which consists of a regulating circuit to maintain a suitable level of the output despite variations in the input level. It is assumed that the system is equipped with an instantaneous AGC and the topic

# bits	Gaussian R.V.		Laplacian R.V.	
	Q. levels	Thresholds	Q. levels	Thresholds
1	[-0.79,0.79]	[0]	[-0.70,0.70]	[0]
2	[-1.51,-0.45, 0.45,1.51]	[-0.98,0,0.98]	[-1.83,-0.42, 0.42,1.83]	[-1.12,0,1.12]
3	[-2.15,-1.34, -0.76,-0.24, 0.24,0.76, 1.34,2.15]	[-2.03,-1.18,-0.56,0, 0.56,1.18,2.03]	[-3.09,-1.67, -0.83,-0.23, 0.23,0.83, 1.67,3.09]	[-2.38,-1.25,-0.53,0, 0.53,1.125,2.38]

Table 2.1: Optimal Lloyd-Max quantization levels and thresholds for zero mean and unit variance Gaussian and Laplacian random variables.

of AGC calibration is ignored in this dissertation. Lloyd-max quantization is optimal for a fixed rate of encoding. For some applications like speech coding, it is more appropriate to minimize the mean squared error for a given level of entropy rather than for a given number of representation points, since the expected number of bits per symbol are governed by the entropy of the quantizer output [120]. This topic will not be covered in this dissertation.

A simple model for the quantizer is the additive noise model for which the output of the quantizer is defined as the input plus the quantization error. If a uniform quantizer is used and if the number of bits b is sufficiently high, the quantization error/noise $q[n] = y[n] - x[n]$ is assumed to be uniformly distributed in the range $[-\Delta/2, \Delta/2]$ and has a variance equal to $\sigma_q^2 = \frac{\Delta^2}{12}$ [121]. The statistical representation of quantization error under such a model is based on the assumptions that

- the quantization has a large number of levels and the step width is relatively small

- the quantizer rarely overloads

- the input pdf is smooth.

These assumptions are often not justified in practice. For instance, the quantizer may have only a few levels and the step width is typically not small, and the input may be

drawn from a discrete alphabet. Using the wrong quantization noise model can lead to poor characterization of the system. Thus, more accurate models are needed.

The Bussgang decomposition and Bussgang's theorem [96] are useful tools to analyze the non-linearity introduced by coarsely quantized ADCs like one-bit ADCs. The theorem essentially states that the cross-correlation between the input and output of a nonlinear device affected by Gaussian noise can be computed in terms of the input autocorrelation function. Bussgang's result holds for Gaussian signals and for any nonlinear function. The main result is summarized by Theorem 1.

Theorem 1 (Bussgang theorem): Let $x = f(t_1)$ and $z = g(t_2)$ be zero-mean complex Gaussian random variables and let $y = U(x)$ be a nonlinear function of x. The cross-correlation between y and z, C_{yz} is given in terms of the cross-correlation between x and z, C_{xz} as

$$C_{yz} = \mathbb{E}[U(x)z^*] = \underbrace{\frac{\mathbb{E}[U(x)x^*]}{\mathbb{E}[|x|^2]}}_{\gamma} C_{xz},$$

where γ is known as the Bussgang gain. Thus, the cross-correlation between two signals, when one of which has undergone a transformation, has the same form as the original cross-correlation.

A consequence of the above theorem is that for $z = x$, the output y can be decomposed as

$$y = \gamma x + q$$

where q is a noise term that is uncorrelated to with both y and x. This is known as the *Bussgang decomposition* [27]. It should be pointed out that the Bussgang theorem is distinguished from the Bussgang decomposition, which is used equivalently as a linear decomposition even when the input is not necessarily Gaussian. For the one-bit quantizer

(comparator), the output is $y = Q(x) = \text{sign}(\text{Re}(x)) + j\text{sign}(\text{Im}(x))$, and the Bussgang gain is given by

$$\gamma = \frac{\mathbb{E}[Q(x)x^*]}{\mathbb{E}[|x|^2]} = \frac{\mathbb{E}[|\text{Re}(x)|]}{\mathbb{E}[|\text{Re}(x)|^2]} = \frac{2}{\sqrt{\pi}\sigma_x}.$$

The autocorrelation of y, $R_y(\tau)$ can be expressed in terms of the autocorrelation function of x, $R_x(\tau)$, using Price's theorem [97]

$$R_y(\tau) = \frac{2}{\pi}\sin^{-1}[R_x(\tau)].$$

Bussgang's results have been extended to MIMO systems in recent years. In particular, for an M-element multi-antenna system with input $\mathbf{x} \in \mathbb{C}^{M \times 1} \sim \mathcal{CN}(0, \mathbf{C}_x)$ and ADC output $\mathbf{y} = \mathcal{Q}(\mathbf{x}) \in \mathbb{C}^{M \times 1}$, the Bussgang decomposition can be written in matrix-vector form as [27]

$$\mathbf{y} = \mathbf{\Gamma}\mathbf{x} + \mathbf{q},$$

where $\mathbf{\Gamma}$ is a matrix chosen to make $\mathbf{q}$ uncorrelated with $\mathbf{y}$ and $\mathbf{x}$. This choice is equivalent to selecting a $\mathbf{\Gamma}$ that minimizes the mean-squared error between $\mathbf{x}$ and $\mathbf{y}$, i.e.

$$\mathbf{\Gamma} = \mathbf{C}_{yx}\mathbf{C}_x^{-1},$$

and $\mathbf{\Gamma}\mathbf{x}$ is the linear MMSE estimate of $\mathbf{y}$ given $\mathbf{x}$. For one-bit quantization, $\mathbf{C}_{yx}$ is given by $\mathbf{C}_{yx} = \sqrt{\frac{2}{\pi}}\mathbf{C}_x\mathbf{\Sigma}_x^{-\frac{1}{2}}$ and, therefore we have, $\mathbf{\Gamma} = \sqrt{\frac{2}{\pi}}\mathbf{\Sigma}_x^{-\frac{1}{2}}$, where $\mathbf{\Sigma}_x = \text{diag}(\mathbf{C}_x)$. Invoking Price's theorem as before, the autocorrelation matrix of $\mathbf{y}$, $\mathbf{C}_y$

$$\mathbf{C}_y = \frac{2}{\pi}\left[\sin^{-1}\left(\mathbf{\Sigma}_x^{-\frac{1}{2}}\text{Re}(\mathbf{C}_x)\mathbf{\Sigma}_x^{-\frac{1}{2}}\right) + j\sin^{-1}\left(\mathbf{\Sigma}_x^{-\frac{1}{2}}\text{Im}(\mathbf{C}_x)\mathbf{\Sigma}_x^{-\frac{1}{2}}\right)\right].$$

Note that even though $\mathbf{\Gamma}$ was a diagonal matrix in the above example, this is not necessarily

the case in case of non-Gaussian signals.

In this dissertation, the above decomposition is referred to as the *vector-wise Bussgang decomposition* to distinguish it from the *element-wise Bussgang decomposition* outlined below. The motivation for considering an element-wise decomposition is that the condition that $\mathbf{q}$ and $\mathbf{x}$ are uncorrelated may be too stringent and may not always be valid in practice as we will see in Chapter 4. In the element-wise version, $\boldsymbol{\Gamma}$ is considered to be a diagonal matrix given by $\boldsymbol{\Gamma} = \mathrm{diag}(\gamma_1, \gamma_2, \ldots, \gamma_M)$. At the mth antenna element, we have

$$y_m = \gamma_m x_m + q_m$$

$$\gamma_m = \frac{\mathbb{E}[\mathcal{Q}_m(x_m)x_m^*]}{\mathbb{E}[|x_m|^2]} = \frac{\mathbb{E}[|\mathrm{Re}(x)|]}{\mathbb{E}[|\mathrm{Re}(x)|^2]}.$$

The element-wise decomposition will be elaborated on in Chapter 4.

2.3 Cramér-Rao bound (CRB)

In parameter estimation, it is often useful to quantify a benchmark against which we can compare the performance of an unbiased estimator. Performance bounds are useful in designing systems and in analyzing the effect of different parameters that affect the system performance. The concept of efficient estimators is also related to the existence of such a lower bound. The celebrated Cramér-Rao bound (CRB) is a lower bound on the MSE of unbiased estimators and it is closely related to the theory of maximum likelihood (ML). ML estimators are known to be asymptotically efficient and achieve the CRB. Estimation theory in general consists of two frameworks- deterministic and Bayesian approaches. In the deterministic approach, the parameters to be estimated are modeled as deterministic but unknown, whereas in the Bayesian approach, the parameters are modeled as random variables with known a priori pdfs and the goal is to estimate their realizations. Similarly, the

performance bounds can also be classified as deterministic or Bayesian. The most general deterministic bound is the Barankin bound [122], which is not straightforward to obtain in closed-form. The CRB is the most widely used deterministic local bound since it is relatively easy to compute for many practical problems. The Bhattacharya bound [123] is another local bound which is a generalized version of the CRB. The Bayesian class of bounds consists of the Ziv-Zakaï family [124], which relates the MSE to the probability of error in a binary hypothesis testing problem, and the Weiss-Weinstein family [125], to which the Bayesian CRB belongs.

Let $\ln p(\mathbf{x}; \boldsymbol{\theta})$ be the log-likelihood function parameterized by the deterministic vector $\boldsymbol{\theta}$ that is of interest to be estimated. The CRB theorem is stated in Theorem 2.

Theorem 2 (CRB theorem [126]): Assuming that $p(\mathbf{x}; \boldsymbol{\theta})$ satisfies the regularity condition

$$\mathbb{E}\left[\nabla_{\boldsymbol{\theta}} \ln p(\mathbf{x}; \boldsymbol{\theta})\right] = \mathbf{0}, \quad \text{for all } \boldsymbol{\theta},$$

the variance of an unbiased estimator of $\boldsymbol{\theta}$, $\hat{\boldsymbol{\theta}}$, satisfies

$$\mathrm{var}(\hat{\theta}_i) \geq \left[\mathbf{J}_D^{-1}\right]_{ii}$$

where $\mathbf{J}_D$ is the Fisher information matrix (FIM) given by

$$[\mathbf{J}_D]_{ij} = -\mathbb{E}\left[\frac{\partial^2 \ln p(\mathbf{x}; \boldsymbol{\theta})}{\partial \theta_i \, \partial \theta_j}\right].$$

An unbiased estimator that attains the bound exists if and only if the gradient $\nabla_{\boldsymbol{\theta}} \ln p(\mathbf{x}; \boldsymbol{\theta})$ can be written as

$$\nabla_{\boldsymbol{\theta}} \ln p(\mathbf{x}; \boldsymbol{\theta}) = \mathbf{J}_D \left(\mathbf{g}(\boldsymbol{\theta}) - \boldsymbol{\theta}\right),$$

and $\mathbf{g}(\boldsymbol{\theta})$ is the estimator that attains the bound.

The Bayesian version of the CRB can be derived when $\boldsymbol{\theta}$ is a random variable with the a priori pdf $p(\boldsymbol{\theta})$. The overall FIM in this case is the sum of two information matrices

$$\mathbf{J} = \mathbf{J}_D + \mathbf{J}_P, \qquad [\mathbf{J}_D]_{ij} = -\mathbb{E}\left[\frac{\partial^2 \ln p(\mathbf{x}|\boldsymbol{\theta})}{\partial \theta_i\, \partial \theta_j}\right] \qquad [\mathbf{J}_P]_{ij} = -\mathbb{E}\left[\frac{\partial^2 \ln p(\boldsymbol{\theta})}{\partial \theta_i\, \partial \theta_j}\right].$$

In the case of Gaussian observations for which $\mathbf{x} \sim \mathcal{N}\left(\boldsymbol{\mu}(\boldsymbol{\theta}), \mathbf{C}(\boldsymbol{\theta})\right)$, the CRB is given by the compact expression [126]

$$[\mathbf{J}_D]_{ij} = \left[\frac{\partial \boldsymbol{\mu}(\boldsymbol{\theta})}{\partial \theta_i}\right]^T \mathbf{C}^{-1}(\boldsymbol{\theta}) \left[\frac{\partial \boldsymbol{\mu}(\boldsymbol{\theta})}{\partial \theta_j}\right] + \frac{1}{2}\mathrm{Tr}\left(\mathbf{C}^{-1}(\boldsymbol{\theta})\frac{\partial \mathbf{C}(\boldsymbol{\theta})}{\partial \theta_i}\mathbf{C}^{-1}(\boldsymbol{\theta})\frac{\partial \mathbf{C}(\boldsymbol{\theta})}{\partial \theta_j}\right).$$

In Chapter 3, the CRB is used to evaluate the performance of several channel parameter models in massive MIMO systems when the base station (BS) is equipped with one-bit resolution ADCs.

2.4   Channel models

The MIMO channel models considered in this dissertation are discrete-multipath channel models. The signal at the receiver is the sum of a finite number of copies of the transmitted signal as in Fig. 2.5 where each path responsible for reflection, scattering or diffraction of the transmitted signal is characterized by its own path loss, delay and a possible Doppler. The illustrated channel response shows three such multipaths with delays τ_1, τ_2 and τ_3. The channel impulse response, represented by $h(t, \tau)$ is the low-pass response of the channel at time t to an impulse at time $t - \tau$ and a general model for such a channel is given by [127, 128]
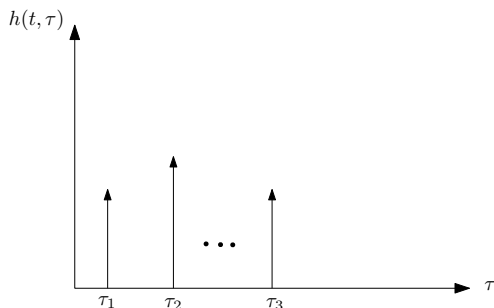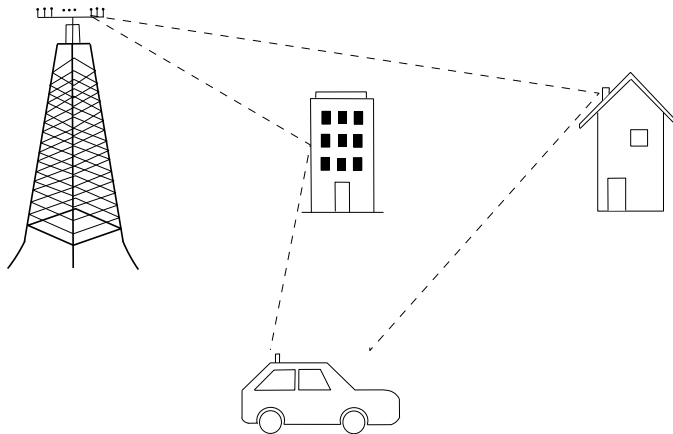
Figure 2.5: Multipath fading and the channel impulse response.

$$h(t,\tau) = \sum_{l=1}^{L} \alpha_l e^{j\omega_c(t-\tau_l)}\delta(\tau - \tau_l), \tag{2.3}$$

where τ_l and α_l are the delay and path loss/shadowing coefficient associated with the lth multipath, and ω_c is the carrier frequency.

For a narrowband channel for which the *delay spread* is small relative to the inverse signal bandwidth, if L is large enough, the central limit theorem can be invoked to approximate α_l and τ_l as stationary and the real and imaginary parts of the channel are jointly Gaussian

processes. A general model for a narrowband MIMO channel is given by

$$\mathbf{h} = \sum_{l=1}^{L} \alpha_l \mathbf{a}_l, \tag{2.4}$$

where $\mathbf{a}$ is a vector of length equal to the number of receive antennas, M, and contains the array response for the signal arriving in path l.

In a structured channel model, the array responses $\mathbf{a}_l$ are known functions of the direction-of-arrival (DOA) associated with the multipaths. In the nominal case, the arrays are precisely calibrated assuming that the array configurations are known. The model may be modified to factor in situations where there is some uncertainty in the array responses. Imperfect calibration, presence of mutual coupling between antenna elements, can be factored into the overall response by adding a small perturbation term to the nominal response: $\mathbf{a}_l + \Delta \mathbf{a}_l$.

In an unstructured channel model, the specific functions that generate $\mathbf{a}_l$ are not defined. The purpose of considering such a model is to approximate a structured channel model when there are severe calibration errors and to simplify the channel estimation process.

The specifics of the structured and unstructured channel models and the associated perturbation models are discussed in more detail in Chapter 3. Slightly different variations of the channel model are used throughout the dissertation depending on the application and the scenario under consideration.

Chapter 3

Channel Estimation Performance Bounds in One-Bit Millimeter-Wave Massive MIMO Systems

In this chapter, CRB performance bounds for mmWave massive MIMO, where the BS is equipped with one-bit ADCs, are considered.

Traditional channel models that assume Rayleigh fading are not suitable for mmWave systems because the scattering environment of mmWave channels is not dense, but rather sparse with line-of-sight (LOS) and a few reflected propagation paths contributing to the effective channel. The analysis focuses on a one-bit mmWave single-input-multiple-output (SIMO) pilot-based single-carrier transmission system where a single transmitter is equipped with one antenna and the base station employs an antenna array. To simplify the analysis, Doppler spread is not assumed to be present, so the angle and delay parameters are assumed to be time-invariant over the channel estimation period. A structured channel model for a single user where the channel is composed of a superposition of multipaths characterized by path

delays and DOAs, an unstructured channel model where the channel is a generic FIR filter, and a dictionary-based channel model, where the path delays and DOAs are selected from small perturbations on a discrete grid and a sparsity constraint applies to the vector of path loss components, are considered. The Bayesian CRB when the array response is imperfectly known and is affected by perturbations in the sensor pattern or position is also derived. The CRBs are evaluated numerically and the effects of various system parameters on the CRB are studied.

3.1   MmWave Channel Model
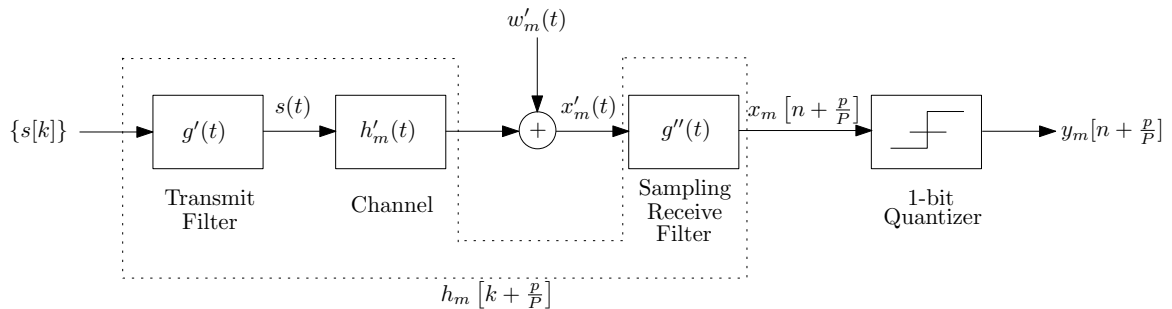
Figure 3.1: System block diagram. © IEEE.

An uplink mmWave MIMO system with a single-antenna user terminal and M receive antennas at the base station is considered. It is assumed that the wireless communication channel is linear and its properties change slowly with respect to the signal duration. The communication system block diagram is illustrated in Fig. 3.1. The received baseband signal at the mth antenna is given by

$$x'_m(t) = \sqrt{P_t} \int_{-\infty}^{\infty} h'_m(t')s(t-t')dt' + w'_m(t), \tag{3.1}$$

where P_t is the transmit signal power, $h'_m(t)$ is the impulse response of the channel from the transmitter to antenna m at time t and $w'_m(t)$ is the corresponding noise.

30

The source signal is assumed to be band-limited to $[-B/2, B/2]$, and $w'_m(t)$ is a complex circularly symmetric and temporally white Gaussian process with power spectral density N_0. The source signal $s(t)$ is encoded as a digital signal with a common pulse period T_s, where the complex valued symbols $\{s[k]\}$ are modulated by a pulse shape function $g'(t)$ as

$$s(t) = \sum_{k=-\infty}^{\infty} s[k]g'(t - kT_s).$$

The received signal in (3.1) is assumed to be fractionally sampled by the filter $g''(t)$ by a factor of P, and can be equivalently represented in sampled time as

$$x_m\left[n + \frac{p}{P}\right] = \sqrt{P_t} \sum_{l=-\infty}^{\infty} h_m\left[l + \frac{p}{P}\right] s[n - l] + w_m\left[n + \frac{p}{P}\right], \qquad (3.2)$$

where $p = 0, 1, \ldots, P-1$, $h_m\left[l + \frac{p}{P}\right]$ is the equivalent discrete-time channel and $w_m\left[n + \frac{p}{P}\right]$ is the discrete-time noise, given by

$$h_m\left[l + \frac{p}{P}\right] = \int_{-\infty}^{\infty} \int_{-\infty}^{\infty} g''\left(\left(l + \frac{p}{P}\right)T_s - t''\right) h'_m(t'' - t')g'(t')dt'dt''$$
$$w_m\left[n + \frac{p}{P}\right] = \int_{-\infty}^{\infty} g''(t'')w'_m\left(\left(n + \frac{p}{P}\right)T_s - t''\right) dt''.$$

The effects of the transmit and receive filters, $g'(t)$ and $g''(t)$, are absorbed into $g(t) = g''(t) \circledast g'(t)$. The convolutive channel is assumed to be frequency selective with maximum delay length of L symbol periods, so that the FIR assumption means that at most L consecutive symbols play a role in the received signal, i.e. $h_m\left[l + \frac{p}{P}\right]$ is zero outside the interval $[0, L-1]$. Generally, oversampling w.r.t. the Nyquist rate results in noise correlation [129]. However, if the receive filter $g''(t)$ is chosen to be a root-Nyquist pulse, the discrete-time noise $w_m[n]$ is white [130]. Consequently, the root-raised-cosine filter is chosen for the transmit and receive filters in our analysis, so that

$$g(t) = \frac{\sin \pi t/T_s}{\pi t/T_s} \frac{\cos \pi \alpha t/T_s}{1 - 4\alpha^2 t^2/T_s^2},$$

where α is the roll-off factor and the noise $w_m[n] \sim \mathcal{CN}(0, \sigma^2)$, $\sigma^2 = N_0 B$. In the analysis, it is assumed that the noise variance σ^2 is known, since the channel gains and σ^2 are not separately identifiable when one-bit quantization is used, which leads to a singular FIM [77, 78].

3.1.1 Unstructured Channel Model

In the unstructured case, the channel is modeled as a uniformly sampled FIR filter characterized by the complex gains of each path to the receiver. Let $\beta_{r,m}$ be the complex path gain of the rth path to the mth antenna so that the channel between the source and antenna m is

$$h_m'(t) = \sum_{r=1}^{R} \beta_{r,m} \delta(t - (\tau_0 + (r-1)\Delta')),$$

where τ_0 corresponds to the delay of the first multipath arrival, and the value of Δ' is determined by the minimum resolvable time difference between different paths. Under this FIR model, the discrete channel can be expressed as $\mathbf{h}[k] = [h_1[k], h_2[k], \ldots, h_M[k]]^T$, where $k = l + \frac{p}{P}$, and

$$\mathbf{h}[k] = \underbrace{\begin{bmatrix} \beta_{1,1} & \cdots & \beta_{R,1} \\ \beta_{1,2} & \cdots & \beta_{R,2} \\ \vdots & \cdots & \vdots \\ \beta_{1,M} & \cdots & \beta_{R,M} \end{bmatrix}}_{\tilde{\boldsymbol{\beta}} \in \mathbb{C}^{M \times R}} \begin{bmatrix} g(kT_s - \tau_0) \\ g(kT_s - (\tau_0 + \Delta')) \\ \vdots \\ g(kT_s - (\tau_0 + (R-1)\Delta')) \end{bmatrix}. \tag{3.3}$$

The parameters of the unstructured model are comprised by $\boldsymbol{\beta}$, the vector of all complex path gains, i.e. $\boldsymbol{\beta} = \mathrm{vec}(\tilde{\boldsymbol{\beta}})$, and $\boldsymbol{\beta}^{\mathrm{Re}} = \mathrm{Re}\,(\boldsymbol{\beta}) \in \mathbb{R}^{MR \times 1}$ and $\boldsymbol{\beta}^{\mathrm{Im}} = \mathrm{Im}\,(\boldsymbol{\beta}) \in \mathbb{R}^{MR \times 1}$.

3.1.2 Structured Channel Model

The structured channel model is a geometric channel parameterized by path loss components, path delays and DOAs. The response of the antenna array to a waveform arriving from direction θ is denoted by $\mathbf{a}(\theta, \boldsymbol{\rho}) \in \mathbb{C}^{M \times 1}$. The vector $\boldsymbol{\rho}$ represents parameters on which the array response depends (e.g., antenna positions, gain and phase response, etc.). These parameters are assumed to be a priori known to be Gaussian with some nominal mean value $\boldsymbol{\rho}_0$ and covariance $\boldsymbol{\Omega}$. Let the DOA of the rth multipath, measured clockwise with respect to the y-axis, be $\theta_r, r = 1, 2, \ldots, R$, and assume that the antenna elements are close enough together so that they share a common complex path gain γ_r for the rth path. The path gain γ_r is an aggregate of the large-scale fading, namely the path loss and shadowing, as well as the small scale fading. More specifically,

$$\beta_{r,m} = \gamma_r q_m(\theta_r, \boldsymbol{\rho})\exp(-j\omega_c\tau_{r,m}), \tag{3.4}$$

where ω_c is the carrier frequency and $q_m(\theta_r, \boldsymbol{\rho})$ is the sensor pattern of the mth sensor in the direction θ_r. The channel between the source and the mth antenna is

$$h'_m(t) = \sum_{r=1}^{R} \gamma_r q_m(\theta_r, \boldsymbol{\rho})\exp(-j\omega_c\tau_{r,m})\delta(t - \tau_{r,m}).$$

Incorporating the transmit and receive pulse shaping, the discrete-time equivalent channel becomes $h_m[k] = \sum_{r=1}^{R} \gamma_r q_m(\theta_r, \boldsymbol{\rho})g(kT_s - \tau_{r,m})\exp(-j\omega_c\tau_{r,m})$ and stacking the discrete-time channels from all M antennas, we get

$$\mathbf{h}[k] = \sum_{r=1}^{R} \gamma_r \begin{bmatrix} g(kT_s - \tau_{r,1}) \\ g(kT_s - \tau_{r,2}) \\ \vdots \\ g(kT_s - \tau_{r,M}) \end{bmatrix} \odot \mathbf{a}(\theta_r, \boldsymbol{\rho}), \tag{3.5}$$

where $\odot$ is the Hadamard (element-wise) product and the term $\exp(-j\omega_c\tau_{r,m})$ in (3.4) was absorbed into the expression for the array response $\mathbf{a}(\theta_r, \boldsymbol{\rho})$ by writing it in terms of the array sensor coordinates. Note that (3.5) uses time delays rather than phase shifts in the pulse shaping functions because the inverse bandwidth of the signals at mmWave frequencies may approach the inter-element delay between antennas in the array.

As an example of the array perturbation parameter $\boldsymbol{\rho}$, consider the case of sensor position and pattern perturbation. The array response vector $\mathbf{a}(\theta_r, \boldsymbol{\rho})$ can be written as

$$\mathbf{a}(\theta_r, \boldsymbol{\rho}) = \begin{bmatrix} q_1(\theta_r, \boldsymbol{\rho})\exp\left(-j2\pi(b_1(\boldsymbol{\rho})\sin\theta_r + c_1(\boldsymbol{\rho})\cos\theta_r)/\lambda\right) \\ \vdots \\ q_M(\theta_r, \boldsymbol{\rho})\exp\left(-j2\pi(b_M(\boldsymbol{\rho})\sin\theta_r + c_M(\boldsymbol{\rho})\cos\theta_r)/\lambda\right) \end{bmatrix},$$

where $(b_m(\boldsymbol{\rho}), c_m(\boldsymbol{\rho}))$ are the coordinates of the mth sensor. In the presence of an antenna pattern perturbation only [112], we have $q_m(\theta_r, \boldsymbol{\rho}) = q_{m,0}(\theta_r) + \rho_m$, where $q_{m,0}(\theta_r)$ is the nominal pattern, ρ_m is the complex perturbation and $\boldsymbol{\rho}$ stacks both the real and imaginary parts of the complex perturbation for all antennas, so that $\boldsymbol{\rho} \in \mathbb{R}^{2M \times 1}$. For sensor position perturbations only, the sensor coordinates can be modeled in a recursive manner as in [110]. The following piecewise linear model applies to flexible array structures: $(b_m(\boldsymbol{\rho}), c_m(\boldsymbol{\rho})) = (b_{m-1} + \delta\sin\phi_m(\boldsymbol{\rho}),\ c_{m-1} + \delta\cos\phi_m(\boldsymbol{\rho}))$, where $\phi_m(\boldsymbol{\rho}) = \phi_{m-1} + \rho_{m-1}$, with initial conditions $\phi_1 = \pi/2$, $b_1 = c_1 = 0$, and δ is the spacing between antenna elements. Thus, ρ_m is the incremental angular perturbation of the mth sensor and $\boldsymbol{\rho} \in \mathbb{R}^{M-1 \times 1}$.

A special case of the above modeling is a uniform linear array operating with a nominal omnidirectional sensor pattern, $q_m(\theta_r) = 1$ and $\boldsymbol{\rho} = \mathbf{0}$. The path delay to the mth sensor is given by $\tau_{r,m} = \tau_r + (m-1)\frac{\delta}{c}\sin\theta_r$, where c is the speed of light and $\tau_r = \tau_{r,1}$ is the time delay of the rth propagation path to the first antenna element. Let $\mathbf{g}_k(\tau_r, \theta_r) = \left[g(kT_s - \tau_r), \ldots, g\left(kT_s - \tau_r - \frac{(M-1)\delta\sin\theta_r}{c}\right)\right]^T$, $\mathbf{a}(\theta_r) = \left[1, e^{-j\frac{2\pi\delta}{\lambda}\sin\theta_r}, \ldots, e^{-j\frac{2\pi\delta}{\lambda}(M-1)\sin\theta_r}\right]^T$ where λ is the wavelength, and $\boldsymbol{\gamma} = [\gamma_1, \gamma_2, \ldots, \gamma_R]^T$. The lth delay-tap of the channel

can then be written as

$$\mathbf{h}[k] = \underbrace{[\mathbf{g}_k(\tau_1, \theta_1), \mathbf{g}_k(\tau_2, \theta_2), \ldots, \mathbf{g}_k(\tau_R, \theta_R)]}_{\mathbf{G}_k \in \mathbb{R}^{M \times R}} \odot \underbrace{[\mathbf{a}(\theta_1)\,\mathbf{a}(\theta_2)\,\ldots\,\mathbf{a}(\theta_R)]}_{\mathbf{A} \in \mathbb{C}^{M \times R}} \boldsymbol{\gamma}. \tag{3.6}$$

In the derivation of the CRB, the following notation is used: $\boldsymbol{\gamma}^{\mathrm{Re}} = \mathrm{Re}\,(\boldsymbol{\gamma})$ and $\boldsymbol{\gamma}^{\mathrm{Im}} = \mathrm{Im}\,(\boldsymbol{\gamma})$.

Note: Although the path delays, $\tau_{r,m}$, are functions of $\boldsymbol{\rho}$ (in the case of position perturbation, for example), this effect is not considered in the derivation of the FIM since the derivative of $\boldsymbol{\tau}$ with respect to $\boldsymbol{\rho}$ is negligible.

3.1.3 Dictionary Based Channel Model

In mmWave transmission, the propagation channel is often described using a sparse scattering model. The underlying channel is still parameterized by DOAs, path delays and complex path gains as in the structured model, but the DOAs and delays are assumed to lie on a fixed grid, and the channel estimation is formulated as a sparse recovery problem. This approach leverages tools available in compressive sensing to design efficient algorithms for determining the channel. A grid mismatch occurs if a particular DOA is not present in the possible DOA set. In our analysis, the true DOA is modeled as a perturbation to the nearest DOA in the grid. Let the uniform grid of DOAs consist of N_a points with $N_a \geq M$, so that the DOA dictionary is the set $\theta' \in \{0, 2\pi/N_a, \ldots, 2\pi(N_a - 1)/N_a\}$. Then, a Taylor interpolation of $\mathbf{a}(\theta, \boldsymbol{\rho})$ around the nearest DOA in the grid, θ', yields

$$\mathbf{a}(\theta' + \theta, \boldsymbol{\rho}) = \mathbf{a}(\theta', \boldsymbol{\rho}) + \theta \frac{\partial \mathbf{a}(\theta, \boldsymbol{\rho})}{\partial \theta}\bigg|_{\theta = \theta'}. \tag{3.7}$$

Here, θ is used to denote the grid mismatch between the nearest DOA grid point and the DOA of the corresponding multipath, rather than the multipath DOA as in the structured channel.

Similarly, the uniform delay grid is the set $\tau' \in \left\{0, \frac{(L-1)T_s}{N_d}, \ldots, \frac{(L-1)(N_d-1)T_s}{N_d}\right\}$ and a Taylor interpolation similar to (3.7) can be performed to obtain

$$g(kT_s - \tau' - \tau) = g(kT_s - \tau') + \tau \frac{\partial g(kT_s - \tau)}{\partial \tau}\bigg|_{\tau=\tau'}. \tag{3.8}$$

Here, τ is used to denote the grid mismatch between the nearest delay grid point and the delay of the corresponding multipath. Having taken into account the dictionary errors, the discrete-time channel $\mathbf{h}[k]$ for the dictionary-based channel model is given by

$$\mathbf{h}[k] = (\mathbf{G}_D(kT_s, \boldsymbol{\tau}) \otimes \mathbf{A}_D(\boldsymbol{\theta}, \boldsymbol{\rho}))\, \boldsymbol{\gamma}, \tag{3.9}$$

where $\mathbf{A}_D(\boldsymbol{\theta}, \boldsymbol{\rho}) \in \mathbb{C}^{M \times N_a}$ and $\mathbf{G}_D(kT_s, \boldsymbol{\tau}) \in \mathbb{R}^{P \times N_d}$ are the angular and delay domain perturbed dictionary matrices, respectively, and $\boldsymbol{\theta}$ and $\boldsymbol{\tau}$ are the vectors of grid mismatch errors to be estimated. The columns of $\mathbf{G}_D(kT_s, \boldsymbol{\tau})$ are of the form $[g(kT_s - \tau' - \tau), \ldots, g((k + \frac{P-1}{P})T_s - \tau' - \tau)]^T$, and the columns of $\mathbf{A}_D(\boldsymbol{\theta}, \boldsymbol{\rho})$ are of the form $\mathbf{a}(\theta' + \theta, \boldsymbol{\rho})$. The complex unknown vector $\boldsymbol{\gamma}$ is a sparse $N_a N_d \times 1$ vector that carries the path gains from the corresponding DOAs and delays in the dictionary. The sparse formulation implies that $\boldsymbol{\gamma}$ only has $R \ll N_a N_d$ non-zero elements. In the analysis of the CRB for this model, and unlike the structured and unstructured models described above, it is assumed that the locations of the non-zero elements in $\boldsymbol{\gamma}$, and therefore the nearest angle and delay grid points are known a priori. The benefit of this a priori information will depend on the resolution of the grid, and the ability of dictionary-based methods to correctly identify the correct grid points. The assumption should be a reasonable one for dictionaries whose grids are not too finely spaced.

3.1.4 System Model

Gathering the received signals at the M antennas from (3.2) in $\mathbf{x}$ and the noise in $\mathbf{w}$,

$$\mathbf{x}\left[n + \frac{p}{P}\right] = \sqrt{P_t} \sum_{l=0}^{L-1} \mathbf{h}\left[l + \frac{p}{P}\right] s[n-l] + \mathbf{w}\left[n + \frac{p}{P}\right],$$

where $\mathbf{h}\left[l + \frac{p}{P}\right]$ corresponds to (3.6) for the structured channel, (3.3) for the unstructured channel and (3.9) for the dictionary based channel model. The samples from N source symbol periods, where the coherence time of the channel is greater than NT_s are collected, and the received signal at each antenna are sampled at P times the symbol rate. The $MP \times N$ spatial and temporal samples of the received signal are collected in the matrix $\mathbf{X}$ to get

$$\mathbf{X} = \begin{bmatrix} \mathbf{x}[0] & \mathbf{x}[1] & \ldots & \mathbf{x}[N-1] \\ \mathbf{x}[\frac{1}{P}] & \mathbf{x}[1+\frac{1}{P}] & \ldots & \mathbf{x}[N-1+\frac{1}{P}] \\ \vdots & \vdots & \vdots & \vdots \\ \mathbf{x}[\frac{P-1}{P}] & \mathbf{x}[1+\frac{P-1}{P}] & \ldots & \mathbf{x}[N-1+\frac{P-1}{P}] \end{bmatrix}$$

$$= \sqrt{P_t} \underbrace{\begin{bmatrix} \mathbf{h}[0] & \mathbf{h}[1] & \ldots & \mathbf{h}[L-1] \\ \mathbf{h}[\frac{1}{P}] & \mathbf{h}[1+\frac{1}{P}] & \ldots & \mathbf{h}[L-1+\frac{1}{P}] \\ \vdots & \vdots & \vdots & \vdots \\ \mathbf{h}[\frac{P-1}{P}] & \mathbf{h}[1+\frac{P-1}{P}] & \ldots & \mathbf{h}[L-1+\frac{P-1}{P}] \end{bmatrix}}_{\mathbf{H} \in \mathbb{C}^{MP \times L}} \underbrace{\begin{bmatrix} s[0] & s[1] & \ldots & s[N-1] \\ s[-1] & s[0] & \ldots & s[N-2] \\ \vdots & \vdots & \vdots & \vdots \\ s[-L+1] & s[-L+2] & \ldots & s[N-L] \end{bmatrix}}_{\tilde{\mathbf{S}} \in \mathbb{C}^{L \times N}} + \mathbf{W}.$$

$$(3.10)$$

Vectorizing (3.10) and taking the real and imaginary parts separately, we have

$$\mathbf{x} = \begin{bmatrix} \mathrm{Re}\left(\mathrm{vec}(\mathbf{X})\right) \\ \mathrm{Im}\left(\mathrm{vec}(\mathbf{X})\right) \end{bmatrix} = \mathbf{Sh} + \mathbf{w}, \qquad (3.11)$$

where,

$$
\mathbf{S} = \begin{bmatrix} \mathrm{Re}\left(\tilde{\mathbf{S}}^T \otimes \sqrt{P_t}\mathbf{I}_{MP}\right) & -\mathrm{Im}\left(\tilde{\mathbf{S}}^T \otimes \sqrt{P_t}\mathbf{I}_{MP}\right) \\ \mathrm{Im}\left(\tilde{\mathbf{S}}^T \otimes \sqrt{P_t}\mathbf{I}_{MP}\right) & \mathrm{Re}\left(\tilde{\mathbf{S}}^T \otimes \sqrt{P_t}\mathbf{I}_{MP}\right) \end{bmatrix} \in \mathbb{R}^{2MNP \times 2LMP},
$$

$$
\mathbf{h} = \begin{bmatrix} \mathrm{Re}\left(\mathrm{vec}(\mathbf{H})\right) \\ \mathrm{Im}\left(\mathrm{vec}(\mathbf{H})\right) \end{bmatrix} \in \mathbb{R}^{2LMP \times 1},
$$

$$
\mathbf{w} = \begin{bmatrix} \mathrm{Re}\left(\mathrm{vec}(\mathbf{W})\right) \\ \mathrm{Im}\left(\mathrm{vec}(\mathbf{W})\right) \end{bmatrix} \in \mathbb{R}^{2MNP \times 1},
$$

Note that $\mathbf{w} \sim \mathcal{N}(\mathbf{0}, \frac{\sigma^2}{2}\mathbf{I})$. The per-antenna SNR at the receiver is defined as

$$
\mathrm{SNR} = \frac{P_t}{\sigma^2} \sum_{l=0}^{L-1} \sum_{p=0}^{P-1} \mathbb{E}\left[|h_m[l + p/P]|^2\right].
$$

As in [27], the quantization operation is defined as $\mathcal{Q}(\cdot) = \frac{1}{\sqrt{2}}(\mathrm{sign}(\cdot))$, where the sign operation is performed separately for the real and imaginary parts, so the quantized output $\mathbf{x}$ is

$$
\mathbf{y} = \mathcal{Q}(\mathbf{x}) = \mathcal{Q}(\mathbf{Sh} + \mathbf{w}).
$$

A distinction between the unstructured, structured and dictionary based models is that in the structured model and the dictionary based model, the channel parameters are estimated, whereas in the unstructured model, the channel $\mathbf{h}$ is estimated.

3.2   Cramér-Rao Bound

In this section, the CRB is derived for parameters of the spatially structured and unstructured channel models. For the spatially structured channel model, the parameter vector

consists of both deterministic and stochastic components. The deterministic components are, namely, the DOAs, path delays and complex path gains. When considering sensor position perturbations only, we have $\boldsymbol{\rho} \in \mathbb{R}^{M-1 \times 1}$, and for pattern perturbations only, we have $\boldsymbol{\rho} = \left[\ \mathrm{Re}(\rho_1), \mathrm{Re}(\rho_2), \ldots, \mathrm{Re}(\rho_M), \mathrm{Im}(\rho_1), \mathrm{Im}(\rho_2), \ldots, \mathrm{Im}(\rho_M) \ \right] \in \mathbb{R}^{2M \times 1}$. The full list of parameters is $\boldsymbol{\Theta} = \left[\boldsymbol{\theta}, \boldsymbol{\tau}, \boldsymbol{\gamma}^{\mathrm{Re}}, \boldsymbol{\gamma}^{\mathrm{Im}}, \boldsymbol{\rho} \right]$ under the structured and dictionary-based channel models, and $\boldsymbol{\Theta} = \left[\boldsymbol{\beta}^{\mathrm{Re}}, \boldsymbol{\beta}^{\mathrm{Im}} \right]$ for the unstructured model. Assuming independent observations, the log-likelihood for the spatially structured and unstructured models, $l(\mathbf{y}; \boldsymbol{\Theta})$, can be obtained as

$$l(\mathbf{y}; \boldsymbol{\Theta}) = \sum_{k=1}^{2MNP} \ln \Psi \left(\frac{2}{\sigma} y_k u_k \right),$$

where y_k is the kth element of $\mathbf{y}$, $u_k = \left(\mathbf{s}^{(k,)} \right)^T \mathbf{h}$, $\mathbf{s}^{(k,)}$ is the kth row of $\mathbf{S}$, and $\Psi(x)$ is the cumulative distribution function of the standard normal distribution. Assuming that the regularity condition of the log-likelihood holds, the FIM has the following form [131]:

$$\mathbf{J} = \mathbf{J}_D + \mathbf{J}_P,$$

where $\mathbf{J}_D$ and $\mathbf{J}_P$ are the information matrices obtained from the data and the a priori information, respectively. The (i, j)th elements of $\mathbf{J}_D$ and $\mathbf{J}_P$ are given by

$$[\mathbf{J}_D]_{i,j} = - \mathbb{E}_{\mathbf{y}, \boldsymbol{\rho}} \left[\frac{\partial^2}{\partial \Theta_i \partial \Theta_j} l(\mathbf{y}; \boldsymbol{\Theta}) \right]$$
$$[\mathbf{J}_P]_{i,j} = \mathbb{E}_{\boldsymbol{\rho}} \left[\frac{\partial^2}{\partial \Theta_i \partial \Theta_j} (\boldsymbol{\rho} - \boldsymbol{\rho}_0)^T \boldsymbol{\Omega}^{-1} (\boldsymbol{\rho} - \boldsymbol{\rho}_0) \right],$$

where $\boldsymbol{\Omega}$ is the covariance matrix of $\boldsymbol{\rho}$. Since only $\boldsymbol{\rho}$ is random, the matrix $\mathbf{J}_P$ is given by

$$\mathbf{J}_P = \mathrm{blkdiag}\{\mathrm{diag}(\mathbf{0}_D), \boldsymbol{\Omega}^{-1}\},$$

where blkdiag$\{\cdot\}$ is a block-diagonal matrix where the arguments form the diagonal blocks, and $D = 4R$, $D = 2MR$ and $D = 4R$, for the structured, unstructured and dictionary based channel models respectively.

The expectation with respect to the joint distribution of $\mathbf{y}$ and $\boldsymbol{\rho}$ in $\mathbf{J}_D$ is difficult to compute. Instead, the approach in [110, 112] is followed. If the perturbations are small, $\mathbf{J}_D$ can be approximated to order $O(1)$ around ρ_0, in which case

$$[\mathbf{J}_D]_{i,j} \approx -\mathbb{E}_{\mathbf{y}} \left[\frac{\partial^2}{\partial \Theta_i \partial \Theta_j} l(\mathbf{y}; \boldsymbol{\Theta}) \right] \Bigg|_{\boldsymbol{\rho} = \boldsymbol{\rho}_0} . \tag{3.12}$$

Then, the CRB for the ith parameter of an unbiased estimator with $\mathbb{E}\left[\hat{\boldsymbol{\Theta}}\right] = \boldsymbol{\Theta}$ is given by the (i, i) element of the inverse of the FIM, where the FIM is computed at the "true" values of $\boldsymbol{\Theta}$ and $\boldsymbol{\rho}$. That is,

$$\mathrm{var}(\hat{\Theta}_i) \geq \left[\mathbf{J}^{-1}(\boldsymbol{\Theta}) \right]_{i,i} .$$

The approximation in (3.12) is sufficiently accurate for values of $\boldsymbol{\rho}$ commonly encountered in real calibrated systems (see [112] for more details).

3.2.1 Unstructured Channel

For the unstructured channel model, the FIM is given by

$$\mathbf{J} = \begin{bmatrix} \mathbf{J}_{\boldsymbol{\beta}^{\mathrm{Re}}} & \mathbf{J}_{\boldsymbol{\beta}^{\mathrm{Re}}\boldsymbol{\beta}^{\mathrm{Im}}} \\ \mathbf{J}_{\boldsymbol{\beta}^{\mathrm{Re}}\boldsymbol{\beta}^{\mathrm{Im}}}^T & \mathbf{J}_{\boldsymbol{\beta}^{\mathrm{Im}}} \end{bmatrix} \in \mathbb{R}^{2MR \times 2MR}, \tag{3.13}$$

with

$$\mathbf{J}_{\boldsymbol{\beta}^{\mathrm{Re}}} = \mathbb{E}\left[\nabla_{\boldsymbol{\beta}^{\mathrm{Re}}}l(\mathbf{y};\boldsymbol{\Theta})(\nabla_{\boldsymbol{\beta}^{\mathrm{Re}}}l(\mathbf{y};\boldsymbol{\Theta}))^T\right] \in \mathbb{R}^{MR \times MR},$$

$$\mathbf{J}_{\boldsymbol{\beta}^{\mathrm{Im}}} = \mathbb{E}\left[\nabla_{\boldsymbol{\beta}^{\mathrm{Im}}}l(\mathbf{y};\boldsymbol{\Theta})(\nabla_{\boldsymbol{\beta}^{\mathrm{Im}}}l(\mathbf{y};\boldsymbol{\Theta}))^T\right] \in \mathbb{R}^{MR \times MR}, \qquad (3.14)$$

$$\mathbf{J}_{\boldsymbol{\beta}^{\mathrm{Re}}\boldsymbol{\beta}^{\mathrm{Im}}} = \mathbb{E}\left[\nabla_{\boldsymbol{\beta}^{\mathrm{Re}}}l(\mathbf{y};\boldsymbol{\Theta})(\nabla_{\boldsymbol{\beta}^{\mathrm{Im}}}l(\mathbf{y};\boldsymbol{\Theta}))^T\right] \in \mathbb{R}^{MR \times MR}.$$

The expressions for the Jacobians are as follows:

$$\mathbf{D}_{\boldsymbol{\beta}^{\mathrm{Re}}} = \left[\frac{\partial \mathbf{h}}{\partial \beta_{1,1}^{\mathrm{Re}}}, \frac{\partial \mathbf{h}}{\partial \beta_{1,2}^{\mathrm{Re}}}, \ldots, \frac{\partial \mathbf{h}}{\partial \beta_{R,M}^{\mathrm{Re}}}\right],$$

$$\frac{\partial \mathbf{h}[k]}{\partial \beta_{r,m}^{\mathrm{Re}}} = g(kT_s - (\tau_0 + (r-1)\Delta')),$$

$$\mathbf{D}_{\boldsymbol{\beta}^{\mathrm{Im}}} = j\mathbf{D}_{\boldsymbol{\beta}^{\mathrm{Re}}},$$

where $\mathbf{e}_m$ is the unit vector with a 1 at the mth index.

3.2.2 Structured and Dictionary Based Channels

The regularity condition for the pdf of $\mathbf{y}$ can be easily verified. For the structured and the grid mismatched dictionary based channel models, $\mathbf{J}_D$ is block-partitioned and symmetric and is given by

$$\mathbf{J}_D = \begin{bmatrix} \mathbf{J}_{\boldsymbol{\theta}} & \mathbf{J}_{\boldsymbol{\theta}\boldsymbol{\tau}} & \mathbf{J}_{\boldsymbol{\theta}\boldsymbol{\gamma}^{\mathrm{Re}}} & \mathbf{J}_{\boldsymbol{\theta}\boldsymbol{\gamma}^{\mathrm{Im}}} & \mathbf{J}_{\boldsymbol{\theta}\boldsymbol{\rho}} \\ \mathbf{J}_{\boldsymbol{\theta}\boldsymbol{\tau}}^T & \mathbf{J}_{\boldsymbol{\tau}} & \mathbf{J}_{\boldsymbol{\tau}\boldsymbol{\gamma}^{\mathrm{Re}}} & \mathbf{J}_{\boldsymbol{\tau}\boldsymbol{\gamma}^{\mathrm{Im}}} & \mathbf{J}_{\boldsymbol{\tau}\boldsymbol{\rho}} \\ \mathbf{J}_{\boldsymbol{\theta}\boldsymbol{\gamma}^{\mathrm{Re}}}^T & \mathbf{J}_{\boldsymbol{\tau}\boldsymbol{\gamma}^{\mathrm{Re}}}^T & \mathbf{J}_{\boldsymbol{\gamma}^{\mathrm{Re}}} & \mathbf{J}_{\boldsymbol{\gamma}^{\mathrm{Re}}\boldsymbol{\gamma}^{\mathrm{Im}}} & \mathbf{J}_{\boldsymbol{\gamma}^{\mathrm{Re}}\boldsymbol{\rho}} \\ \mathbf{J}_{\boldsymbol{\theta}\boldsymbol{\gamma}^{\mathrm{Im}}}^T & \mathbf{J}_{\boldsymbol{\tau}\boldsymbol{\gamma}^{\mathrm{Im}}}^T & \mathbf{J}_{\boldsymbol{\gamma}^{\mathrm{Re}}\boldsymbol{\gamma}^{\mathrm{Im}}}^T & \mathbf{J}_{\boldsymbol{\gamma}^{\mathrm{Im}}} & \mathbf{J}_{\boldsymbol{\gamma}^{\mathrm{Im}}\boldsymbol{\rho}} \\ \mathbf{J}_{\boldsymbol{\theta}\boldsymbol{\rho}}^T & \mathbf{J}_{\boldsymbol{\tau}\boldsymbol{\rho}}^T & \mathbf{J}_{\boldsymbol{\gamma}^{\mathrm{Re}}\boldsymbol{\rho}}^T & \mathbf{J}_{\boldsymbol{\gamma}^{\mathrm{Im}}\boldsymbol{\rho}}^T & \mathbf{J}_{\boldsymbol{\rho}} \end{bmatrix}, \qquad (3.15)$$

where the expression for each matrix block is provided in Appendix A. Let $u_k = \left(\mathbf{s}^{(k)}\right)^T \mathbf{h}$,

$(\cdot)^{(i,)}$ be the ith row of the argument and $(\cdot)^{(,i)}$ be the ith column of the argument. Denoting the Jacobian of $\mathbf{h}$ with respect to $\boldsymbol{\theta}$ by $\mathbf{D}_{\boldsymbol{\theta}}$, it is shown in Appendix A that $\mathbf{J}_{\boldsymbol{\theta}}$ can be written as

$$[\mathbf{J}_{\boldsymbol{\theta}}]_{i,j} = \mathbb{E}\left[\frac{\partial l(\mathbf{y}; \boldsymbol{\Theta})}{\partial \theta_i} \frac{\partial l(\mathbf{y}; \boldsymbol{\Theta})}{\partial \theta_j}\right] = \left(\mathbf{D}_{\boldsymbol{\theta}}^{(,i)}\right)^T \mathbf{S}^T \ \boldsymbol{\Psi}_D \ \mathbf{S} \ \mathbf{D}_{\boldsymbol{\theta}}^{(,j)}, \tag{3.16}$$

where $\boldsymbol{\Psi}_D$ is a diagonal matrix with $[\boldsymbol{\Psi}_D]_{k,k} = \frac{2}{\sigma^2} \frac{\left(\Psi'\left(\frac{\sqrt{2}}{\sigma} u_k\right)\right)^2}{\Psi\left(\frac{\sqrt{2}}{\sigma} u_k\right)\left(1 - \Psi\left(\frac{\sqrt{2}}{\sigma} u_k\right)\right)}$. In a similar manner, expressions for the other sub-matrices of (3.15) in terms of $\mathbf{D}_{\boldsymbol{\theta}}$, $\mathbf{D}_{\boldsymbol{\tau}}$, $\mathbf{D}_{\boldsymbol{\gamma}^{\mathrm{Re}}}$ and $\mathbf{D}_{\boldsymbol{\gamma}^{\mathrm{Im}}}$ can be derived. For instance, the sub-matrix $\mathbf{J}_{\boldsymbol{\theta}\boldsymbol{\tau}}$ is given by

$$\mathbf{J}_{\boldsymbol{\theta}\boldsymbol{\tau}} = (\mathbf{D}_{\boldsymbol{\theta}})^T \mathbf{S}^T \ \boldsymbol{\Psi}_D \ \mathbf{S} \ \mathbf{D}_{\boldsymbol{\tau}}.$$

The expressions for the Jacobian matrices are derived in Appendix B, and are evaluated at the nominal perturbation value $\boldsymbol{\rho}_0$.

3.3 Simulation Results

A ULA with half-wavelength spacing between antenna elements, i.e. $\delta = 0.5\lambda$, $\lambda = c/f_c$ with the carrier frequency $f_c = 60\text{GHz}$ is considered. The source signal $s[n], n = -L+1, \ldots, N-1$, is taken to be a randomly generated quadrature phase shift keying (QPSK) sequence. The parameter r is chosen to be the raised cosine filter with roll-off factor $\alpha = 0.8$. For wideband systems, the channel bandwidths can be as high as 1GHz [132]. For this reason, in the simulations the null-to-null bandwidth is set to 1GHz, the symbol duration $T_s = 1\text{ns}$, and the received signal is oversampled at the sampling frequency $f_s = P \times \text{null} - \text{to} - \text{null bandwidth}$. The oversampling factor is $P = 3$ in all plots except Fig. 3.7.

A comparison of the CRBs of the different channel models is accomplished by translating the

CRB of the parameters $\boldsymbol{\Theta}$ into the CRB of the channel by the following transformation [126]

$$\text{CRB}(\mathbf{h}) \succeq \nabla_{\boldsymbol{\Theta}}\mathbf{h} \ \mathbf{J}^{-1} \ \nabla_{\boldsymbol{\Theta}}^{T}\mathbf{h},$$

where $\nabla_{\boldsymbol{\Theta}}(\cdot)$ is the Jacobian with respect to $\boldsymbol{\Theta}$. The parameters for the structured channel model are selected as follows. The angles of arrival of the multipaths are assumed to be distributed independently and uniformly in $[0, 2\pi)$. The R complex gains of the multipaths γ_r are assumed to be generated from a complex normal distribution. The path delays $\tau_r, r = 1, 2, \ldots, R$, are chosen to be integer multiples of the sampling interval $1/f_s$. For the first few simulations, the effect of array perturbations is ignored. Similarly, for the unstructured channel, the elements of the spatial signatures $\beta_{m,r}, m = 1, 2, \ldots, M, \ r = 1, 2, \ldots, R$, are also assumed to be generated independently and identically from a complex normal distribution with unit variance, and $\Delta' = 1/f_s$.

Finally, for the dictionary matrix in (3.9), $N_a = 2M$ and $N_d = 2L-1$. The angular and delay domain mismatch errors, $\boldsymbol{\theta}$ and $\boldsymbol{\tau}$, are generated independently and uniformly in $\left[-\frac{\pi}{2N_a}, \frac{\pi}{2N_a}\right]$ and $\left[-\frac{(L-1)T_s}{2N_d}, \frac{(L-1)T_s}{2N_d}\right]$, respectively. The square root of the trace of the CRB matrix for each of the parameters is computed and averaged over 50 realizations of the channel.

3.3.1 Performance vs. SNR

Fig. 3.2 (a) shows the square root of the trace of the channel estimate CRB as a function of the SNR for a single line-of-sight path $(R = 1)$ to the receiver and a single tap channel $(L = 1)$ with $M = 32$ receive antennas and pilot length $N = 20$. This is the frequency-flat fading case with the unstructured model corresponding to the Rayleigh fading case.

The increase in the bound at high SNR in Fig. 2 (a) is commonly observed in one-bit sampled systems, and is due to the loss of information in the channel gain as the amplitude of
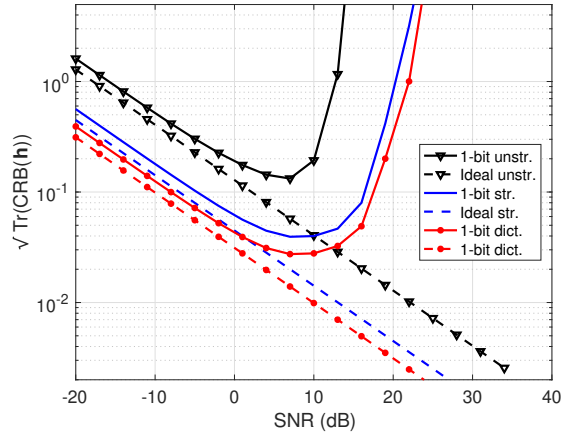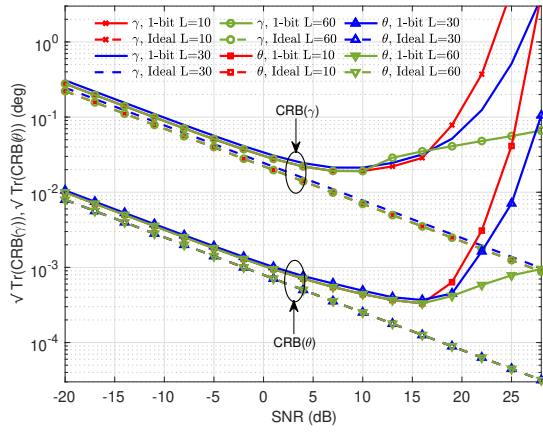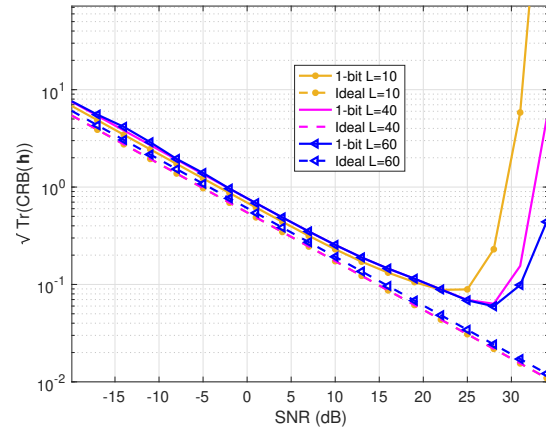
Figure 3.2: CRB($\mathbf{h}$), CRB($\boldsymbol{\theta}$) and CRB($\boldsymbol{\gamma}$) with $M = 32$ and single LOS path for different values of the channel delay-tap length. © IEEE.

the received signal grows, and the FIM becomes rank deficient. This illustrates the benefit behind dithering (stochastic resonance), where adding noise (lowering the SNR) can improve estimation performance with coarsely sampled data. It is also observed that at low-moderate SNRs, which is common in mmWave, the gap due to the quantization error between the unquantized and one-bit bounds is about 1.96dB as expected [133]. At higher SNRs, however, the gap is much higher since the FIM becomes increasingly ill-conditioned due to reduced identifiability of the channel gains. The CRBs for the unstructured one-bit and unquantized channels are higher than the other CRBs since they reflect the estimation error for a total of 64 real-valued parameters compared to only 3 structured and dictionary based channel parameters (2 real-valued path gains and one DOA). Furthermore, the dictionary based CRB is lower than the unstructured and structured counterparts. This is because approximate knowledge of the DOAs and delays is available and the CRB reflects the estimation error for the grid mismatch. Fig. 3.2 (a) provides a very interesting observation concerning the structured vs. unstructured models and one-bit quantization. Note that the channel estimation lower bound for the structured model under one-bit quantization is significantly lower than the bound for the unstructured model without quantization (perfect resolution), provided that the SNR is below 10dB, which would be the typical case for mmWave systems. Thus, the gain in parsimony provided by the structured model more than compensates for the loss due to the coarse quantization, and this provides a strong argument for the use of the structured model when the propagation environment is relatively simple.

When the channel is strongly frequency selective (large delay spread L), the received signal power is spread evenly over time, the quantization noise becomes circularly symmetric, and the resulting amplitude distortion caused by the quantization is reduced (see [39] for details). This is evident in the CRB results shown in Figs. 2 (b) and (c). Fig. 3.2 (b) illustrates the CRBs of $\boldsymbol{\gamma}$ and $\boldsymbol{\theta}$ for different channel lengths $L = 10$, $L = 30$ and $L = 60$. The number of pilots is set at $N = 80$ in all cases. It is seen that as the number of channel taps increases, the degradation in performance due to quantization at higher SNRs also decreases. For
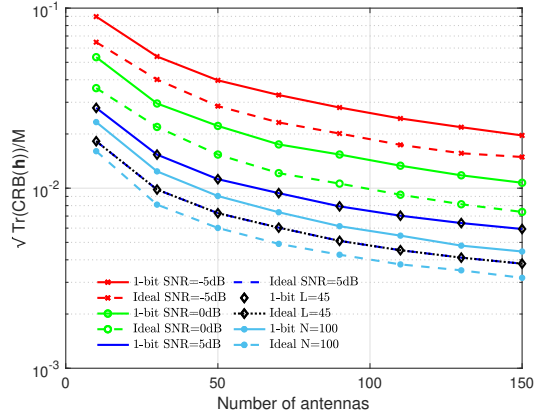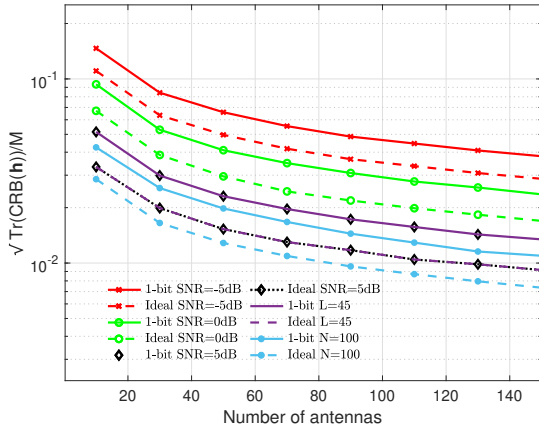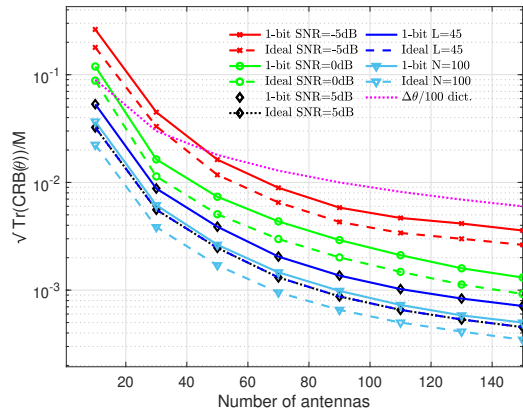
Figure 3.3: CRB($\mathbf{h}$) of structured and unstructured channels, and CRB($\boldsymbol{\theta}$) of structured channels as a function of the number of receive antennas. © IEEE.

the same number of pilots, no effect on the CRB is observed at low-to-moderate SNRs. The performance of the ideal system is insensitive to L, and therefore, the dashed curves corresponding to the ideal system overlap. A similar effect is seen Fig. 3.2 (c) where the CRB of the unstructured channel is plotted as a function of the SNR for different values of L. Here, a single multipath is considered with the number of pilots fixed to $N = 80$. Since the size of the $\boldsymbol{\beta}$ grows linearly with R and L, the CRB is normalized by MR. Thus, the effect of quantization error from one-bit ADCs in longer frequency-selective channels is less severe at high SNRs.

3.3.2 Performance vs Number of Antennas

The effect of increasing the number of antennas on the CRB is studied next. In Fig. 3.3 (a), the CRB normalized by the number of receive antennas ($\sqrt{\text{Tr}(\text{CRB}(\mathbf{h}))/M}$) is plotted for the structured channel case, for varying values of M at different SNRs and delay tap lengths. For the case with $L = 45$, the SNR is 5dB, and for the $N = 100$ case- $L = 15$ and SNR = 5dB. For the other plots, $L = 15$. The number of pilots is fixed to $N = 60$ and the number of multipaths is $R = 4$. As expected, increasing the number of antennas reduces the average estimation error in each channel coefficient. In [39], it was found that, for a given SNR, the number of antennas in one-bit systems with an unstructured channel model should increase by approximately 2.5 times to meet the achievable rate of an otherwise equivalent ideal unquantized system. At SNR $= -5$dB, fewer than twice the number of antennas are required for the one-bit system to achieve the same channel estimation performance as the unquantized system. For example, the one-bit CRB at $M = 80$ is equal to the unquantized CRB at $M = 50$. At 5dB SNR, it is seen that the number of antennas should be increased by slightly more than a factor of two; the one-bit CRB at $M = 110$ is equal to the unquantized CRB at $M = 50$. At 5dB SNR, even the highly frequency-selective channel ($L = 45$) has the same CRB as a channel with $L = 15$ as seen by the overlapping blue and black curves. At higher SNRs, it can be expected that one-bit systems are advantageous for highly frequency-selective channels.

The CRB is plotted as a function of M for unstructured channels in Fig. 3.3 (b). Since the number of parameters for the unstructured channel scales with M (more specifically, the number of parameters is $2MR$), the CRB is normalized by MR, and $N = 80$. As expected, increasing the number of antennas reduces the average estimation error in each channel coefficient. At low SNRs, the number of antennas needed by one-bit systems has to again increase by almost two times to cope with the loss due to quantization distortion. For instance, at SNR $= 0$dB, the one-bit system with $M = 100$ achieves the same CRB as the

unquantized system with $M = 50$. As the SNR is increased, it is found that the number of antennas should be increased even more to meet the CRB of the unquantized system.

Fig. 3.3 (c) shows the CRB for $\boldsymbol{\theta}$ as a function of the number of antennas with the case for $N = 100$ corresponding to $L = 15$ and SNR $= 5$dB. The constrained CRB is also illustrated for SNR $= 5$dB and $L = 15$. The dotted line indicates the scaled angular resolution of the dictionary based channel model. The figure also shows the grid spacing of the dictionary based channel model scaled appropriately. At SNR $= -5$dB, the number of antennas should be increased by less than 1.5 times to achieve the unquantized CRB, significantly less than for the channel itself in Fig. 3.3 (a). The one-bit CRB at $M = 110$ is equal to the unquantized CRB at $M = 90$. At 5dB, the factor increases to 1.5, still fewer than for the channel. It can be seen that the Jacobian scales linearly with M, and thus, the CRB reduces with a factor of M^2. Comparing Figs. 3.3 (a) and (c) with (b), it is seen that, to match the CRB of the unquantized systems, the unstructured models require almost $2.5 - 3$ times the number of antennas, whereas the structured models typically require much less than twice the number of antennas. Thus, this example illustrates another advantage of using the structured model together with one-bit quantization: fewer additional antennas are needed to achieve the same performance as an ideal unquantized system than in the case of an unstructured channel model. Note that in this example, the structured model provides DOA estimates that are well beyond the resolution of the grid used in the dictionary-based model, especially for larger array sizes.

3.3.3 Effect of Array Calibration Errors

The effect of array perturbations on the CRB is now considered. First, a gain pattern perturbation only with $\boldsymbol{\Omega} = \sigma_{\boldsymbol{\rho}}^2 \, \mathbf{I}_M$ is assumed. Here, $M = 64$, the number of pilots is $N = 50$, the channel length $L = 5$ and the number of multipaths $R = 5$. Fig. 3.4 shows
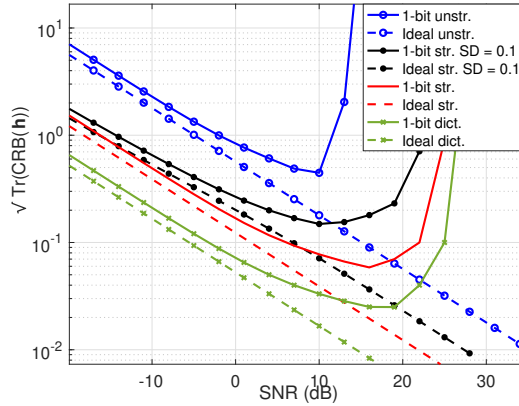
Figure 3.4: CRB($\mathbf{h}$) as a function of the SNR for varying standard deviations (SDs) of the pattern perturbation. © IEEE.

the CRB of the structured channel for a standard deviation of $\boldsymbol{\rho}$, $\sigma_{\boldsymbol{\rho}} = 0.1$. At $\sigma_{\boldsymbol{\rho}} = 0.1$, the structured model is an appropriate model to assess the channel performance at lower SNRs but the CRB degrades faster. On the other hand, the unstructured channel is a more suitable model when the perturbations are large and unknown. Fig. 3.4 amplifies the result of Fig. 3.2 (a), showing that the structured model with one-bit quantization achieves better channel estimation performance than the ideal unstructured model up to about 10dB SNR even when there are array perturbations at the level of $\sigma_{\boldsymbol{\rho}} = 0.1$. Thus, for low-to-moderate SNRs where mmWave systems operate, structured models that have even imprecise calibration and use only one-bit quantization perform better than using unstructured models with perfect quantization.

The effect of position perturbation on the CRB is also studied. The CRBs of $\boldsymbol{\gamma}$ and $\boldsymbol{\theta}$ as a function of the standard deviation, $\sigma_{\boldsymbol{\rho}}$, are plotted in Fig. 3.5 (a) and (b), respectively, for two different values of the SNR, 5dB and 10dB. It is seen in Fig. 3.5 (a) that for small values of $\sigma_{\boldsymbol{\rho}}$, increasing the SNR is advantageous since the CRB is lower at SNR $= 10$dB than at SNR $= 5$dB. However, more interestingly, increasing the perturbation causes the CRB to degrade rapidly at SNR $= 10$dB due to the near-singularity of the FIM. The same effect was observed in Fig. 3.4. Similarly, the CRB of $\boldsymbol{\theta}$ also degrades for SNR $= 10$dB with
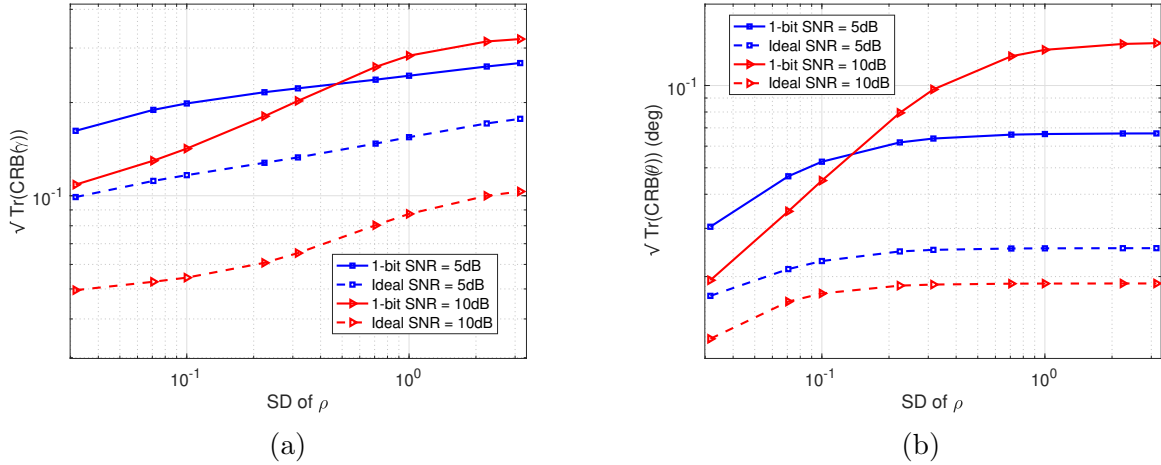
Figure 3.5: (a) CRB($\boldsymbol{\gamma}$) as a function of the SD of $\boldsymbol{\rho}$. (b) CRB($\boldsymbol{\theta}$) antennas as a function of the SD of $\boldsymbol{\rho}$. © IEEE.

an increasing perturbation in Fig. 3.5 (b). The gap between the one-bit and unquantized CRBs is greater for SNR = 10dB and it becomes more pronounced upon increasing the perturbation.

3.3.4 Effect of bandwidth and oversampling

Fig. 3.6 (a) and (b) show the CRBs of $\boldsymbol{\gamma}$ and $\boldsymbol{\theta}$, and $\boldsymbol{\tau}$ respectively, as a function of the signal bandwidth for $M = 32$ and $M = 64$ in the structured channel model. The delay spread is fixed to 0.2μs and the SNR is 0dB. The number of pilots is $N = 60$ and it is assumed that $R = 4$ multipaths are present. The null-to-null bandwidth is varied from 1MHz to 1GHz and the oversampling factor is kept at $P = 3$. Since the delay spread is kept constant, the channel length increases with the bandwidth, making the channel more frequency-selective. For both $\boldsymbol{\gamma}$ and $\boldsymbol{\theta}$, increasing the BW from 1MHz to 1GHz decreases the CRB by almost an order of magnitude. Therefore, for a given number of estimation parameters, a broadband system exhibits a lower estimation error for structured channel parameters than a narrowband system. Similarly, increasing the bandwidth also provides better resolution for the estimation of the delay parameters $\boldsymbol{\tau}$ as seen in Fig. 3.6(b).
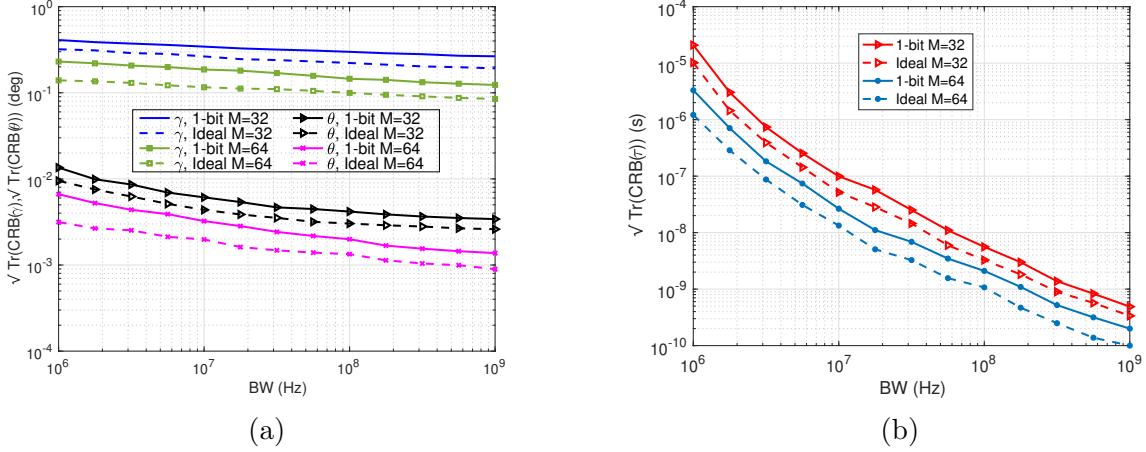
Figure 3.6: (a) CRB($\boldsymbol{\gamma}$) and CRB($\boldsymbol{\theta}$) of the structured channels as a function of the system bandwidth for a fixed delay spread. (b) CRB($\boldsymbol{\tau}$) as a function of the system bandwidth. © IEEE.

The effect of oversampling on the CRB is shown in Fig. 3.7. The plots with the $\triangledown$ and $*$ markers represent parameters $\boldsymbol{\tau}$ and $\boldsymbol{\gamma}$, respectively. The plots for $\boldsymbol{\theta}$ are unmarked. For SNR $= -20$dB, χ for all parameters are equal. Here, the gap between the one-bit CRB and the unquantized CRB is plotted as a function of the oversampling factor. More specifically, $\text{Tr}[\text{CRB}_{1-\text{bit}}(\cdot)]/\text{Tr}[\text{CRB}_{\infty}(\cdot)]$ for $\boldsymbol{\tau}, \boldsymbol{\gamma}$ and $\boldsymbol{\theta}$ is plotted. The number of antennas is kept fixed at 32 and the oversampling factor above the Nyquist rate is varied from 1 to 5. It is seen that performance loss from quantization is the least at SNR $= -20$dB and increases upon increasing the SNR. However, the effect of oversampling is to reduce the loss beyond the $2/\pi$ limit. At low SNRs, for example at -20dB, increasing the oversampling factor does not have any effect and the plots for all parameters coincide. However, improvements would still be possible at low SNRs if the analog filter prior to sampling is optimized [134].

3.3.5   Effect of path separation and number of multipaths

A disadvantage of the structured channel model is that the FIM becomes ill-conditioned when two multipaths arrive with similar DOAs and path delays. Fig. 3.8 illustrates the
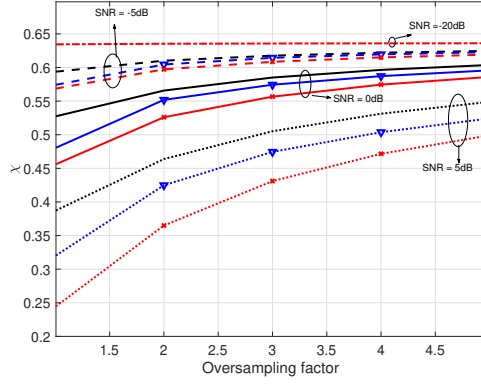
Figure 3.7: $\chi_{\mathbf{p}} = \frac{\text{Tr}[\text{CRB}_{1-\text{bit}}(\mathbf{p})]}{\text{Tr}[\text{CRB}_{\infty}(\mathbf{p})]}$ for $\mathbf{p} \in \{\boldsymbol{\gamma}, \boldsymbol{\theta}, \boldsymbol{\tau}\}$ of structured channels as a function of the oversampling factor, P. © IEEE.
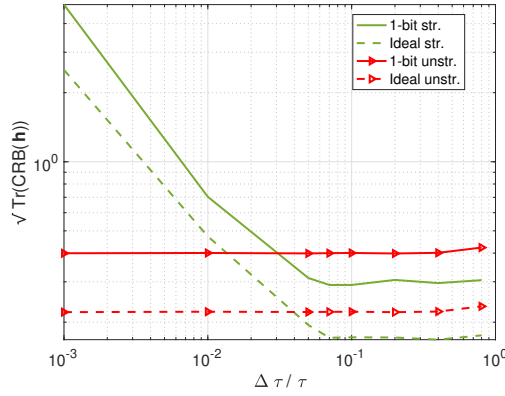
Figure 3.8: The CRB of the channel as a function of the fractional separation between path delays. The SNR is 0dB, $M = 64$, $N = 40$ and $L = 10$. © IEEE.

CRB as a function of the fractional path delay difference. In this setup, $R = 2$ and the two paths have different path gains but are configured to have the same DOA under the structured model. It is seen that as the path delays become closer, the structured model is not accurate and the unstructured model is better suited for resolving the two paths. When the paths are well separated in time, the structured channel model yields better results. For the given example, it is seen that the structured model only begins to break down when the difference in path delays is on the order of $3 - 4\%$ of the symbol period, but this illustrates the necessity of choosing the proper model order for the structured case, which is the key drawback of this method.

(a)   (b)
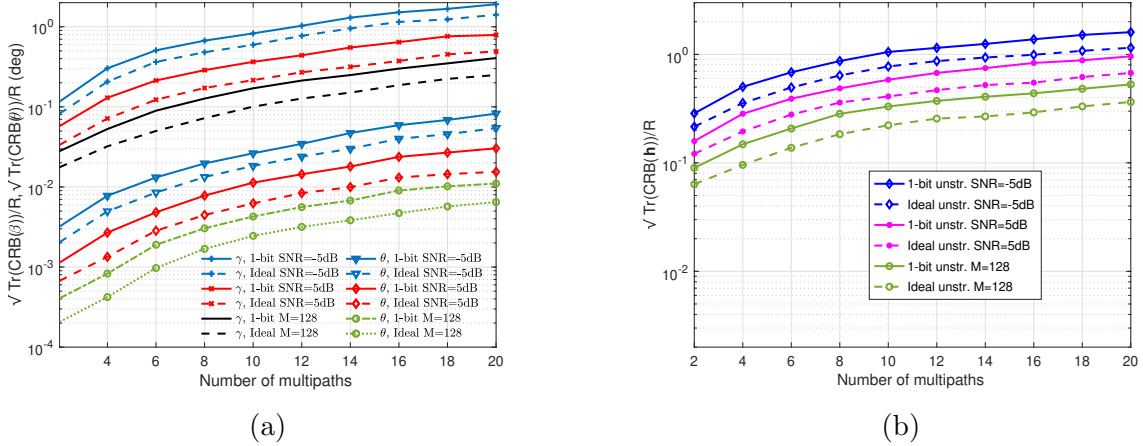
Figure 3.9: (a) CRB(γ) and CRB(θ) as a function of the number of multipaths. For the $M = 128$ plots, the SNR = 5dB. (b) CRB($\mathbf{h}$) of unstructured channels as a function of the number of multipaths. © IEEE.

Fig. 3.9 (a) and (b) show the normalized CRB ($\sqrt{\text{Tr}(\text{CRB}(\mathbf{h}))/R}$) as a function of the number of multipaths for $M = 64$, $N = 80$ and $L = 25$. It is seen that the CRB increases almost linearly on the log scale as the number of parameters also increases linearly with R.

3.4   Conclusion

In this chapter, performance bounds for channel estimation in one-bit mmWave massive MIMO systems were considered. A comparison in the CRBs of the structured, unstructured and dictionary-based channels as a function of the SNR indicated that the structured CRB is lower than that of the unstructured channel since fewer parameters contribute to the expression of the CRB. The effects of perturbation, bandwidth, the channel length, and the number of receive antennas on the CRBs of the one-bit quantized system were also considered. It was found that pertubation caused the CRB to degrade and approach that of an unstructured model at high SNRs. However, at low-to-moderate per-antenna SNRs, which is common in mmWave, the structured one-bit channel models have better channel estimation performance than the unquantized unstructured models. Furthermore, increasing

the bandwidth and the oversampling factor caused the estimation error variance to decrease due to improved temporal resolution. It is also seen that to achieve the same error variance as an unquantized system, the one-bit structured system required significantly less than twice the number of antennas.

One of the principal observations of the results is that a significantly lower channel estimation error can be achieved by using a structured rather than an unstructured channel model, even when the underlying array calibration is not precisely known. Thus, the extra computational cost required for the resulting non-linear optimization is often well worth the effort. The study of dependencies between the various system parameters can be useful in the design of channel estimation for mmWave massive MIMO with one-bit quantizers at the receiver.

Part II

Spatial Sigma-Delta modulation

Chapter 4

Sigma-Delta Modulation Preliminaries

In this chapter, some concepts on $\Sigma\Delta$ modulation, beginning with its temporal implementation, will be reviewed. The extension of $\Sigma\Delta$ modulation to the spatial domain, or *spatial* $\Sigma\Delta$ *modulation*, will be examined and an equivalent linear model for the output of the modulator will be developed.

Oversampling factor P

$x(t) \longrightarrow$ | ADC | $\xrightarrow{y[n]}$ | LPF $\omega_c = \pi/P$ | $\longrightarrow$ | $\downarrow P$ | $\longrightarrow y_d[n]$
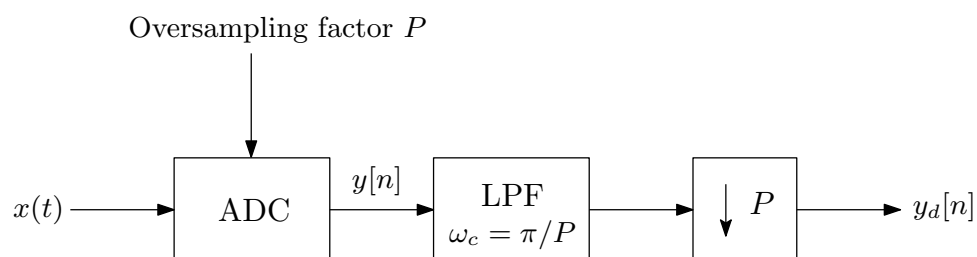
Figure 4.1: Oversampled direct quantizer followed by an LPF and a decimation stage.

4.1 Temporal Sigma-Delta Modulation

In the previous chapter, it was shown that oversampling can recuperate some of the loss in the signal-to-quantization-noise ratio (SQNR). Consider an oversampled ADC, operating with an oversampling factor P, with direct quantization followed by a low pass filter (LPF) and a decimator as in Fig. 4.1. It is usually assumed that $x(t)$ is bandlimited to frequency ω Hz, and the sampling frequency is $f_s = \omega P/\pi$ Hz. With an additive signal-plus-quantization noise model such as

$$y[n] = x[n] + q[n],$$

it can be shown that the signal power remains unaltered as it traverses the system but the same is not true for the noise component generated by quantization [121]. The quantization noise is usually modeled as a wide-sense stationary white-noise process with zero-mean and variance σ_q^2. The variance and power spectral density (PSD) of $q[n]$, $\phi_q(\Omega)$, are given by

$$\sigma_q^2 = \Delta^2/12$$
$$\phi_q(\Omega) = \sigma_q^2, \quad |\Omega| < \pi.$$

The PSD of the signal and the PSD of the quantization noise before and after the decimation stage are illustrated in Fig. 4.2. Although neither the signal nor the quantization noise power in (a) depend on P, the overlap between the two PSDs decreases as P increases. The combination of oversampling and sampling-rate reduction improves the SQNR. More specifically, the LPF removes the quantization noise in the band $\pi/P < \Omega \leq \pi$ while leaving the signal component unaltered. It is easy to show that the noise power at the output of the LPF is equal to σ_q^2/P [121]. Downsampling changes the PSD of both the signal and quantization noise component as seen in Fig. 4.2(b). The noise power at the decimated output is obtained by finding the area under the power density spectrum, and is the same
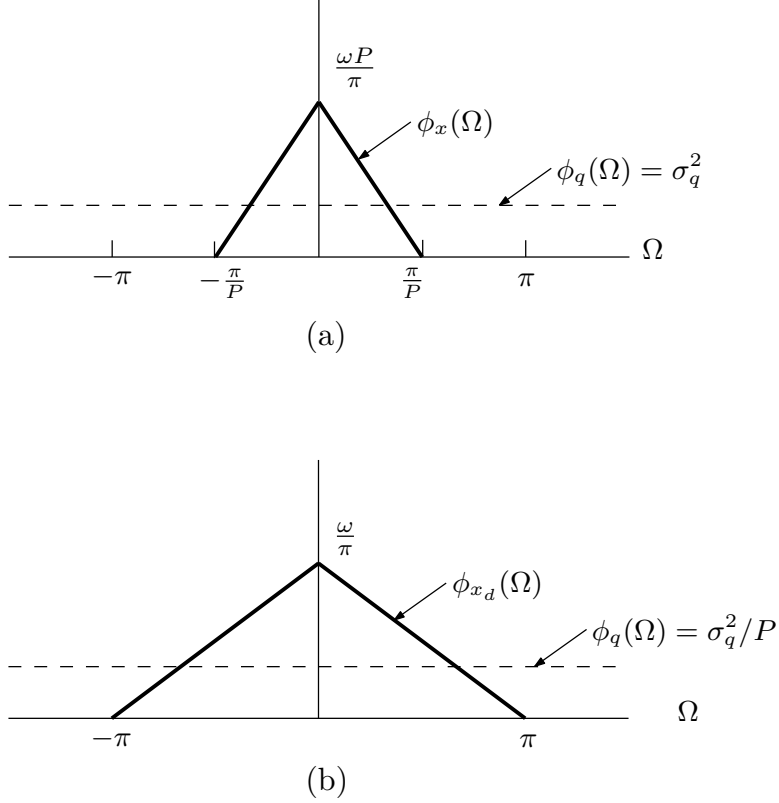
Figure 4.2: Direct quantization: (a) PSD before decimation. (b) PSD after decimation.

as that at the output of the LPF equal to $\sigma_q^2/P = \Delta^2/(12P)$. Therefore, the process of filtering and downsampling has reduced the quantization noise power by a factor of P, while retaining the signal power.

Alternatively, if the A/D conversion is modified such that the power spectrum of the quantization noise is no longer uniform but concentrated outside the frequency band of the desired signal, the SQNR could be improved even more. These higher gains can be obtained if oversampling is combined with noise spectrum shaping via feedback. The well-known $\Sigma\Delta$ modulator achieves this noise-shaping and is illustrated in Fig. 4.3 (a). It consists of an oversampled ADC, which is usually a low-resolution quantizer, and a DAC which converts the digital output back to the analog domain and subtracts it from the input signal. This causes the noise to be shaped such that it is concentrated at higher frequencies and can be subsequently removed with the help of an LPF and decimator. The equivalent discrete-time

system for Fig. 4.3(a) is shown in Fig. 4.3(b).

In the negative feedback loop, the difference between the output and input of the quantizer is subtracted from the input $x[n]$ after a one-sample delay. The operation of the quantizer is defined using the following equivalent linear model with gain $\gamma > 0$, even though γ is usually taken to be 1. For the spatial $\Sigma\Delta$ application, we will see that γ plays a crucial role in the stability of the feedback system. In commercial quantizers, however, selection of the parameter γ is usually achieved with the help of an AGC (see Fig. 1.2). The output of the ADC can be expressed as [103]

$$
\begin{aligned}
y[n] = \mathcal{Q}\left(r[n]\right) &= \gamma r[n] + q[n] \\
&= \gamma(x[n] + r[n-1] - y[n-1]) + q[n] \\
&= \gamma(x[n] + \frac{y[n-1] - q[n-1]}{\gamma} - y[n-1]) + q[n].
\end{aligned}
$$

In transfer function notation, this relationship can be expressed as

$$
\begin{aligned}
Y(z) &= \frac{\gamma}{1 - (\gamma - 1)z^{-1}}X(z) + \frac{(1 - z^{-1})}{1 - (\gamma - 1)z^{-1}}Q(z) \\
&= A_x(z)X(z) + A_q(z)Q(z) ,
\end{aligned}
$$

where $\{Y(z), X(z), Q(z)\}$ respectively represent the z-transforms of $\{y[n], x[n], q[n]\}$. When $\gamma = 1$, we have that $A_x(z) = 1$ is an all-pass filter and that $A_q(z) = 1 - z^{-1}$ is a first-order high-pass filter, which is the standard result, indicating the quantization noise is shaped to higher frequencies. Given that $x[n]$ is oversampled and is concentrated at lower frequencies, the effect of the quantization noise can be substantially reduced by passing the output of the $\Sigma\Delta$ modulator through a low-pass filter. The all-pass plus high-pass structure still remains true as long as $\gamma \approx 1$, but the $\Sigma\Delta$ modulator clearly approaches instability as $\gamma \to 2$.

(a)

(b)
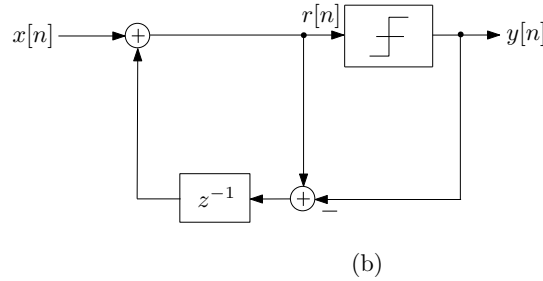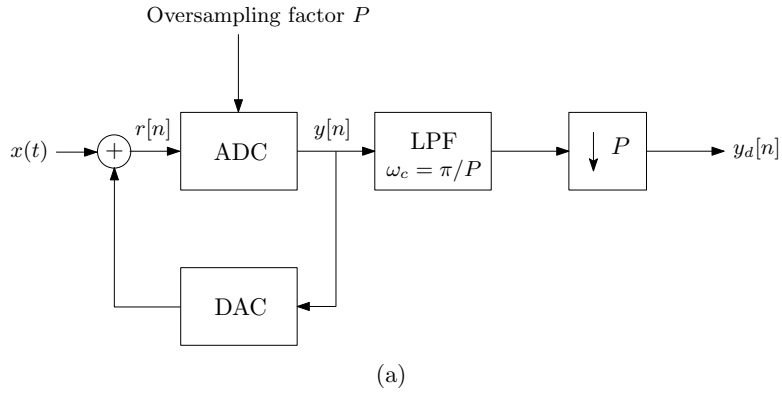
Figure 4.3: (a) Temporal $\Sigma\Delta$ modulator. (b) Equivalent block diagram

(a)

(b)
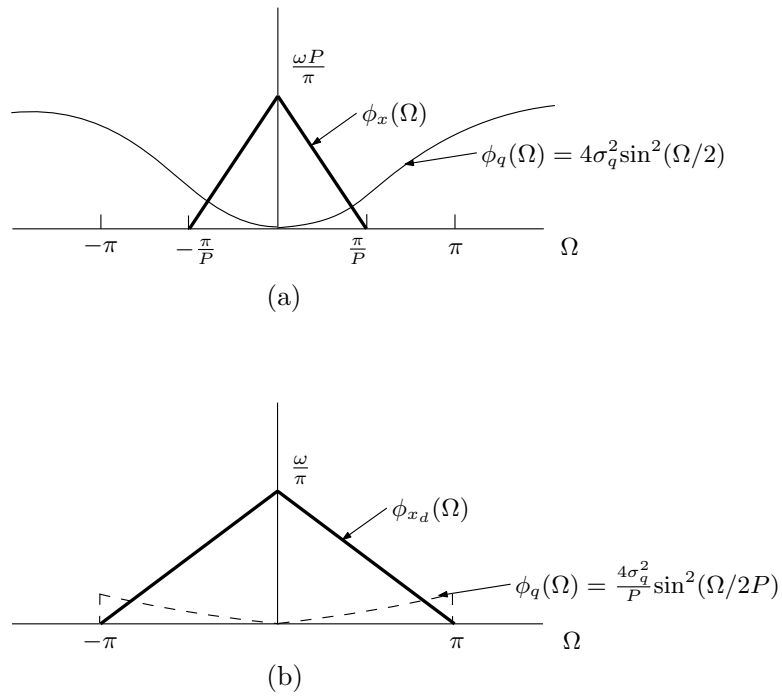
Figure 4.4: Temporal $\Sigma\Delta$: (a) PSD before decimation (b) PSD after decimation.

60
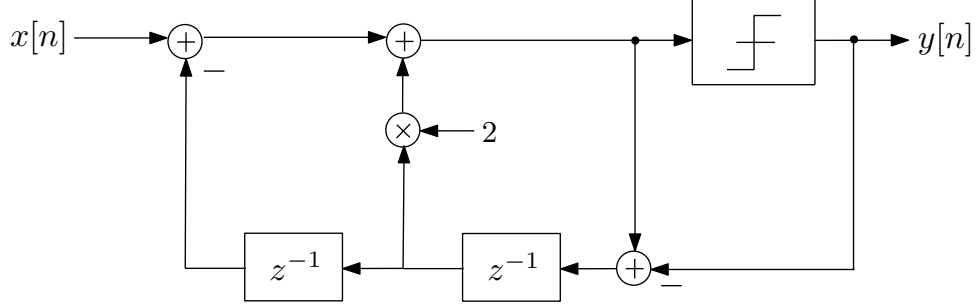
Figure 4.5: Second-order temporal $\Sigma\Delta$ modulator.

Like in the oversampled direct quantization case, the noise shaping effect is also evident when the PSDs before and after decimation, shown in Fig. 4.4, are inspected. The power density spectrum before decimation can be shown to be [121]

$$\phi_q(\Omega) = 4\sigma_q^2 \sin^2(\Omega/2),$$

where the quantization noise is shaped in such a manner that most of the noise power is concentrated outside the frequency band of the desired signal. The quantization noise power in the filtered and decimated output is even lower as seen in Fig. 4.4.

The noise shaping effect can be extended by using a second stage of integration as in Fig. 4.5. The noise transfer function for the second-order $\Sigma\Delta$ modulator is

$$A_q(z) = (1 - z^{-1})^4.$$

Although even more error accumulation stages can be used to achieve greater noise reduction, there is also an increased potential for instability and oscillations. This applies to the spatial implementation of $\Sigma\Delta$ modulation as well and therefore, the discussion on spatial $\Sigma\Delta$ ADCs will be restricted to first-order architectures.

61

4.2 Spatial Sigma-Delta Modulation

In temporal $\Sigma\Delta$ modulation, the temporal correlation between adjacent samples of the input signals was exploited through oversampling. An analogous effect could be achieved in the spatial domain by placing the antennas closer than half the wavelength. This approach exploits oversampling in space, which arises when large arrays are deployed with a limited aperture, or when the uplink signals are confined to some angular sector, due to cell sectorization or certain small-cell geometries (narrow conference halls, city streets, etc.). The spatial $\Sigma\Delta$ architecture is depicted in Fig. 4.6, and shows that the quantization error from one antenna is phase-shifted by $-\psi$ prior to being added to the input of the adjacent antenna, rather than to the input of the same antenna. This architecture shapes the quantization noise away from the angle of arrival (AoA) associated with the phase shift ψ, and thus users in an angular sector surrounding this AoA experience a significantly higher SQNR. If the feedback is not phase-shifted, this has the effect of shaping the quantization noise to high spatial frequencies, in favor of signals with low spatial frequencies (e.g., angles closer to the broadside of a uniform linear array). The size of the high-SQNR angular sector can be increased by placing the antennas closer together than $\lambda/2$, corresponding to spatial oversampling, although in practice mutual coupling and the physical dimensions of the antennas place a limit on how much spatial oversampling can be achieved. For this reason, the $\Sigma\Delta$ array is best suited for situations where both factors are present: the array has some spatial oversampling and the users of interest are confined to some angular sector. Note that the sector need not be near the array broadside since the region of low quantization noise can be steered to arbitrary directions.

To generate a mathematical model for the $\Sigma\Delta$ array, define the $M \times 1$ vectors $\mathbf{r}$ and $\mathbf{y}$ corresponding respectively to the quantizer inputs and the array outputs that result from the $M \times 1$ received signal vector $\mathbf{x}$. In other words, the mth elements $\{x_m, r_m, y_m\}$ of the vectors $\{\mathbf{x}, \mathbf{r}, \mathbf{y}\}$ respectively represent the signal received by the mth antenna, the input to
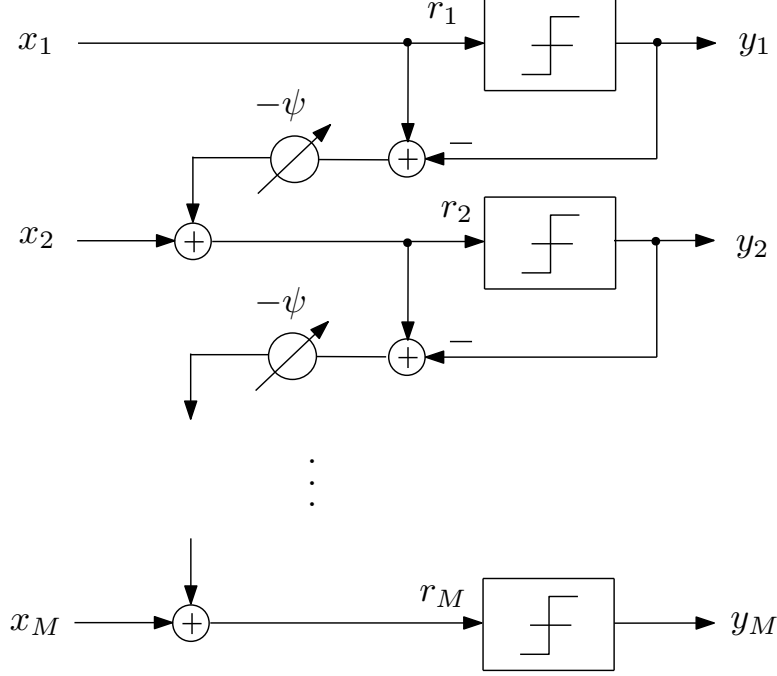
Figure 4.6: First-order spatial $\Sigma\Delta$ ADC array.

the quantizer at the mth antenna, and the $\Sigma\Delta$ output of the mth antenna. The output y_m can be written as

$$y_m = \mathcal{Q}_m\left(\mathrm{Re}(r_m)\right) + j\mathcal{Q}_m\left(\mathrm{Im}(r_m)\right), \tag{4.1}$$

where $\mathcal{Q}_m$ represents the quantization operation for the mth antenna. The input to the mth ADC r_m can be expressed in terms of the quantization noise q_{m-1} from the previous stage as

$$
\begin{aligned}
r_m &= x_m + e^{-j\psi} q_{m-1} \\
&= x_m + e^{-j\psi}\left(r_{m-1} - y_{m-1}\right) \\
&= x_m + e^{-j\psi}\left(x_{m-1} + r_{m-2} - y_{m-2} - y_{m-1}\right).
\end{aligned}
\tag{4.2}
$$

In vector notation, the output of the $\Sigma\Delta$ array can be conveniently written as

$$\mathbf{y} = \mathcal{Q}(\mathbf{r}) \tag{4.3}$$
$$= [\mathcal{Q}_1(r_1), \dots, \mathcal{Q}_M(r_M)]^T \; ,$$

where

$$\mathbf{r} = \mathbf{U}_d\mathbf{x} - \mathbf{V}_d\mathbf{y}$$

$$\mathbf{V}_d = \begin{bmatrix} 0 & 0 & \dots & 0 & 0 \\ e^{-j\psi} & 0 & \dots & 0 & 0 \\ e^{-j2\psi} & e^{-j\psi} & \dots & 0 & 0 \\ & & \vdots & & \\ e^{-j(M-1)\psi} & e^{-j(M-2)\psi} & \dots & e^{-j\psi} & 0 \end{bmatrix}$$

$$\mathbf{U}_d = \mathbf{I}_M + \mathbf{V}_d. \tag{4.4}$$

An equivalent linear signal-plus-quantization-noise model will be used to represent the output $\mathbf{y}$ in terms of the ADC input $\mathbf{r}$. Mathematically, the linear model is given by

$$\mathbf{y} = \mathbf{\Gamma}\mathbf{r} + \mathbf{q}, \tag{4.5}$$

where $\mathbf{q}$ is the equivalent quantization noise vector. There is an infinite number of design choices for the matrix $\mathbf{\Gamma}$ with each selection leading to a different linear model. However, two models based on the Bussgang decomposition will be considered below.

4.2.1 Vector-wise Bussgang decomposition

One method to select $\mathbf{\Gamma}$ is to use a vector-wise Bussgang decomposition as described in Section 2.2. According to this model, $\mathbf{\Gamma}$ is a matrix chosen to make $\mathbf{q}$ uncorrelated with $\mathbf{r}$, i.e., $\mathbf{\Gamma} = \mathbf{C}_{ry}^H \mathbf{C}_r^{-1}$, where $\mathbf{C}_{ry}$ is the cross-correlation matrix between $\mathbf{r}$ and $\mathbf{y}$ and $\mathbf{C}_r$ is the auto-correlation matrix of $\mathbf{r}$. For a $\Sigma\Delta$ ADC array equipped with one-bit ADCs, these matrices can be expressed in closed-form by extending the Bussgang decomposition proposed in [27]. Assuming that the elements of $\mathbf{r}$ are jointly Gaussian and defining $\mathbf{C}_y$ to be the auto-correlation matrix of $\mathbf{y}$, the following relations can be obtained

$$
\begin{aligned}
\mathbf{\Gamma} &= \sqrt{\frac{2}{\pi}} \mathrm{diag}\left(\mathbf{C}_r\right)^{-0.5}, \\
\mathbf{C}_y &= \frac{2}{\pi}\left[\arcsin\left(\frac{\pi}{2}\mathbf{\Gamma}\mathrm{Re}(\mathbf{C}_r)\mathbf{\Gamma}^H\right) + j\arcsin\left(\frac{\pi}{2}\mathbf{\Gamma}\mathrm{Im}(\mathbf{C}_r)\mathbf{\Gamma}^H\right)\right], \\
\mathbf{C}_r &= \mathbf{U}_d\mathbf{C}_x\mathbf{U}_d^H + \mathbf{V}_d\mathbf{C}_y\mathbf{V}_d^H - \mathbf{U}_d\mathbf{C}_{xy}\mathbf{\Gamma}^H - \mathbf{V}_d\mathbf{C}_{xy}^H\mathbf{U}_d^H,
\end{aligned}
\tag{4.6}
$$

where $\mathbf{C}_{xy}$ is

$$
\mathbf{C}_{xy} = (\mathbf{C}_x\mathbf{U}_d^H\mathbf{\Gamma}^H + \mathbf{U}_d^{-1}\mathbf{V}_d\mathbf{C}_q)(\mathbf{I} + \mathbf{V}_d^H\mathbf{\Gamma}^H)^{-1}.
\tag{4.7}
$$

We note here that there is a complicated inter-relationship between $\mathbf{C}_y$ and $\mathbf{C}_z$ for the $\Sigma\Delta$ array that is the primary difficulty for calculating the matrix $\mathbf{\Gamma}$. We show below that, while it is not possible to obtain closed form expressions for $\mathbf{C}_y$ and $\mathbf{C}_z$, their elements can be computed recursively. In [101], the derivation based on this recursion was shown for the problem of channel estimation using orthogonal pilots. This derivation will not be shown here, but it is necessary to make an important observation regarding this kind of decomposition. The vector-wise Bussgang decomposition shown above is based on the observation that $\mathbf{q}$ is uncorrelated with $\mathbf{r}$, which is not consistent with the traditional definition of quantization noise. From (4.2), this definition for the quantization noise does not have a physical interpretation in the context of Fig. 4.6. This is better illustrated with the help of the ex-
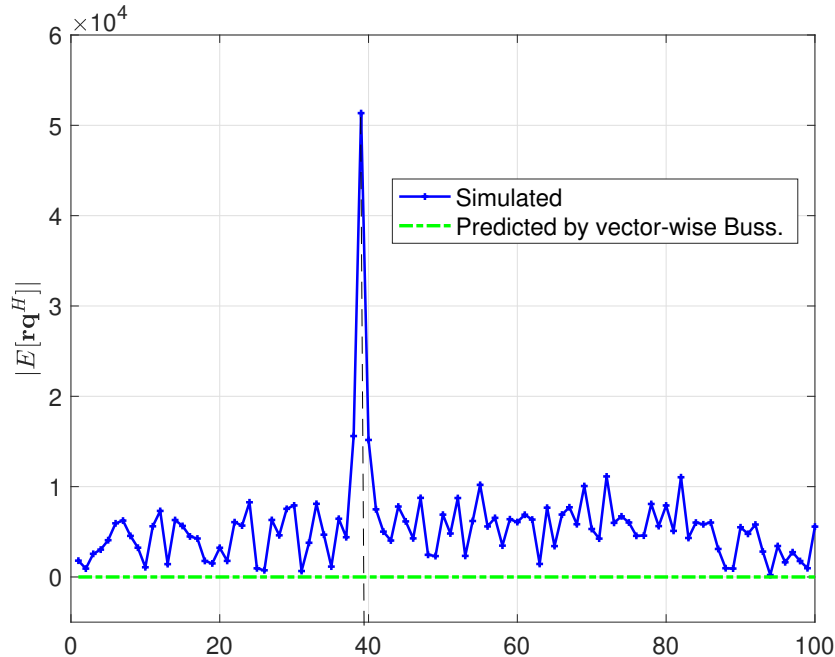
Figure 4.7: Cross-correlation between $\mathbf{r}$ and $\mathbf{q}$ with vector-wise Bussgang decomposition.

ample in Fig. 4.7, where values from a particular row of cross-correlation between $\mathbf{r}$ and $\mathbf{q}$ are plotted. More specifically, the correlation between r_m and $\mathbf{q}$ for $m = 40$ is plotted and it is seen that r_{40} is highly correlated with q_{39} and less correlated with the quantization noise from other antenna indices. Thus, the assumption that $\mathbf{r}$ and $\mathbf{q}$ are uncorrelated is clearly invalid.

4.2.2   Element-wise Bussgang decomposition

There is a need to incorporate a more meaningful definition of the quantization noise and it can be performed using an element-wise implementation of the Bussgang decomposition as defined in [103] and described in this section. This approach explicitly takes into account the spatial correlation between the quantized outputs of the $\Sigma\Delta$ ADC array. In order to do

this, the quantization operation will be defined as:

$$y_m = \alpha_m \mathcal{Q}_m \left(\mathrm{Re}(r_m) \right) + j \alpha_m \mathcal{Q}_m \left(\mathrm{Im}(r_m) \right), \tag{4.8}$$

where α_m is the output level of the quantizer. Note that α_m is allowed to be different for each antenna, unlike conventional one-bit quantization where they are the same.

The Bussgang decomposition can be applied element-wise such that $\mathbb{E}\left[r_m q_m^*\right] = 0$. With this definition, $\mathbf{\Gamma}$ becomes a diagonal matrix whose mth diagonal element, γ_m, is given by

$$\gamma_m = \frac{\mathbb{E}\left[r_m y_m^*\right]}{\mathbb{E}\left[|r_m|^2\right]}. \tag{4.9}$$

Plugging $\mathbf{r} = \mathbf{U}_d \mathbf{x} - \mathbf{V}_d \mathbf{y}$ into (4.5), we get

$$\mathbf{y} = \left(\mathbf{I} + \mathbf{\Gamma} \mathbf{V}_d \right)^{-1} \mathbf{\Gamma} \mathbf{U}_d \mathbf{x} + \left(\mathbf{I} + \mathbf{\Gamma} \mathbf{V}_d \right)^{-1} \mathbf{q}. \tag{4.10}$$

The specific numerical value for γ_m will depend on the output level α_m. An α_m will be chosen such that $\gamma_m = 1$, or equivalently such that $\mathbf{\Gamma} = \mathbf{I}_M$, and (4.10) can be simplified to

$$\mathbf{y} = \mathbf{x} + \mathbf{U}_d^{-1} \mathbf{q} . \tag{4.11}$$

This is a convenient choice since the model is now the exact spatial analog of the temporal $\Sigma\Delta$ architecture, and is equivalent to passing $\mathbf{x}$ through a (spatial) all-pass filter and $\mathbf{q}$ through a filter that shapes the quantization noise away from the AoA corresponding to ψ. While this choice for α_m is an elegant one and provides good performance in our simulation results, there is no proof of its optimality. Such a proof appears to be difficult to obtain, so it is left for future work. Nevertheless, a choice of γ different from 1 seems difficult to justify since it would imply that the signal $\mathbf{x}$ is spatially filtered by the ADC architecture in some unclear way. As shown in the following sections for one- and two-bit quantization,

the value of α_m depends in general on the statistics of the signal r_m, which would have to remain time-invariant for the quantizer gains to be fixed. This can be achieved in practice using an AGC at the input to the ADC.

One-Bit Spatial $\Sigma\Delta$ ADCs

When the $\Sigma\Delta$ array is implemented with one-bit ADCs, the output is given by

$$y_m = \alpha_m \left(\text{sign}(\text{Re}(r_m)) + j\text{sign}(\text{Im}(r_m))\right), \tag{4.12}$$

and (4.9) can be simplified to

$$\begin{aligned}
\gamma_m &= \alpha_m \frac{\mathbb{E}\left[|\text{Re}(r_m)| + |\text{Im}(r_m)|\right]}{\mathbb{E}\left[|r_m|^2\right]} \\
&= \alpha_m \frac{\mathbb{E}\left[|\text{Re}(r_m)|\right]}{\mathbb{E}\left[|\text{Re}(r_m)|^2\right]}
\end{aligned} \tag{4.13}$$

for circularly symmetric r_m. Since the power of the pilot symbols is time-invariant, the statistics of r_m are identical to those of r_m. Consequently, we can set $\gamma_m = 1$, which leads to

$$\alpha_m = \frac{\mathbb{E}\left[|\text{Re}(r_m)|^2\right]}{\mathbb{E}\left[|\text{Re}(r_m)|\right]}. \tag{4.14}$$

If r_m were Gaussian, (4.14) could be simplified to

$$\alpha_m = \frac{\sqrt{\pi \mathbb{E}\left[|r_m|^2\right]}}{2}. \tag{4.15}$$

This was the value for α_m used in [103], and it provides sufficiently accurate estimates of the spectral efficiency for the case where the CSI is already known. However, the deviation of r_m from Gaussianity, while not large, is sufficient to render (4.15) unsuitable for channel

estimation. The derivation of (4.15) relies on the fact that

$$\frac{\sqrt{\mathbb{E}\left[|\mathrm{Re}(r_m)|^2\right]}}{\mathbb{E}\left[|\mathrm{Re}(r_m)|\right]} = \sqrt{\frac{\pi}{2}} \tag{4.16}$$

for Gaussian random variables. However, due to the non-linear feedback of the $\Sigma\Delta$ array, the tails of the distribution of r_m are slightly heavier than a Gaussian, so the ratio on the left hand side of (4.16) is slightly greater than $\sqrt{\pi/2}$.

Whether Eq. (4.14) or (4.15) is used to calculate α_m, in a practical implementation some empirical measurement of the mean power and absolute value of r_m in the $\Sigma\Delta$ architecture would be necessary, and could be facilitated by the use of an automatic gain control. Rather than implementing the computation of α_m according to (4.14), in our simulations of the one-bit case presented later, α_m is simply computed as

$$\alpha_m^* = \beta \frac{\sqrt{\pi \mathbb{E}\left[|r_m|^2\right]}}{2}, \tag{4.17}$$

with a value of $\beta > 1$. There is a very small range of values near one that are appropriate for β. To see this, let $\sigma_{r_m}^2 \triangleq \mathbb{E}\left[|r_m|^2\right]$. Using similar definitions for $\sigma_{y_m}^2$ and $\sigma_{q_m}^2$, and the fact that r_m and q_m are uncorrelated, we obtain the following relationship between the powers of the input and output of the array:

$$\sigma_{y_m}^2 = \frac{\pi}{2}\beta^2\sigma_{r_m}^2, \qquad \sigma_{q_m}^2 = \sigma_{y_m}^2 - \sigma_{r_m}^2. \tag{4.18}$$

From (4.18), we can see that in order to prevent the quantization noise power from becoming greater than the input power $\sigma_{r_m}^2$, we must ensure that $\left(\frac{\pi}{2}\beta^2 - 1\right) < 1$, and hence that $1 \leq \beta < 2/\sqrt{\pi} \approx 1.1284$. Otherwise, the input power to each ADC grows monotonically with the antenna index.

The modeling described above does not rely on the assumption that $\mathbf{r}$ and $\mathbf{q}$ are uncorrelated,

just that r_m and q_m are uncorrelated. The cross-correlation matrix, $\mathbf{C}_{rq}$ is obtained by first assuming that $\mathbb{E}[q_m q_{m\pm 1}] \approx 0$ (this will be explained in Chapter 5). Then, using $\mathbb{E}[\mathbf{x}\mathbf{q}^H] \approx \mathbf{0}$ (see Appendix C for proof), (4.5) and (4.11), it is straightforward to show that

$$\mathbf{C}_{rq} = \mathbb{E}[\mathbf{r}\mathbf{q}^H] = -\mathbf{V}_d \mathbf{U}_d^{-1} \mathbf{C}_q, \tag{4.19}$$

where $\mathbf{C}_q = \mathrm{diag}(\sigma_{q_1}^2, \ldots, \sigma_{q_M}^2)$ and $\mathbf{V}_d \mathbf{U}_d^{-1}$ has the special structure

$$\mathbf{V}_d \mathbf{U}_d^{-1} = \mathbf{I}_N \otimes e^{-j\psi} \begin{bmatrix} 0 & 0 & \ldots & 0 & 0 \\ 1 & 0 & \ldots & 0 & 0 \\ 0 & 1 & \ldots & 0 & 0 \\ & & \vdots & & \\ 0 & 0 & \ldots & 1 & 0 \end{bmatrix}. \tag{4.20}$$

The analytical values of this cross-correlation is plotted in Fig. 4.8 for the 40th row of $\mathbf{C}_{rq}$. The simulated and analytical values of the cross-correlation are closely matched, indicating that the element-wise Bussgang decomposition describes the $\Sigma\Delta$ operation better than the vector-wise decomposition.

Two-bit Spatial $\Sigma\Delta$ ADCs

In this section, we extend the above analysis to the case where the quantizers in the $\Sigma\Delta$ array employ two-bits of resolution, implying four quantization levels. Unlike the one-bit case, with two bits the Gaussian approximation for r_m is quite accurate. We use the well-known Lloyd-max condition to determine the optimum quantization levels that minimize the distortion [118, 119]. We will denote the quantization levels and the associated intervals that minimize the distortion for unit variance Gaussian inputs by ν_i and $\left(\nu_i^{\mathrm{lo}}, \nu_i^{\mathrm{hi}}\right)$, $i = 1, \ldots, 4$,
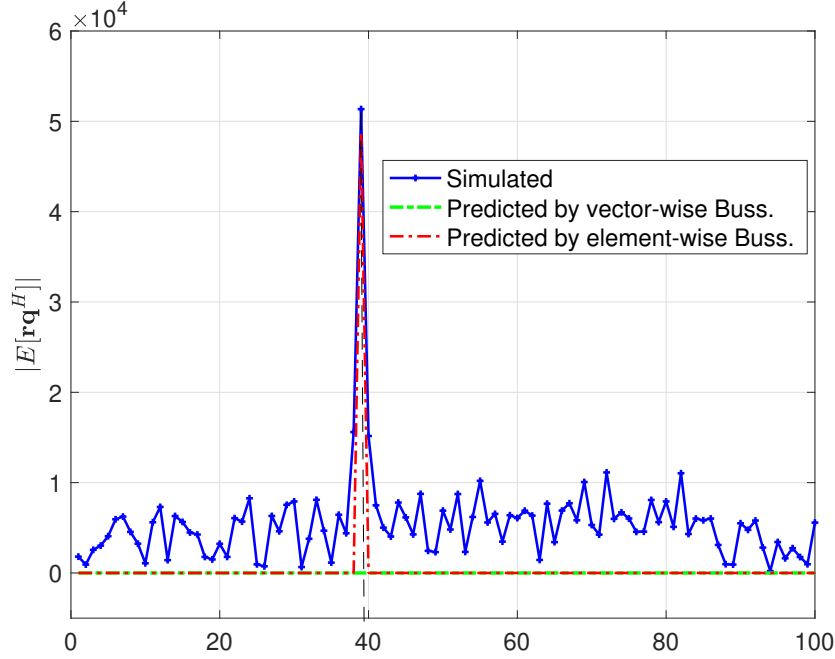
Figure 4.8: Cross-correlation between $\mathbf{r}$ and $\mathbf{q}$ with element-wise Bussgang decomposition for 1-bit ADCs.

respectively, and define

$$
\mathcal{Q}_m \left(r_m^{\mathrm{Re}} \right) = \nu_i, \quad \text{if } r_m^{\mathrm{Re}} \in \left(\frac{\sigma_{r_m}}{\sqrt{2}} \nu_i^{\mathrm{lo}}, \frac{\sigma_{r_m}}{\sqrt{2}} \nu_i^{\mathrm{hi}} \right], \tag{4.21}
$$

where $r_m^{\mathrm{Re}} \triangleq \mathrm{Re}(r_m)$. The above quantization levels satisfy $\nu_i^{\mathrm{hi}} = \nu_{i+1}^{\mathrm{lo}}$, $\nu_1^{\mathrm{lo}} = -\infty$, and $\nu_4^{\mathrm{hi}} = \infty$, and the quantization bins have been adjusted to span the range of the input levels by modeling r_m as a circularly symmetric Gaussian random variable with variance $\sigma_{r_m}^2$. Note that, while the convention is to also scale the output quantization level according to standard deviation of the input, we perform this scaling with the factor α_m as was performed for the one-bit case using (4.12).

Assuming a linear model as before and using an element-wise Bussgang decomposition, (4.9)

71
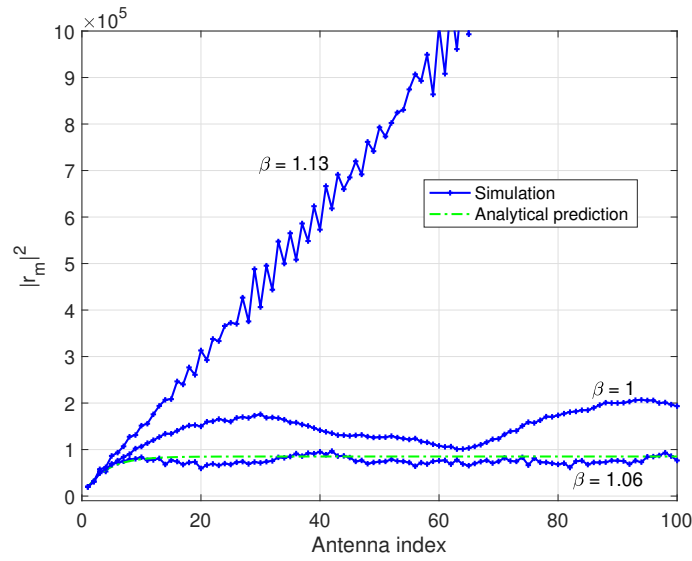
Figure 4.9: Input power to the *mth* ADC ($m = 40$) for different values of β- $\Sigma\Delta$ 1-bit.
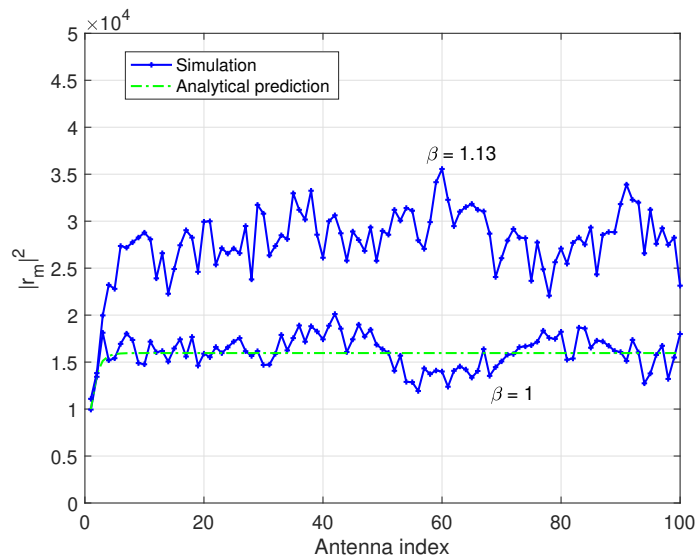
Figure 4.10: Input power to the *mth* ADC ($m = 40$) for different values of β- $\Sigma\Delta$ 2-bit.
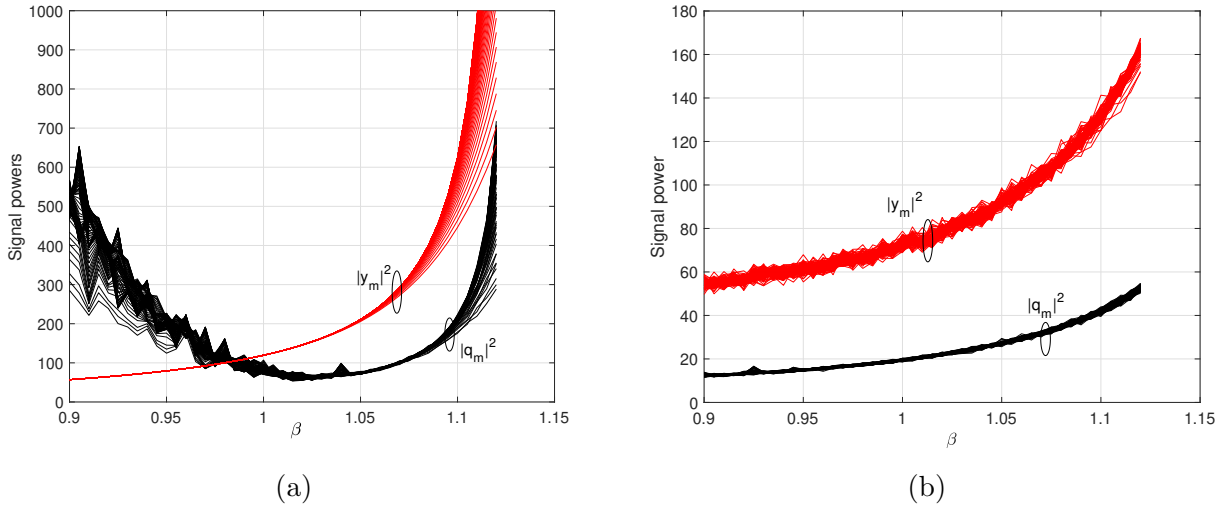
Figure 4.11: Output and quantization noise powers (a) 1-bit (b) 2-bits.

can be written as

$$\gamma_m = \frac{\mathbb{E}\left[r_m^{\mathrm{Re}} y_m^{\mathrm{Re}}\right]}{\mathbb{E}\left[r_m^{\mathrm{Re}}\right]^2} \tag{4.22}$$

due to the circular symmetry of the data, where $y_m^{\mathrm{Re}} \triangleq \mathrm{Re}\left(y_m\right)$. The numerator of (4.22) can be obtained from Bussgang's theorem [96]:

$$\mathbb{E}\left[r_m^{\mathrm{Re}} y_m^{\mathrm{Re}}\right] = \alpha_m \mathbb{E}\left[r_m^{\mathrm{Re}} \mathcal{Q}_{m'}\left(r_m^{\mathrm{Re}}\right)\right]$$
$$= \alpha_m \int_{-\infty}^{\infty} \frac{1}{\sqrt{2\pi}} \frac{\partial \mathcal{Q}_{m'}\left(r_m^{\mathrm{Re}}\right)}{\partial r_m^{\mathrm{Re}}} \exp\left(-\frac{\left(r_m^{\mathrm{Re}}\right)^2}{\sigma_{r_m}^2}\right) \mathrm{d}r_m^{\mathrm{Re}}. \tag{4.23}$$

The derivative $\partial \mathcal{Q}_{m'}\left(r_m^{\mathrm{Re}}\right)/\partial r_m^{\mathrm{Re}}$ can be computed as

$$\frac{\partial \mathcal{Q}_m\left(r_m^{\mathrm{Re}}\right)}{\partial r_m^{\mathrm{Re}}} = \sum_{i=2}^{4} \left(\nu_i - \nu_{i-1}\right) \delta\left(r_m^{\mathrm{Re}} - \frac{\sigma_{r_m}}{\sqrt{2}} \nu_i^{\mathrm{lo}}\right), \tag{4.24}$$

using the Dirac delta function $\delta(\cdot)$ to represent the derivative at the quantizer steps. Sub-

73

stituting the above equation in (4.23) and evaluating the integral, we get

$$\mathbb{E}\left[r_m^{\text{Re}} y_m^{\text{Re}}\right] = \alpha_m \sum_{i=2}^{4} \frac{(\nu_i - \nu_{i-1})}{\sqrt{2\pi}} \exp\left(-\frac{\left(\nu_i^{\text{lo}}\right)^2}{2}\right). \tag{4.25}$$

Then, the value of α_m that yields $\gamma_m = 1$ is given by

$$\alpha_{m'} = \frac{\beta \sigma_{r_m} \sqrt{\pi/2}}{\sum_{i=2}^{4} (\nu_i - \nu_{i-1}) \exp\left(-\frac{\left(\nu_i^{\text{lo}}\right)^2}{2}\right)}. \tag{4.26}$$

Thus, α_m is determined by the standard deviation of the ADC input, the quantization intervals and the corresponding output levels. Finally, computing the expectation $\mathbb{E}\left[|y_m|^2\right]$, the output and quantization noise powers are, respectively, given by

$$\begin{aligned}
\sigma_{y_m}^2 &= \alpha_m^2 \sum_i \left|\mathcal{Q}_m\left(r_m^{\text{Re}}\right)\right|^2 \Pr\left(\frac{\sigma_{r_m}}{\sqrt{2}}\nu_i^{\text{lo}} < r_m^{\text{Re}} \leq \frac{\sigma_{r_m}}{\sqrt{2}}\nu_i^{\text{hi}}\right) \\
&= 2\alpha_m^2 \sum_{i=1}^{4} \nu_i^2 \left(\Psi\left(\frac{\sigma_{r_m}}{\sqrt{2}}\nu_i^{\text{hi}}\right) - \Psi\left(\frac{\sigma_{r_m}}{\sqrt{2}}\nu_i^{\text{lo}}\right)\right), \\
\sigma_{q_m}^2 &= \sigma_{y_m}^2 - \sigma_{r_m}^2.
\end{aligned} \tag{4.27}$$

The effect of β on the input power to the ADC for the $m = 40$th antenna index is illustrated in Fig. 4.9 and Fig. 4.10 for one-bit and two-bits, respectively. The input power in the one-bit ADC case is stable as the antenna index is varied for $\beta = 1$ and 1.06, but increases rapidly when β is as high as 1.13. The $\Sigma\Delta$ two-bit case, however, is less sensitive to the particular choice of β. Similar observations can be made from Fig. 4.11 where the quantization noise powers and output powers are plotted as a function of β.

Finally, Fig. 4.12 shows that quantization noise power in dB as a function of the angle when there is a single user present at 25° and ψ is chosen to steer the ADC array to 25°, and when the inter-element antenna spacing is $\lambda/6$. The $\Sigma\Delta$ array, whether it is equipped with one or two-bit ADCs, has a superior noise shaping effect compared to regular ADCs. The
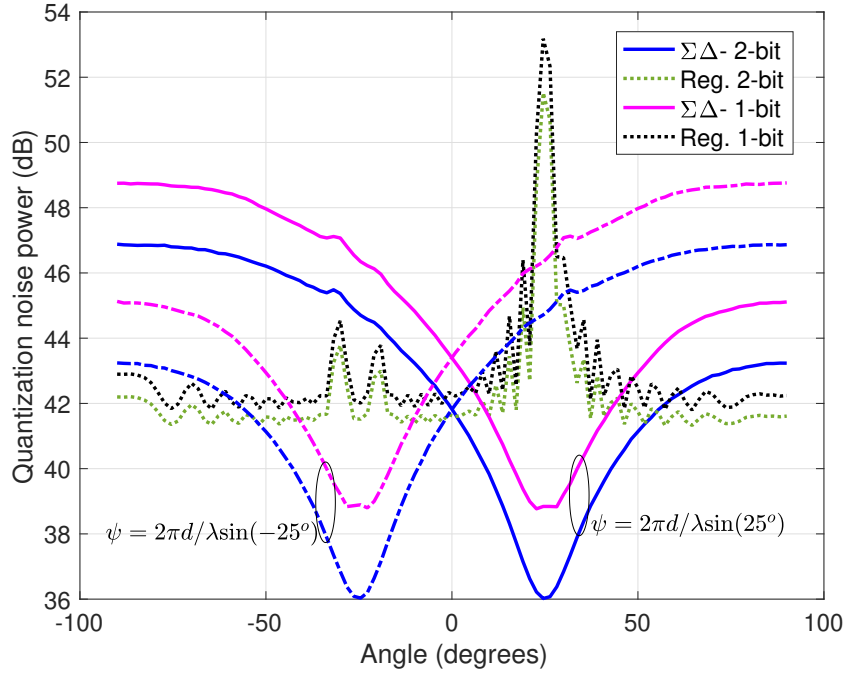
Figure 4.12: Quantization noise power as a function of the angle, $d/\lambda = 1/6$.

quantization noise power is significantly lower in the narrow sector around $25°$ but a higher quantization noise than regular ADCs outside of this sector. A similar noise shaping effect is also achieved when the signal of interest has a DOA $-25°$. When the spacing is $\lambda/2$, the width of the sector in which $\Sigma\Delta$ ADCs have a higher SQNR than standard quantizers is narrower. Fig. 4.14 shows the SQNR as a function of the angle when the user signal is originating from $-25°$ and ψ is chosen to steer the array to this angle. $\Sigma\Delta$ ADCs have a higher SQNR in the narrow sector around $-25°$ but a lower SQNR in the region outside of the steered sector.

4.3 Mutual Coupling

While spatial oversampling, i.e., antennas spaced less than one-half wavelength apart, can produce the required low spatial frequencies, there is a limit to how close the antennas can
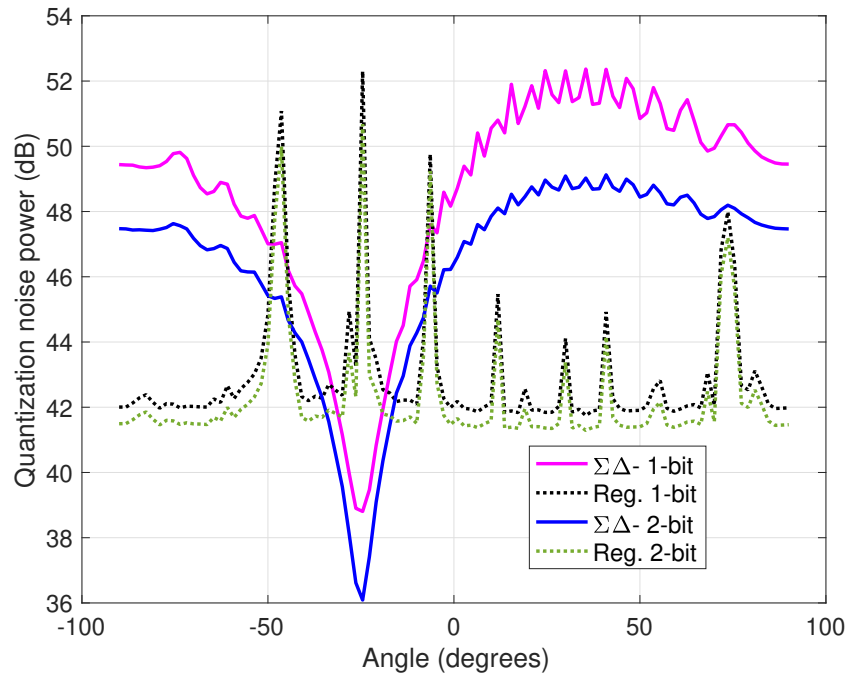
Figure 4.13: Quantization noise power as a function of the angle, $d/\lambda = 1/2$.
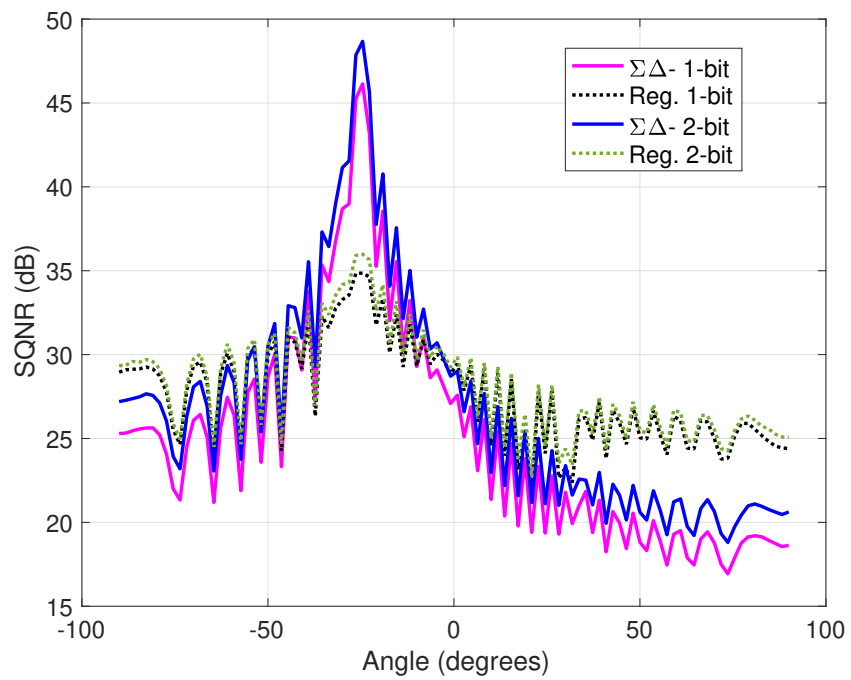
Figure 4.14: SQNR as a function of the angle.

be placed together before *mutual coupling* and the physical size of the antennas come into play. Mutual coupling is a phenomenon in which the electrical field of one antenna influences the current distribution of other antennas in close proximity. The effect of mutual coupling becomes prominent as the inter-element spacing is decreased below one-half wavelength, and can degrade the capacity [135]. The impact of mutual coupling is important because spatial $\Sigma\Delta$ arrays whose elements may be spaced closer than one-half wavelength apart are considered. In modeling the mutual coupling, the antenna array is treated as a bilateral network and the relationship between element output voltages and open circuit voltages is derived from multiport circuit theory. The analytical formulas involved in the expression for the so-called mutual coupling matrix (MCM), denoted by $\mathbf{T}$, are detailed in [113, 136, 137] and summarized below. The MCM $\mathbf{T}$ is given by

$$\mathbf{T} = \left(\mathbf{I} + \frac{1}{R}\mathbf{Z} \right)^{-1}, \tag{4.28}$$

where R is the input impedance of the low-noise amplifier (LNA). The impedance matrix of the antenna elements, $\mathbf{Z}$, is described by

$$\begin{aligned}
\mathbf{Z}_{ij} &= 30 \left(2\mathrm{Ci}(2\pi d_{ij}) - \mathrm{Ci}(\xi_{ij} + \pi) - \mathrm{Ci}(\xi_{ij} - \pi) \right. \\
&\quad \left. -j \left(2\mathrm{Si}(2\pi d_{ij}) - \mathrm{Si}(\xi_{ij} + \pi) - \mathrm{Si}(\xi_{ij} - \pi) \right) \right), i \neq j \\
\mathbf{Z}_{ii} &= 30 \left(\eta + \log(2\pi) - \mathrm{Ci}(2\pi) + j\mathrm{Si}(2\pi) \right),
\end{aligned} \tag{4.29}$$

for $i, j = 1, \cdots, M$, where $\xi_{ij} = \pi\sqrt{1 + 4d_{ij}^2}$.

Furthermore, due to the presence of mutual coupling, the noise at the receiver is spatially

correlated and its covariance matrix is given by

$$\mathbf{C}_N = \mathbf{T}\mathbf{\Upsilon}\mathbf{T}^H, \tag{4.30}$$

$$\mathbf{\Upsilon} = \sigma_i^2 \left(\mathbf{Z}\mathbf{Z}^H - 2R_N \mathrm{Re}(\varrho_n^* \mathbf{Z}) + R_N^2 \mathbf{I} \right) + 4k_B T_A B \mathrm{Re}(\mathbf{Z}) , \tag{4.31}$$

where $\sigma_i^2 = \mathbb{E}[\mathbf{i}_N \mathbf{i}_N^H]$, $\sigma_v^2 = \mathbb{E}[\mathbf{v}_N \mathbf{v}_N^H]$, $\mathbf{i}_N$ and $\mathbf{v}_N$ are the complex current and voltage of the noise source, $R_N = \sigma_v/\sigma_i$ is the noise resistance, $\varrho_n = \mathbb{E}[\mathbf{i}_N \mathbf{v}_N^H]/(\sigma_i \sigma_v)$ is the so-called noise correlation coefficient, k_B is the Boltzmann constant, T_A is the ambient temperature, and B is the bandwidth. In Chapters 5 and 6, the channel model will incorporate the effect of mutual coupling whenever oversampled arrays are considered.

Chapter 5

Channel Estimation Using Low-Resolution Spatial Sigma-Delta ADCs

In this chapter, the element-wise Bussgang decomposition will be used for linear minimum mean squared error (LMMSE) channel estimation for massive MIMO systems where the BS is equipped with low resolution (1-2 bits) spatial $\Sigma\Delta$ ADCs. A recursive solution to compute the covariance matrices required for the LMMSE channel estimate is found and a practical algorithm is found for doing so. The resulting estimators have low complexity and analytical expressions for the resulting covariance matrix of the channel estimation error are derived. A lower bound on the uplink achievable rate using the maximal ratio combining (MRC), zero-forcing (ZF) and LMMSE receivers when implemented with imperfect channel state information (CSI) obtained using the LMMSE channel estimate, assuming the detailed model for mutual coupling outlined in Chapter 4.

5.1 System Model

An uplink massive MIMO system with K single-antenna user terminals, and a base station (BS) equipped with a uniform linear array (ULA) of M antennas and a first-order spatial $\Sigma\Delta$ array is considered. During the training period, all K users simultaneously transmit their pilot sequences of length N. The received signal, $\mathbf{X} \in \mathbb{C}^{M \times N}$, at the BS is

$$\mathbf{X} = [\mathbf{x}_1 \ \cdots \ \mathbf{x}_N] = \sqrt{\rho}\,\mathbf{G}\,\boldsymbol{\Phi}_t + \mathbf{N}, \tag{5.1}$$

where $\mathbf{x}_k$ is the array output for training sample k, $\mathbf{G} \in \mathbb{C}^{M \times K}$ is the channel matrix, and $\boldsymbol{\Phi}_t \in \mathbb{C}^{K \times N}$ is the pilot matrix. The matrix $\mathbf{N} = [\mathbf{n}_1, \mathbf{n}_2, \ldots, \mathbf{n}_N]$ contains noise from both intrinsic (low-noise amplifiers and other circuitry) and extrinsic (received by the antennas) sources and consists of zero mean spatially correlated additive noise Gaussian elements that satisfy

$$\mathbb{E}\left[\mathbf{n}_i\mathbf{n}_i^H\right] = \mathbf{C}_N,$$
$$\mathbb{E}\left[\mathbf{n}_i\mathbf{n}_j^H\right] = \mathbf{0}, \quad i \neq j, \tag{5.2}$$

where $\mathbf{C}_N$ is the spatial correlation matrix of the receiver noise as described in Chapter 4. It is assumed that power control is employed to counteract non-uniform path loss so that all the user signals are received with the same power; thus the factor ρ determines the SNR. A spatially correlated channel model for $\mathbf{G}$ is assumed. In particular, the kth column of $\mathbf{G}$, which represents the channel $\mathbf{g}_k$ for the kth user, is assumed to be given by

$$\mathbf{g}_k = \mathbf{C}_{g_k}^{\frac{1}{2}}\mathbf{h}_k\ , \tag{5.3}$$

where the elements of $\mathbf{h}_k \in \mathbb{C}^{L_k \times 1}$ are independently and identically distributed (i.i.d.) as $\mathcal{CN}(0,1)$ random variables, and $\mathbf{C}_{g_k} \in \mathbb{C}^{M \times L_k}$ is the channel covariance matrix. In this application, the spatial correlation will arise from two factors: signal arrivals that come from a certain sector of possible angles of arrival (AoAs), and mutual coupling between the BS antennas:

$$\mathbf{C}_{g_k}^{\frac{1}{2}} = \frac{1}{\sqrt{L_k}} \mathbf{T} \mathbf{A}_k \ , \tag{5.4}$$

where $\mathbf{T}$ is the $M \times M$ matrix that accounts for the mutual coupling as described in Chapter 4, $\mathbf{A}_k \in \mathbb{C}^{M \times L_k}$ is a matrix whose lth column is the steering vector of a linear array

$$\mathbf{a}_l = \begin{bmatrix} 1 & e^{-j2\pi d_{12}\sin(\theta_l)} & \cdots & e^{-j2\pi d_{1M}\sin(\theta_l)} \end{bmatrix}^T \ , \tag{5.5}$$

θ_l is the AoA, and d_{ij} is the distance between the antenna elements i and j. It will be assumed that the AoAs for all users lie in a certain known angular region $\theta_l \in \mathcal{S}_\theta$. Here, L_k represents the number of propagation paths over which user k's signal is received. The restriction $\theta_l \in \mathcal{S}_\theta$ is a common situation in many practical settings due to cell sectoring; *e.g.,* a given BS array will only serve users from some fraction of all available azimuth or elevation angles. Besides this region $\mathcal{S}_\theta$, prior to channel estimation the BS is only aware of the channel covariance matrix $\mathbf{C}_{g_k}$ for each user, and not the components (mutual coupling, AoAs) of its decomposition in (5.4).

Vectorizing (5.1), we get

$$\mathbf{x} = \text{vec}\,(\mathbf{X}) = \mathbf{\Phi}\mathbf{g} + \mathbf{n}, \tag{5.6}$$

where

$$\boldsymbol{\Phi} = \sqrt{\rho}\left(\boldsymbol{\Phi}_t^T \otimes \mathbf{I}_M\right)$$

$$\mathbf{g} = \begin{bmatrix} \mathbf{g}_1 \\ \mathbf{g}_2 \\ \vdots \\ \mathbf{g}_K \end{bmatrix} = \text{vec}\left(\mathbf{G}\right), \qquad \mathbf{n} = \begin{bmatrix} \mathbf{n}_1 \\ \mathbf{n}_2 \\ \vdots \\ \mathbf{n}_N \end{bmatrix} = \text{vec}\left(\mathbf{N}\right). \tag{5.7}$$

The covariance matrix of $\mathbf{x}$ can be expressed as

$$\mathbf{C}_x = \boldsymbol{\Phi}\mathbf{C}_g\boldsymbol{\Phi}^H + \mathbf{C}_n, \tag{5.8}$$

where the block-diagonal matrices $\mathbf{C}_g = \text{blkdiag}\{\mathbf{C}_{g_1}, \ldots, \mathbf{C}_{g_K}\}$ and $\mathbf{C}_n = \mathbf{I}_N \otimes \mathbf{C}_N$ have been defined. The average per-user per-antenna SNR is defined as

$$\text{SNR} = \frac{\rho}{NK}\frac{\text{Tr}\left(\mathbb{E}\left[\mathbf{G}\boldsymbol{\Phi}_t\boldsymbol{\Phi}_t^H\mathbf{G}^H\right]\right)}{\text{Tr}\left(\mathbf{C}_N\right)}. \tag{5.9}$$

When the pilot sequences are row-wise orthogonal and the minimum number of pilots, $N = K$, is used, then $\boldsymbol{\Phi}_t\boldsymbol{\Phi}_t^H = K\mathbf{I}_K$ and

$$\text{SNR} = \frac{\rho}{K}\frac{\text{Tr}\left(\mathbf{C}_g\right)}{\text{Tr}\left(\mathbf{C}_N\right)}. \tag{5.10}$$

In the derivations below, it will be assumed that the power of the pilot signals is time-invariant, which implies that the diagonal elements of $\boldsymbol{\Phi}_t^H\boldsymbol{\Phi}_t$ are identical. The goal is to derive an algorithm to estimate the channel $\mathbf{g}$ from the output of the $\Sigma\Delta$ array. Defining $m' = \text{mod}_M(m)$, the output of the $\Sigma\Delta$ ADC array is defined similar to Ch. 4.2

$$y_m = \alpha_{m'}\mathcal{Q}_{m'}\left(\text{Re}(r_m)\right) + j\alpha_{m'}\mathcal{Q}_{m'}\left(\text{Im}(r_m)\right), \tag{5.11}$$

where $\mathcal{Q}_{m'}$ represents the quantization operation for antenna m', and $\alpha_{m'}$ is the output level of the quantizer. In vector form, the output of the $\Sigma\Delta$ array can be written as

$$\mathbf{y} = \mathcal{Q}(\mathbf{r}) \tag{5.12}$$
$$= [\mathcal{Q}_1(r_1), \ldots, \mathcal{Q}_M(r_M), \mathcal{Q}_1(r_{M+1}), \ldots, \mathcal{Q}_M(r_{MN})]^T ,$$

where

$$\mathbf{r} = \mathbf{U}\mathbf{x} - \mathbf{V}\mathbf{y}$$
$$\mathbf{V} = \mathbf{I}_N \otimes \mathbf{V}_d \tag{5.13}$$
$$\mathbf{U} = \mathbf{I}_N \otimes \mathbf{U}_d.$$

The matrices $\mathbf{V}_d$ and $\mathbf{U}_d$ were defined in Ch. 4.2. The element-wise Bussgang decomposition described in 4.2.2 has to be slightly modified for the $MN \times 1$ vectors $\mathbf{r}$ and $\mathbf{y}$ defined above. For the one-bit $\Sigma\Delta$ case,

$$\alpha_{m'}^* = \beta \frac{\sqrt{\pi \mathbb{E}[|r_m|^2]}}{2}, \tag{5.14}$$

with a value of $\beta > 1$. The reader is referred to Ch. 4.2.2 for a discussion on the necessity and on the method of selection of the correction factor β. For the two-bit case,

$$\alpha_{m'} = \frac{\sigma_{r_m}\sqrt{\pi/2}}{\sum_{i=2}^{4} (\nu_i - \nu_{i-1}) \exp\left(-\frac{(\nu_i^{\text{lo}})^2}{2}\right)}. \tag{5.15}$$

5.2 Channel Estimation with spatial Sigma-Delta ADCs

The LMMSE channel estimate is derived based on the one-bit or two-bit outputs $\mathbf{y}$ of the $\Sigma\Delta$ ADC array.

5.2.1 LMMSE Channel Estimation

The LMMSE channel estimate is defined by

$$
\begin{aligned}
\hat{\mathbf{g}} &= \mathbb{E}\left[\mathbf{g}\mathbf{y}^H\right]\left(\mathbb{E}\left[\mathbf{y}\mathbf{y}^H\right]\right)^{-1}\mathbf{y} \\
&= \mathbf{C}_{gy}\mathbf{C}_y^{-1}\mathbf{y} \ .
\end{aligned}
\tag{5.16}
$$

Using the equivalent linear model in (4.11), we can obtain the covariance matrix of $\mathbf{y}$:

$$
\mathbf{C}_y = \mathbf{C}_x + \mathbf{U}^{-1}\mathbf{C}_q\mathbf{U}^{-H},
\tag{5.17}
$$

where $\mathbf{C}_q$ is the covariance matrix of $\mathbf{q}$. The expression in (5.17) relies on the assumption that $\mathbb{E}\left[\mathbf{x}\mathbf{q}^H\right] = \mathbf{0}$, which is shown in Appendix C to be true if r_m is Gaussian. This does not imply that $\mathbb{E}\left[\mathbf{r}\mathbf{q}^H\right] = \mathbf{0}$, as $\mathbf{r}$ and $\mathbf{q}$ are clearly correlated. Although r_m is strictly speaking not Gaussian, the assumption is sufficiently accurate here, and it will be seen in Section 5.4 that it yields a channel estimator with good performance. Similarly, since $\mathbf{\Gamma} = \mathbf{I}$ has been chosen in (4.5), it is easy to show that

$$
\mathbf{r} = \mathbf{x} - \mathbf{V}\mathbf{U}^{-1}\mathbf{q}
\tag{5.18}
$$

and hence that

$$
\mathbf{C}_r = \mathbf{C}_x + \mathbf{V}\mathbf{U}^{-1}\mathbf{C}_q\mathbf{U}^{-H}\mathbf{V}^H.
\tag{5.19}
$$

From (5.17), it is seen that $\mathbf{C}_y$ is determined by $\mathbf{C}_q$, whereas (4.18) and (4.27) show that the quantization noise power is dependent on $\sigma_{y_m}^2$. Due to this inter-relationship between $\mathbf{C}_y$ and $\mathbf{C}_q$, these matrices cannot be computed in closed form. However, they can be computed in a recursive manner.

Using $\mathbb{E}\left[\mathbf{x}\mathbf{q}^H\right] \approx \mathbf{0}$ and the fact that $\mathbb{E}\left[r_m q_m^*\right] = 0$, it can be shown that $\mathbb{E}\left[q_m q_{m\pm 1}^*\right] \approx 0$. As a result, $\mathbf{C}_q$ is approximately diagonal with elements given by $\sigma_{q_m}^2$. Furthermore, noting that $\mathbf{V}\mathbf{U}^{-1}$ has the structure

$$
\mathbf{V}\mathbf{U}^{-1} = \mathbf{I}_N \otimes e^{-j\psi}
\begin{bmatrix}
0 & 0 & \ldots & 0 & 0 \\
1 & 0 & \ldots & 0 & 0 \\
0 & 1 & \ldots & 0 & 0 \\
 & & \vdots & & \\
0 & 0 & \ldots & 1 & 0
\end{bmatrix},
\tag{5.20}
$$

the following recursion for $\sigma_{r_m}^2$, $\sigma_{y_m}^2$ and $\sigma_{q_m}^2$ using (5.17) and (5.19) can be generated:

$$
\sigma_{r_m}^2 =
\begin{cases}
\sigma_{x_m}^2, & m = kM + 1, \quad k = 0, 1, \ldots, N - 1, \\
\\
\sigma_{x_m}^2 + \sigma_{q_{m-1}}^2, & \text{otherwise.}
\end{cases}
$$

$$
\sigma_{y_m}^2 =
\begin{cases}
\frac{\pi}{2}\beta^2 \sigma_{r_m}^2, & \text{for 1-bit ADCs} \\
\\
\frac{\alpha^2 \sigma_{r_m}^2}{2} \sum_{i=1}^{4} \nu_i^2 \left(\Psi\left(\frac{\sigma_{r_m}}{\sqrt{2}}\nu_i^{\text{hi}}\right) - \Psi\left(\frac{\sigma_{r_m}}{\sqrt{2}}\nu_i^{\text{lo}}\right) \right), \\
\quad\quad \text{for 2-bit ADCs}
\end{cases}
\tag{5.21}
$$

$$
\sigma_{q_m}^2 = \sigma_{y_m}^2 - \sigma_{r_m}^2.
$$

In the above equations, $\sigma_{x_m}^2$ is the mth diagonal element of $\mathbf{C}_x$. Thus, the power of the mth quantizer input, $\sigma_{r_m}^2$, depends on the quantization noise powers computed up to index $m - 1$. Then, the mth output power, $\sigma_{y_m}^2$, is given by (4.18) for one-bit ADCs and by (4.27) for two-bit ADCs. This allows us to compute $\sigma_{q_m}^2$, and from there $\sigma_{r_{m+1}}^2$, and so on. Following

85

this process for indices $m = 1$ to MN allows us to compute $\mathbf{C}_q$, and finally the complete $\mathbf{C}_y$ is obtained from (5.17).

Thus, the LMMSE estimate of the channel, $\hat{\mathbf{g}}$, can be obtained from (5.16) where

$$
\begin{aligned}
\mathbf{C}_{gy} &= \mathbb{E}\left[\mathbf{g}\mathbf{y}^H\right] \\
&= \mathbb{E}\left[\mathbf{g}\left(\mathbf{\Phi}\mathbf{g} + \mathbf{n} + \mathbf{U}^{-1}\mathbf{q}\right)^H\right] \\
&= \mathbf{C}_g\mathbf{\Phi}^H + \mathbb{E}\left[\mathbf{g}\mathbf{q}^H\right]\mathbf{U}^{-H} \\
&\approx \mathbf{C}_g\mathbf{\Phi}^H .
\end{aligned}
\tag{5.22}
$$

The final approximation results because $\mathbb{E}\left[\mathbf{g}\mathbf{q}^H\right] = \mathbf{\Phi}^\dagger\mathbb{E}\left[\mathbf{x}\mathbf{q}^H\right] - \mathbf{\Phi}^\dagger\mathbb{E}\left[\mathbf{n}\mathbf{q}^H\right] \approx \mathbf{0}$, since $\mathbb{E}\left[\mathbf{x}\mathbf{q}^H\right] \approx \mathbf{0}$ and it can be shown that $\mathbb{E}\left[\mathbf{n}\mathbf{q}^H\right] = \mathbf{0}$ using an argument identical to that in Appendix C for Gaussian noise $\mathbf{n}$. The resulting algorithm for computing the LMMSE channel estimate for the $\Sigma\Delta$ array has low complexity and is summarized in Algorithm 1.

Algorithm 1: Channel estimation using $\Sigma\Delta$ array

---

1. Set $\beta = 1.05$ for one-bit operation. For $m = 1$ to MN, repeat:

(i) Update the diagonal elements of $\mathbf{C}_r$, $\sigma_{r_m}^2$, using (5.21). Update $\sigma_{y_m}^2$ using (4.18) for one-bit ADCs and (4.27) for two-bit ADCs.

(ii) The elements of $\mathbf{C}_q$, $\sigma_{q_m}^2$, are updated using $\sigma_{q_m}^2 = \sigma_{y_m}^2 - \sigma_{r_m}^2$.

(iii) Update $\alpha_{m'} = \begin{cases} \text{From (5.14) for one-bit } \Sigma\Delta \text{ ADCs,} \\ \text{From (5.15) for two-bit } \Sigma\Delta \text{ ADCs.} \end{cases}$.

2. Obtain the complete matrix $\mathbf{C}_y$ using (5.17).

3. Compute the output of the $\Sigma\Delta$ array as follows:

(i) $r_m = x_m$, for $m = kM + 1, k = 0, \ldots, N - 1$.
   $r_m = x_m + e^{-j\psi}(r_{m-1} - y_{m-1})$, otherwise.

(ii) $y_m = \alpha_{m'}(\mathcal{Q}_m(\text{Re}(r_m)) + j\mathcal{Q}_m(\text{Im}(r_m)))$.

4. Estimate the channel, $\hat{\mathbf{g}}$, from (5.16).

5.2.2 Channel Estimation Error

As the $\Sigma\Delta$ channel estimation error will be compared with standard one-bit sampling, which is unable to identify the channel gain, normalized error (or cosine distance) that is independent of any scaling factor affecting either the real channel or its estimate will be used:

$$
\begin{aligned}
\mathrm{NE} &= \min_{\zeta} \frac{\mathbb{E}\left[\|\mathbf{g} - \zeta\hat{\mathbf{g}}\|_2^2\right]}{\mathbb{E}\left[\|\mathbf{g}\|_2^2\right]} \\
&= 1 - \frac{\mathbb{E}\left[|\hat{\mathbf{g}}^H\mathbf{g}|^2\right]}{\mathbb{E}\left[\|\hat{\mathbf{g}}\|_2^2\right]\mathbb{E}\left[\|\mathbf{g}\|_2^2\right]}.
\end{aligned}
\tag{5.23}
$$

This expression for the NE, which satisfies $0 \leq \mathrm{NE} \leq 1$, is valid for any estimator. For the particular case of LMMSE estimators, which necessarily satisfy $\mathbb{E}\left[\mathbf{g}\hat{\mathbf{g}}^H\right] = \mathbf{C}_{\hat{g}}$, (5.23) can be expressed as

$$
\mathrm{NE} = \frac{\mathbb{E}\left[\|\mathbf{g}\|_2^2\right] - \mathbb{E}\left[\|\hat{\mathbf{g}}\|_2^2\right]}{\mathbb{E}\left[\|\mathbf{g}\|_2^2\right]} = \frac{\mathrm{Tr}\left(\mathbf{C}_{\mathbf{g}} - \mathbf{C}_{\hat{\mathbf{g}}}\right)}{\mathrm{Tr}\left(\mathbf{C}_g\right)},
\tag{5.24}
$$

where $\mathbf{C}_{\hat{g}}$ is given by

$$
\begin{aligned}
\mathbf{C}_{\hat{g}} &= \mathbb{E}\left[\hat{\mathbf{g}}\hat{\mathbf{g}}^H\right] = \mathbf{C}_g\mathbf{\Phi}^H\mathbf{C}_y^{-1}\mathbf{\Phi}\mathbf{C}_g \\
&= \mathbf{C}_g\mathbf{\Phi}\left(\mathbf{C}_x + \mathbf{U}^{-1}\mathbf{C}_q\mathbf{U}^{-H}\right)^{-1}\mathbf{\Phi}^H\mathbf{C}_g.
\end{aligned}
\tag{5.25}
$$

Finally, the estimation error covariance matrix is given by

$$
\mathbf{C}_\epsilon = \mathbf{C}_g - \mathbf{C}_g\mathbf{\Phi}\left(\mathbf{C}_x + \mathbf{U}^{-1}\mathbf{C}_q\mathbf{U}^{-H}\right)^{-1}\mathbf{\Phi}^H\mathbf{C}_g.
\tag{5.26}
$$

When the pilots are orthogonal and $N = K$, the matrices $\mathbf{C}_x$, $\mathbf{C}_y$ and $\mathbf{C}_q$ are block-diagonal with identical blocks. As a result, $\mathbf{C}_{\hat{g}}$ is also block-diagonal and the kth $M \times M$ block corresponds to the covariance matrix of the estimated channel of the kth user.

Remark: It should be noted here that a candidate for comparison with the above estimator

is an LMMSE channel estimator based on the output of a massive MIMO system with conventional two-bit quantizers. Although, a channel estimator based on the Bussgang decomposition for one-bit ADCs has been derived in [27], no explicit analysis exists for two-bit ADCs. To facilitate such a comparison, in Appendix D the LMMSE channel estimator based on standard two-bit quantization of the array output is derived.

5.3   Uplink Achievable Rate Analysis

In this section, the uplink achievable rate for MRC and ZF receivers is derived. In the uplink data transmission stage, the K users transmit their data represented by the $K \times 1$ vector $\mathbf{s}$. Using a Bussgang decomposition as described previously on the $\Sigma\Delta$-quantized received signal, $\mathbf{y}_d$, we get

$$\mathbf{y}_d = \mathcal{Q}\left(\mathbf{r}_d\right) = \sqrt{\rho_d}\mathbf{G}\mathbf{s} + \mathbf{n}_d + \mathbf{U}_d^{-1}\mathbf{q}_d, \tag{5.27}$$

where $\mathbf{r}_d = \mathbf{U}_d\left(\sqrt{\rho_d}\mathbf{G}\mathbf{s} + \mathbf{n}_d\right) - \mathbf{V}_d\mathbf{y}_d$, ρ_d is the data transmission power, $\mathbf{n}_d \sim \mathcal{CN}\left(\mathbf{0}, \mathbf{C}_N\right)$ and $\mathbf{q}_d$ are the additive and quantization noise in the data phase, respectively. The matrices $\mathbf{U}_d$ and $\mathbf{V}_d$ are defined by taking $N = 1$ in Eq. (5.13). For this analysis, it is assumed that the user symbols s_k are i.i.d with $\mathbb{E}\left[|s_k|^2\right] = 1$ and that the channel covariance matrices of the different users are equal and denoted by $\mathbf{C}_G = \mathbf{C}_{g_1} = \cdots = \mathbf{C}_{g_K}$.

The analysis of the achievable rate relies on the covariance matrix of $\mathbf{q}_d$, $\mathbf{C}_{q_d}$, which is different from the quantization noise covariance matrix during the training phase. For the data transmission stage, this matrix has to be derived in a manner similar to Section 5.2. Inspecting the recursion equations developed in the previous section, it is seen that initialization of the recursion will be performed with $\mathbf{C}_{x_d}$, where $\mathbf{C}_{x_d} = \rho_d\mathbf{G}\mathbf{G}^H + \mathbf{C}_N$. To simplify the subsequent analysis, as in [27, 39] we can approximate $\mathbf{G}\mathbf{G}^H$ by $K\mathbf{C}_G$, which becomes

increasingly accurate as K grows. It will be seen in the simulations that excellent agreement between the theoretical and simulated spectral efficiency is obtained even for values as low as $K = 10$. Thus

$$\mathbf{C}_{x_d} \approx K\rho_d\mathbf{C}_G + \mathbf{C}_N. \tag{5.28}$$

The procedure to obtain $\mathbf{C}_{q_d}$ is outlined as follows. Let $\sigma^2_{r_{d_m}}$, $\sigma^2_{y_{d_m}}$ and $\sigma^2_{q_{d_m}}$ denote the powers of the mth components of $\mathbf{r}_d$, $\mathbf{y}_d$ and $\mathbf{q}_d$, respectively. Then, (5.21) is modified for the data transmission stage as

$$\sigma^2_{r_{d_m}} = \begin{cases} \sigma^2_{x_{d_m}}, & m = 0, 1, \ldots, M, \\[2em] \sigma^2_{x_{d_m}} + \sigma^2_{q_{d_{m-1}}}, & \text{otherwise.} \end{cases}$$

$$\sigma^2_{y_{d_m}} = \begin{cases} \frac{\pi}{2}\beta^2\sigma^2_{r_{d_m}}, & \text{for 1-bit ADCs} \\[2em] \frac{\alpha^2\sigma^2_{r_{d_m}}}{2}\sum_{i=1}^{4}\nu_i^2\left(\Psi\left(\frac{\sigma_{r_{d_m}}}{\sqrt{2}}\nu_i^{\text{hi}}\right) - \Psi\left(\frac{\sigma_{r_{d_m}}}{\sqrt{2}}\nu_i^{\text{lo}}\right)\right), \\ \qquad\qquad \text{for 2-bit ADCs} \end{cases} \tag{5.29}$$

$$\sigma^2_{q_{d_m}} = \sigma^2_{y_{d_m}} - \sigma^2_{r_{d_m}},$$

where $\sigma^2_{x_{d_m}}$ is the mth diagonal element of $\mathbf{C}_{x_d}$. The diagonal matrix $\mathbf{C}_{q_d}$ is completed with $\sigma^2_{q_{d_m}}$ as its diagonal elements.

The BS uses a linear receiver for symbol detection that depends on the LMMSE channel estimate. Denoting the linear receiver by $\mathbf{W}$, the detected symbol vector is obtained by

multiplying the conjugate transpose of $\mathbf{W}$ with the received signal vector as

$$\hat{\mathbf{s}} = \mathbf{W}^H \mathbf{y}_d = \sqrt{\rho_d} \mathbf{W}^H \mathbf{G} \mathbf{s} + \mathbf{W}^H \mathbf{n}_d + \mathbf{W}^H \mathbf{U}_d^{-1} \mathbf{q}_d. \tag{5.30}$$

From (5.30), the various components contributing to the kth detected symbol can be re-written as

$$\hat{s}_k = \sqrt{\rho_d} \mathbb{E} \left[\mathbf{w}_k^H \mathbf{g}_k \right] s_k + \sqrt{\rho_d} \left(\mathbf{w}_k^H \mathbf{g}_k - \mathbb{E} \left[\mathbf{w}_k^H \mathbf{g}_k \right] \right) s_k +$$
$$\sqrt{\rho_d} \mathbf{w}_k^H \sum_{i \neq k} \mathbf{g}_i s_i + \mathbf{w}_k^H \mathbf{n}_d + \mathbf{w}_k^H \mathbf{U}_d^{-1} \mathbf{q}_d, \tag{5.31}$$

where $\mathbf{w}_k$ is the kth column of $\mathbf{W}$. The terms in the above equation correspond to the desired signal, the receiver uncertainty, the inter-user interference, the additive noise and the quantization noise, respectively.

An approach similar to [39] and [138] will be followed and the classical worst-case uncorrelated Gaussian assumption on the terms in (5.31) will be used to obtain a lower bound on the achievable rate. Treating the final four terms as "effective noise", the achievable rate of the kth user is given by (5.33) at the top of the next page, based on the widely used approximation for massive MIMO systems [138]

$$\mathbb{E} \left[\log_2 \left(1 + \frac{X}{Y} \right) \right] \approx \log_2 \left(1 + \frac{\mathbb{E}[X]}{\mathbb{E}[Y]} \right), \tag{5.32}$$

where X and Y are sums of non-negative random variables. The above approximation becomes increasingly accurate for a large number of antennas since, according to the law of large numbers, the variances of both X and Y become small due to channel hardening effect. Whereas the achievable rate bounds derived in [103] assume perfect knowledge of the CSI, our result takes into account the channel estimation error. In the derivation of the worst-case bound, it is assumed that the channel estimate $\hat{\mathbf{g}}$ is Gaussian with covariance matrix $\mathbf{C}_{\hat{g}}$ given by (5.25). Similarly, $\mathbf{q}_d$ is also assumed to be Gaussian and its covariance

matrix is obtained as described earlier in this section. In the following, the performance for the specific cases of the MRC, ZF and LMMSE receivers is considered. In the derivation of the achievable rate using these receivers, it will be assumed that during the training phase, the pilots are orthogonal and that $N = K$. Consequently, the matrices $\mathbf{C}_x$, $\mathbf{C}_y$ and $\mathbf{C}_{\hat{g}}$ will be block-diagonal.

$$R_k = \log_2 \left(1 + \frac{\rho_d \left| \mathbb{E}\left[\mathbf{w}_k^H \mathbf{g}_k\right] \right|^2}{\rho_d \mathrm{var}\left(\mathbf{w}_k^H \mathbf{g}_k\right) + \rho_d \sum_{i \neq k} \mathbb{E}\left[|\mathbf{w}_k^H \mathbf{g}_i|^2\right] + \mathbb{E}\left[\left|\mathbf{w}_k^H \mathbf{n}_d\right|^2\right] + \mathbb{E}\left[\left|\mathbf{w}_k^H \mathbf{U}_d^{-1} \mathbf{q}_d\right|^2\right]} \right)$$

$$(5.33)$$

5.3.1 MRC receiver

To simplify the analysis, an MRC receiver without pre-whitening is considered, as follows:

$$\mathbf{W}_{\mathrm{MRC}} = \hat{\mathbf{G}}, \tag{5.34}$$

where $\hat{\mathbf{G}}$ is the $M \times K$ matrix formed from $\hat{\mathbf{g}}$ using the inverse of the vec operation. The achievable rate of the kth user is given by (5.35). To show this, the individual terms in the

$$R_k^{\mathrm{MRC}} = \log_2 \left(1 + \frac{\rho_d \mathrm{Tr}\left(\mathbf{C}_{\hat{g}}\right)/K}{\rho_d K \mathrm{Tr}\left(\mathbf{C}_G\right) + \mathrm{Tr}\left(\mathbf{C}_N\right) + \mathrm{Tr}\left(\mathbf{U}_d^{-1} \mathbf{C}_{q_d} \mathbf{U}_d^{-H}\right)} \right) \tag{5.35}$$

achievable rate expression of (5.33) are computed below.

$$
\begin{aligned}
\mathbb{E}\left[\hat{\mathbf{g}}_k^H \mathbf{g}_k\right] &= \mathbb{E}\left[\hat{\mathbf{g}}_k^H \left(\hat{\mathbf{g}}_k + \boldsymbol{\epsilon}_k\right)\right] \\
&= \mathbb{E}\left[\|\hat{\mathbf{g}}_k\|^2\right] + \mathbb{E}\left[\hat{\mathbf{g}}_k^H \boldsymbol{\epsilon}_k\right] \\
&= \mathbb{E}\left[\|\hat{\mathbf{g}}_k\|^2\right] = \mathrm{Tr}\left(\mathbf{C}_{\hat{g}_k}\right) = \frac{\mathrm{Tr}\left(\mathbf{C}_{\hat{g}}\right)}{K},
\end{aligned}
$$

where the fact that the LMMSE channel estimate is uncorrelated with the channel estimation error and that the covariance matrices of the estimated channels for each of the users are equal is used. Further,

$$
\begin{aligned}
&\operatorname{var}\left(\hat{\mathbf{g}}_k^H \mathbf{g}_k\right)\\
=&\mathbb{E}\left[\left|\hat{\mathbf{g}}_k^H \mathbf{g}_k\right|^2\right] - \left(\mathbb{E}\left[\hat{\mathbf{g}}_k^H \mathbf{g}_k\right]\right)^2\\
=&\mathbb{E}\left[\left|\|\hat{\mathbf{g}}_k\|^2 + \hat{\mathbf{g}}_k^H \boldsymbol{\epsilon}_k\right|^2\right] - \left(\mathbb{E}\left[\hat{\mathbf{g}}_k^H \mathbf{g}_k\right]\right)^2\\
=&\mathbb{E}\left[\|\hat{\mathbf{g}}_k\|^4\right] + \mathbb{E}\left[\|\hat{\mathbf{g}}_k\|^2 \hat{\mathbf{g}}_k^H \boldsymbol{\epsilon}_k\right] + \mathbb{E}\left[\|\hat{\mathbf{g}}_k\|^2 \boldsymbol{\epsilon}_k^H \hat{\mathbf{g}}_k\right] +\\
&\quad \mathbb{E}\left[\|\hat{\mathbf{g}}_k^H \boldsymbol{\epsilon}_k\|^2\right] - \left(\mathbb{E}\left[\hat{\mathbf{g}}_k^H \mathbf{g}_k\right]\right)^2\\
=&2\left(\mathbb{E}\left[\|\hat{\mathbf{g}}_k\|^2\right]\right)^2 + \mathbb{E}\left[\|\hat{\mathbf{g}}_k\|^2\right] \mathbb{E}\left[\|\boldsymbol{\epsilon}_k\|^2\right] - \left(\mathbb{E}\left[\hat{\mathbf{g}}_k^H \mathbf{g}_k\right]\right)^2\\
=&\left(\operatorname{Tr}\left(\mathbf{C}_{\hat{g}_k}\right)\right)^2 + \operatorname{Tr}\left(\mathbf{C}_{\hat{g}_k}\right)\left[\operatorname{Tr}\left(\mathbf{C}_G\right) - \operatorname{Tr}\left(\mathbf{C}_{\hat{g}_k}\right)\right]\\
=&\operatorname{Tr}\left(\mathbf{C}_{\hat{g}_k}\right)\operatorname{Tr}\left(\mathbf{C}_G\right) = \frac{\operatorname{Tr}\left(\mathbf{C}_{\hat{g}}\right)\operatorname{Tr}\left(\mathbf{C}_G\right)}{K},
\end{aligned}
$$

and, for $i \neq k$,

$$
\mathbb{E}\left[\left|\hat{\mathbf{g}}_k^H \mathbf{g}_i\right|^2\right] = \left|\mathbb{E}\left[\hat{\mathbf{g}}_k^H \mathbf{g}_i\right]\right|^2 + \mathbb{E}\left[\|\hat{\mathbf{g}}_k\|^2\right] \mathbb{E}\left[\|\mathbf{g}_i\|^2\right],
$$

$$
\mathbb{E}\left[\hat{\mathbf{g}}_k^H \mathbf{g}_i\right] = \mathbb{E}\left[\left(\mathbf{P}_k \boldsymbol{\Phi} \mathbf{g} + \mathbf{P}_k \mathbf{n} + \mathbf{P}_k \mathbf{U}^{-1} \mathbf{q}\right)^H \mathbf{g}_i\right],
$$

where $\mathbf{P}_k = \mathbf{C}_{g_{(k-1)M:kM,:}} \boldsymbol{\Phi} \mathbf{C}_y^{-1}$ and $\mathbf{C}_{g_{(k-1)M:kM,:}}$ refers to the kth block of rows of $\mathbf{C}_g$, and where the expression for $\hat{\mathbf{g}}_k$ is substituted for in the above equation. Then, using the fact that $\mathbf{g}_i$ is uncorrelated with the quantization noise and the additive noise, we get

$$
\mathbb{E}\left[\left|\hat{\mathbf{g}}_k^H \mathbf{g}_i\right|^2\right] = \frac{\operatorname{Tr}\left(\mathbf{C}_{\hat{g}}\right)\operatorname{Tr}\left(\mathbf{C}_G\right)}{K}.
$$

We can solve for the final term in the denominator in a similar manner to get:

$$
\mathbb{E}\left[\left|\hat{\mathbf{g}}_k^H \mathbf{U}_d^{-1} \mathbf{q}\right|^2\right] = \frac{\operatorname{Tr}\left(\mathbf{C}_{\hat{g}}\right)\operatorname{Tr}\left(\mathbf{U}_d^{-1} \mathbf{C}_{q_d} \mathbf{U}_d^{-H}\right)}{K}.
$$

Note that when there is perfect knowledge of the CSI, i.e. $\mathbf{w}_k = \mathbf{g}_k$, (5.35) reduces to the expression derived in [103]. The ratio inside the logarithm of (5.35) shows the impact of the various system parameters on the SNR for each of the users. The three terms in the denominator show the contribution of the multi-user interference (MUI), the receiver noise, and the quantization noise, respectively.

5.3.2 ZF receiver

The composite noise at the output of the $\Sigma\Delta$ array is spatially correlated and its covariance matrix is given by $\mathbf{C}_{\tilde{n}} = \left(\mathbf{C}_N + \mathbf{U}_d^{-1}\mathbf{C}_{q_d}\mathbf{U}_d^{-H}\right)$. Thus, the ZF equalizer becomes

$$\mathbf{W}_{\mathrm{ZF}} = \mathbf{C}_{\tilde{n}}^{-1}\hat{\mathbf{G}}\left(\hat{\mathbf{G}}^H\mathbf{C}_{\tilde{n}}^{-1}\hat{\mathbf{G}}\right)^{-1} . \tag{5.36}$$

The expectations required to compute (5.36) are significantly more complicated than for the case of MRC, and are intractable to evaluate in closed-form. The achievable rate of the kth user can be expressed as in (5.38), where the term $\mathbb{E}\left[\left(\hat{\mathbf{G}}^H\mathbf{C}_{\tilde{n}}^{-1}\hat{\mathbf{G}}\right)_{kk}\right]$ is computed empirically. The remaining terms in the expression can be found as follows. For the numerator,

$$\mathbb{E}\left[\mathbf{w}_k^H\mathbf{g}_k\right] = \mathbb{E}\left[\mathbf{w}_k^H\left(\hat{\mathbf{g}}_k + \boldsymbol{\epsilon}_k\right)\right] = 1 + \mathbb{E}\left[\mathbf{w}_k^H\boldsymbol{\epsilon}_k\right] = 1 . \tag{5.37}$$

Further,

$$\mathrm{var}\left(\mathbf{w}_k^H\mathbf{g}_k\right) = \mathbb{E}\left[\left\|\mathbf{w}_k^H\boldsymbol{\epsilon}_k\right\|^2\right] = \frac{\mathbb{E}\left[\left(\hat{\mathbf{G}}^H\mathbf{C}_{\tilde{n}}^{-1}\hat{\mathbf{G}}\right)_{kk}\right]\mathrm{Tr}\left(\mathbf{C}_\epsilon\right)}{K} .$$

For $i \neq k$, we have

$$\mathbb{E}\left[\left|\mathbf{w}_k^H\mathbf{g}_i\right|^2\right] = \mathbb{E}\left[\left|\mathbf{w}_k^H\boldsymbol{\epsilon}_i\right|^2\right] = \frac{\mathbb{E}\left[\left(\hat{\mathbf{G}}^H\mathbf{C}_{\tilde{n}}^{-1}\hat{\mathbf{G}}\right)_{kk}\right]\mathrm{Tr}\left(\mathbf{C}_\epsilon\right)}{K} .$$

Similarly, we obtain

$$\mathbb{E}\left[\left|\mathbf{w}_k^H \mathbf{n}_d\right|^2\right] = \mathbb{E}\left[\left(\hat{\mathbf{G}}^H \mathbf{C}_{\tilde{n}}^{-1} \hat{\mathbf{G}}\right)_{kk}^{-1}\right] \mathrm{Tr}\left(\mathbf{C}_N\right),$$

$$\mathbb{E}\left[\left|\mathbf{w}_k^H \mathbf{U}_d^{-1} \mathbf{q}\right|^2\right] = \mathbb{E}\left[\left(\hat{\mathbf{G}}^H \mathbf{C}_{\tilde{n}}^{-1} \hat{\mathbf{G}}\right)_{kk}^{-1}\right] \mathrm{Tr}\left(\mathbf{U}_d^{-1} \mathbf{C}_{q_d} \mathbf{U}_d^{-H}\right).$$

$$R_k^{\mathrm{ZF}} = \log_2\left(1 + \frac{\rho_d}{\rho_d \mathbb{E}\left[\left(\hat{\mathbf{G}}^H \mathbf{C}_{\tilde{n}}^{-1} \hat{\mathbf{G}}\right)_{kk}^{-1}\right]\mathrm{Tr}\left(\mathbf{C}_\epsilon\right) + \mathbb{E}\left[\left(\hat{\mathbf{G}}^H \mathbf{C}_{\tilde{n}}^{-1} \hat{\mathbf{G}}\right)_{kk}^{-1}\right]\mathrm{Tr}\left(\mathbf{C}_{\tilde{n}}\right)}\right) \tag{5.38}$$

5.3.3 LMMSE receiver

The LMMSE receiver minimizes the mean squared error in estimating s_k and can be expressed as [139, 140]

$$\mathbf{W}_{\mathrm{MMSE}} = \left(\rho_d \hat{\mathbf{G}}\hat{\mathbf{G}}^H + \rho_d \mathbf{C}_{\tilde{\epsilon}} + \mathbf{C}_{\tilde{n}}\right)^{-1}\hat{\mathbf{G}}, \tag{5.39}$$

where $\mathbf{C}_{\tilde{\epsilon}}$ is one of the sub-blocks along the block diagonal of $\mathbf{C}_\epsilon$ in (5.26). As in the case of ZF, the form of the LMMSE receiver does not lend itself to calculation of closed-form expressions for the expectations required to evaluate (5.33), and hence in the next section the lower bound on the achievable rate for this approach is numerically evaluated.

5.4 Simulation Results

In this section, the NE and sum spectral efficiency achieved with the $\Sigma\Delta$ massive MIMO system using one or two-bit outputs are numerically evaluated. The inter-element spacing
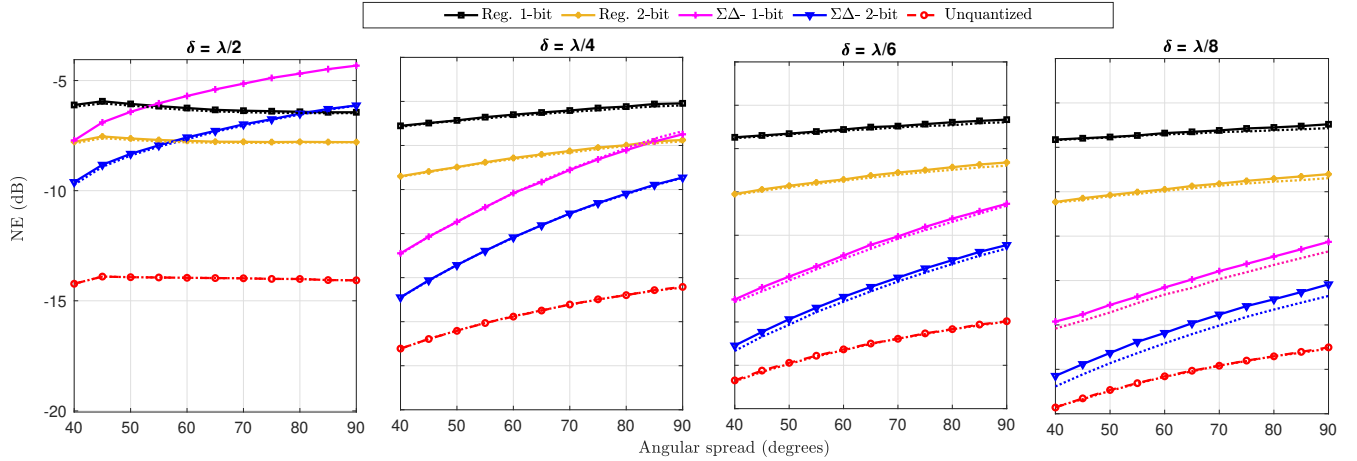
Figure 5.1: NE of channel estimates for different angular spreads of user AoAs and inter-element antenna spacings.
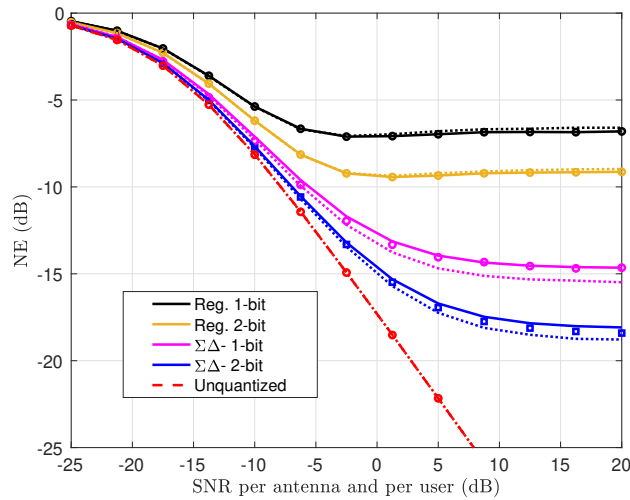
Figure 5.2: NE of channel estimate, $M = 128, N = K = 10$.

is defined by δ, and unless otherwise indicated, the simulations will employ a uniform linear array (ULA) equipped with 128 antennas. The number of pilot symbols and number of users are both 10 ($N = K = 10$), and orthogonal pilot sequences are used based on the $N \times N$ DFT matrix. It is further assumed that the downlink transmission power is equal to the pilot transmission power, i.e. $\rho_d = \rho$.

The users are assumed to be located within a sector centered on the broadside of the antenna

array, so the steering angle of the $\Sigma\Delta$ array is set to $\psi = 0°$, and $\mathcal{S}_\theta = [-\frac{\Theta}{2}, \frac{\Theta}{2}]$. It is assumed the spatial covariance matrix is the same for all users, and defined by $L = 50$ uniformly spaced signal arrivals θ_l in the interval defined by $\mathcal{S}_\theta$. The parameters used in modeling the mutual coupling of the array are: $R = 50\ \Omega$, $T_A = 290$ K, $\varrho_n = 0$, $B = 20$ MHz, $R_N = R$, $\sigma_i^2 = 2k_B T_A B/R$, and $\sigma_v^2 = 2k_B T_A BR$. The simulations performed in the absence of mutual coupling assume that $\mathbf{Z} = R\mathbf{I}$ and $\mathbf{T} = 0.5\mathbf{I}$ [113].

The NE of the channel estimate is evaluated over 500 independent realizations of the channel. For two-bit ADCs, the optimum levels $\{\nu_1, \nu_2, \nu_3, \nu_4\}$ as per [119] are chosen. The sum spectral efficiency as a performance measure defined as

$$\text{SE} = \frac{T - N}{T} \sum_{i=1}^{K} R_k, \tag{5.40}$$

is used, where T is length of the coherence interval during which the channel remains constant. It is assumed that $T = 200$ symbols.

The performance of the $\Sigma\Delta$ LMMSE channel estimator derived above is compared with the one-bit Bussgang LMMSE (BLMMSE) channel estimator of [27] and the LMMSE channel estimate for standard two-bit quantization. The LMMSE algorithm for the two-bit case can be derived by combining the analysis of [27] with that in Sections 4.2.2 and 5.2 by replacing r_m with x_m. The NE of an LMMSE channel estimator using unquantized measurements is also evaluated. Fig. 5.1 shows the estimation performance as a function of the angular spread Θ of the user AoAs for four different antenna spacings. Dotted lines indicate the NE of the channel estimate when there is no mutual coupling, circles indicate analytical values and lines indicate simulated results. As expected, the performance of the spatial $\Sigma\Delta$ approach improves as either the antenna spacing δ or the size of the users' angular spread Θ decreases. Without oversampling, i.e., when $\delta = \lambda/2$, the $\Sigma\Delta$ array offers no benefit over regular one- and two-bit quantization, except for a very narrow region near broadside, since the signals

at adjacent antennas are less correlated. For $\delta \leq \lambda/4$, however, there is a significant gain for angular sectors up to 90° and beyond. The dotted lines in the plots show the performance of the $\Sigma\Delta$ channel estimator if the effect of mutual coupling is removed. While mutual coupling increasingly degrades the channel estimation performance as the antenna spacing decreases, the overall effect is not large. For the remaining numerical examples, we will set $\Theta = 60°$ and $\delta = \lambda/6$.

Fig. 5.2 shows the NE of the channel estimates as a function of SNR with $M = 128$ antennas. The solid lines show the NE predicted by (5.24), the symbols indicate the simulation results, and the dotted lines show the performance without the effect of mutual coupling (this convention will be followed in all subsequent plots). It is seen that there is excellent agreement between our theoretical expression and the simulations. At low-to-medium SNRs, the performance of the $\Sigma\Delta$ channel estimates is very close to that of the unquantized MMSE channel estimate. The NE with two-bit $\Sigma\Delta$ ADCs is also lower than that achieved by one-bit $\Sigma\Delta$ ADCs beyond an SNR of -5dB. The gap between the two widens as the SNR increases and the error floor is about -15dB with one-bit $\Sigma\Delta$ ADCs and -18dB with two-bit $\Sigma\Delta$ ADCs. It is seen that LMMSE channel estimation with the $\Sigma\Delta$ array offers a significant advantage over the conventional one-bit and two-bit quantized arrays. The error floor of the $\Sigma\Delta$ channel estimators is around 8-9dB lower than their counterparts employing standard quantization. The advantage of the spatial $\Sigma\Delta$ approach is further seen in Fig. 5.3 where performance is plotted as a function of M for a fixed SNR of 0dB. These results indicate that the loss due to mutual coupling diminishes as the size of the array grows.

In Fig. 5.4, the theoretical and simulated sum spectral efficiency (SE) achieved by the MRC, ZF and LMMSE receivers using the LMMSE channel estimate are plotted. Fig. 5.4(a) shows that the SE of the $\Sigma\Delta$ architectures is close to that of an unquantized system and a bit higher than that of the one-bit massive MIMO system, although for MRC the difference in SE is not so large since multi-user interference is more of a limiting factor. There is excellent
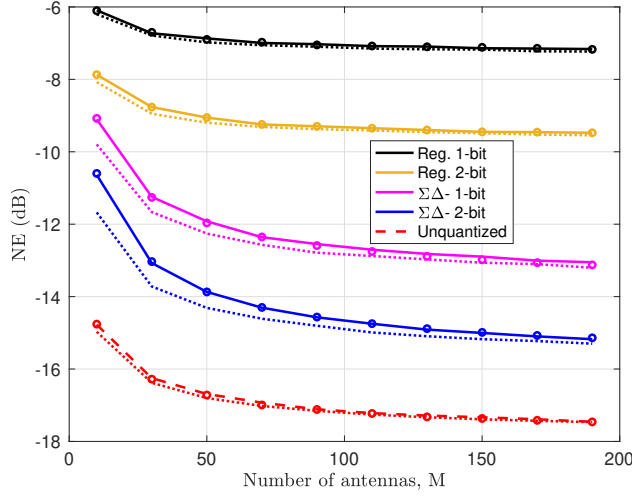
Figure 5.3: NE of channel estimate as a function of the number of antennas, SNR = 0dB.

agreement between the simulations and our analytical expression in (5.35). More impressive results are obtained for the case of a ZF receiver, as shown in Fig. 5.4(b). At high SNRs, the throughput achieved with two-bit $\Sigma\Delta$ ADCs is around 60 bits/s/Hz, almost 2.5 times that achieved with regular two-bit ADCs. With one-bit $\Sigma\Delta$ ADCs, the maximum throughput is around 50 bits/s/Hz, also around 2.5 times that achieved with regular one-bit ADCs. Of course, there is also a much bigger gap between the spectral efficiencies achievable by the $\Sigma\Delta$ and unquantized systems as well, especially at high SNR. From Fig. 5.4 (c), it is seen that the performance of the LMMSE receiver is nearly identical to that of the ZF receiver since the number of users is fairly small ($K = 10$).

Finally, Fig. 5.5 shows a plot of the average per-user achievable rate for the MRC (dotted lines), ZF (dash-dotted lines) and LMMSE (dashed lines) receivers versus the total number of users. For MRC, the per-user rate achieved with both the one-bit and two-bit $\Sigma\Delta$ ADC arrays is essentially identical to that achieved without quantization. The numerator term of the logarithm in (5.35) decreases with K while the inter-user interference term in the denominator increases with K. The net effect is that, as the number of uplink users increases, the effective SNR per user for MRC decreases as $O(K^2)$. When K is not too large, the per-
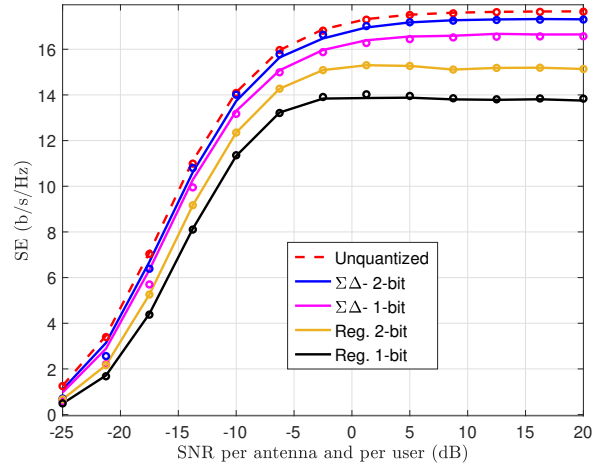
(a)
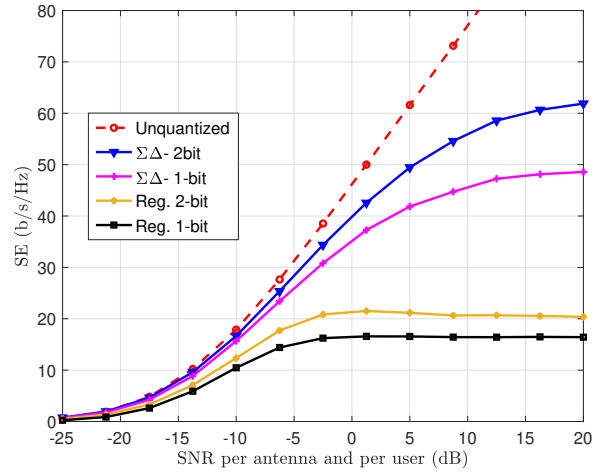
(b)
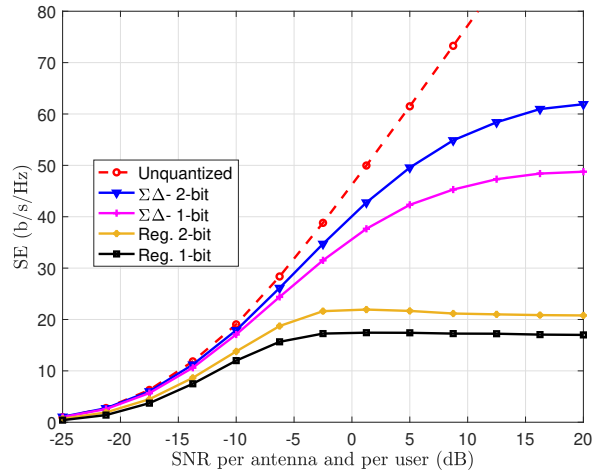
(c)

Figure 5.4: Sum spectral efficiency (SE) with (a) MRC (b) ZF (c) LMMSE receivers ($M = 128, K = 10$).
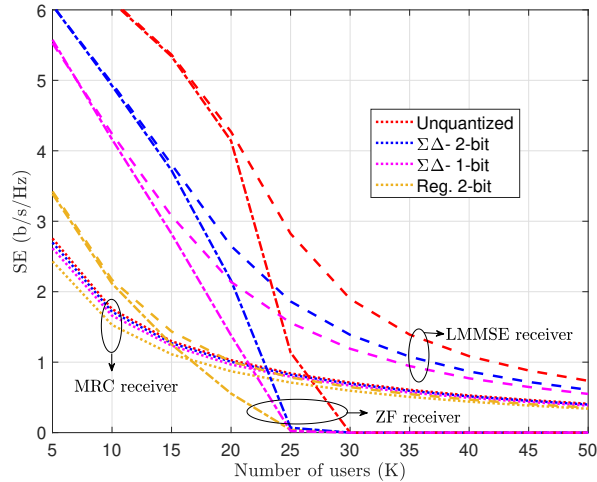
Figure 5.5: Per-user achievable rate as a function of the number of users, SNR = 5dB, $M = 128$.

user rate for ZF is significantly higher than for MRC, with the $\Sigma\Delta$ architecture falling in between the standard one-bit and unquantized systems. For an average per-user rate of 2 bits/s/Hz, MRC can support 7-8 users almost independently of the quantization level, while for ZF/LMMSE the number of users increases to 10 for standard two-bit quantization, and 16-24 for the $\Sigma\Delta$ array. As the number of users increases, the channel matrix becomes ill-conditioned and the sum rate achieved with the ZF receiver tends towards zero. This is primarily due to the fact that the users' signals are confined to arrive from a $60°$ angular sector. However, the LMMSE receiver is more robust and continues to provide a positive, albeit decreasing, average rate for the users even as K is increasing.

5.5 Conclusion

In this chapter, channel estimation in massive MIMO systems employing spatial $\Sigma\Delta$ modulation with one- or two-bit ADCs was considered. The LMMSE channel estimator takes into account the effect of the correlation between the quantizer outputs. The uplink rate that is achievable for MRC, ZF and LMMSE receivers implemented with the LMMSE channel

estimate was analyzed and the simulation results show that, in situations where the users are confined to a certain angular sector or the array elements are more closely spaced than one-half wavelength, the spatial $\Sigma\Delta$ approach is able to achieve significantly better channel estimates and spectral efficiency than systems employing direct quantization using one- and two-bit ADCs. At low-to-medium SNR values, the performance gap between the $\Sigma\Delta$ array and a system with infinite-resolution ADCs is negligible.

Chapter 6

Two-Dimensional Direction Finding with Low-Resolution Sigma-Delta ADCs

In this chapter, the problem of estimating the azimuth and elevation angles with spatial $\Sigma\Delta$ ADCs is considered. A scenario typical to sectorized cells where the antennas are mounted on top the tower is considered where the desired field of view is wide in the azimuth domain and relatively narrow in the elevation domain since most users are on the ground. Even in indoor settings, antenna arrays are mounted on a wall and most users are concentrated around a small angular sector in the elevation domain. Thus, a rectangular array architecture in which the spatial $\Sigma\Delta$ processing occurs only along the vertical dimension of the array is considered, as shown in Fig. 6.1.
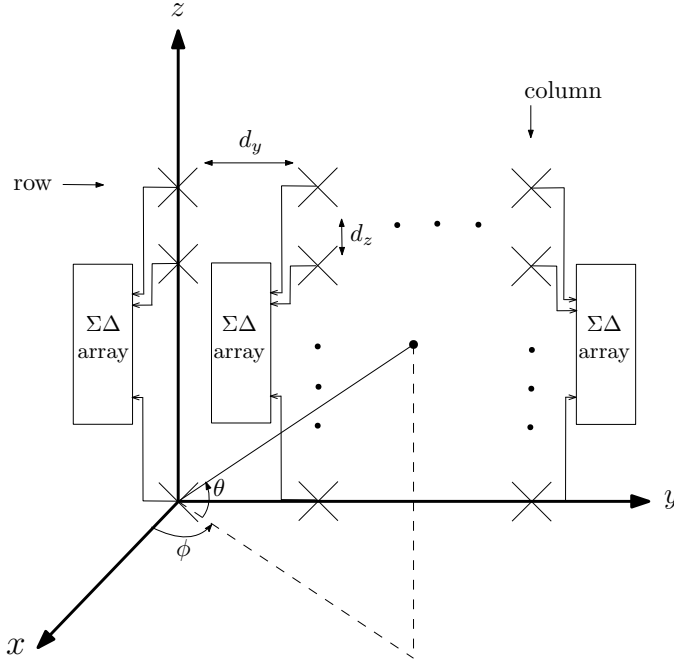
Figure 6.1: Rectangular antenna array in the yz plane.

6.1 System Model

6.1.1 Nominal System Model

The RA consists of M antennas separated by d_y in each row and N antennas separated by d_z in each column. It is assumed that K signals impinge on the array and the direction associated with each signal is dependent on its azimuth and elevation angles, ϕ_k and θ_k, respectively.

It is assumed that the elevation angles of the incoming signals from the users lie in a known narrow angular region $\theta_k \in \mathcal{S}_\theta$, while the azimuth angles are distributed over a wider range. This scenario is common to many practical situations where the elevation angles of various users are nearly the same or limited to a small range around the array broadside. It has been demonstrated that $\Sigma\Delta$ arrays exhibit superior performance compared to standard quantization arrays [101, 103] when the DOAs are confined to a narrow range in addition to, or in lieu of, the BS array being oversampled in space. Additionally, space constraints restrict

the number of antennas that can be placed in a fixed physical space, as well as how small the spacing between adjacent antennas can be. There is a limit on how close the antennas can be placed together before the loss due to mutual coupling becomes substantial. Drawing from these ideas, an RA configuration for which each column consists of a first-order spatial $\Sigma\Delta$ ADC array with spacing $d_z \leq \lambda/2$, is considered and therefore, the impact of mutual antenna coupling between elements of each column is significant. Since the azimuth range is much wider, the horizontal spacing is set to $d_y = \lambda/2$, and hence, it is assumed that the mutual coupling between elements across each row is negligible. The received signal from each column of the RA is collected and stacked on top of each other at time t and is given by

$$\mathbf{x}\left(t\right) = \mathbf{G}\left(\boldsymbol{\theta}, \boldsymbol{\phi}\right)\mathbf{s}\left(t\right) + \mathbf{n}\left(t\right), \tag{6.1}$$

where $\mathbf{G}\left(\boldsymbol{\theta}, \boldsymbol{\phi}\right) \in \mathbb{C}^{MN \times K}$ is the array manifold over the unknown user elevation and azimuth angles, $\boldsymbol{\theta} = \left[\theta_1, \theta_2, \ldots, \theta_K\right]^T$ and $\boldsymbol{\phi} = \left[\phi_1, \phi_2, \ldots, \phi_K\right]^T$, respectively, the K signals at time t are stacked in $\mathbf{s}(t) \in \mathbb{C}^{K \times 1}$, and $\mathbf{n}(t) \in \mathbb{C}^{MN \times 1}$ is the additive noise. It is assumed that the noise is temporally white but not necessarily spatially white. While the various sources of noise, such as thermal noise or the noise from the front-end amplifiers, are independent, mutual coupling between antennas produces colored noise at the output of the receiver. Therefore, the noise is assumed to be a zero-mean Gaussian random process with a known covariance matrix, $\mathbf{C}_n$, i.e.,

$$
\begin{aligned}
\mathbb{E}\left[\mathbf{n}(t_1)\mathbf{n}^H(t_2)\right] &= \mathbf{C}_n\, \delta_{t_1 t_2} \\
\mathbb{E}\left[\mathbf{n}(t_1)\mathbf{n}^T(t_2)\right] &= \mathbf{0}.
\end{aligned}
\tag{6.2}
$$

The array manifold $\mathbf{G}\left(\boldsymbol{\theta}, \boldsymbol{\phi}\right)$ incorporates the mutual coupling between elements represented

by the mutual coupling matrix (MCM), $\mathbf{T}$, and is given by

$$\mathbf{G}\left(\boldsymbol{\theta},\boldsymbol{\phi}\right)=\mathbf{T}\mathbf{A}\left(\boldsymbol{\theta},\boldsymbol{\phi}\right),\tag{6.3}$$

where the columns of the $MN\times K$ matrix $\mathbf{A}\left(\boldsymbol{\theta},\boldsymbol{\phi}\right)$ are the array steering vectors $\mathbf{a}(\theta_k,\phi_k)$, $k=1,\ldots,K$. It is assumed that the functional form of nominal array response, $\mathbf{a}(\theta,\phi)$, is known and that the sensors are omnidirectional so that $\|\mathbf{a}(\theta,\phi)\|_2=\sqrt{MN}$. Slightly different notations for the mutual coupling matrix $\mathbf{T}$ and the spatial noise covariane matrix $\mathbf{C}_n$ will be used as

$$\begin{aligned}\mathbf{T}&=\mathbf{I}_M\otimes\left(\mathbf{I}_N+\frac{1}{R}\mathbf{Z}\right)^{-1},\\[2mm]\mathbf{C}_n&=\mathbf{T}\boldsymbol{\Upsilon}\mathbf{T}^H,\end{aligned}\tag{6.4}$$

where R is the input impedance of the LNA, and $\mathbf{Z}$ and $\boldsymbol{\Upsilon}$ are specified by Eqs. (4.29) and (4.31), respectively.

Let $\mathbf{g}\left(\theta,\phi\right)=\mathbf{T}\,\mathbf{a}\left(\theta,\phi\right)$. The following standard assumptions are made on the signal model:

1. The source DOAs are distinct, i.e. $\mathbf{g}\left(\theta_k,\phi_k\right)=\mathbf{g}\left(\theta_j,\phi_j\right)$, iff $\theta_j=\theta_k$ and $\phi_j=\phi_k$.

2. The additive noise is uncorrelated with the source signals.

3. The source signals follow the unconditional model [141], and are circularly symmetric Gaussian distributed with covariance matrix $\mathbf{C}_s$.

4. The array response vectors corresponding to distinct set of DOAs are orthogonal for

large M and N, i.e.

$$\frac{1}{MN}\mathbf{a}^H(\theta_k, \phi_k)\mathbf{a}(\theta_j, \phi_j) = \begin{cases} 1, & \text{iff} \quad \theta_j = \theta_k, \\ & \qquad \phi_j = \phi_k \\ 0, & \text{otherwise.} \end{cases}$$

Defining $\mathbf{S} = [\mathbf{s}(t_1) \dots \mathbf{s}(t_T)]$ and collecting the received signal over T time instants in $\mathbf{X}$, we have

$$\mathbf{X} = \mathbf{G}\left(\boldsymbol{\theta}, \boldsymbol{\phi}\right)\mathbf{S} + \mathbf{N}, \tag{6.5}$$

where $\mathbf{N} = [\mathbf{n}(t_1) \dots \mathbf{n}(t_T)]$ and the output of the $\Sigma\Delta$ array is given by

$$\begin{aligned} \mathbf{Y} &= \mathcal{Q}_{\Sigma\Delta}\left(\mathbf{X}\right) = \mathcal{Q}\left(\mathbf{R}\right) \\ \mathbf{R} &= \mathbf{U}\mathbf{X} - \mathbf{V}\mathbf{Y}, \end{aligned} \tag{6.6}$$

where $\mathbf{U}$ and $\mathbf{V}$ are $MN \times MN$ matrices defined in Eq. (5.13). Using (6.6) and the equivalent linear model in (4.11) and rearranging the terms, we get

$$\mathbf{Y} = \mathbf{X} + \mathbf{U}^{-1}\mathbf{Q}, \tag{6.7}$$

where $\mathbf{Q}$ is the quantization noise matrix defined similar to $\mathbf{X}$. The output covariance matrix, upon which the MUSIC algorithm depends, can be derived using the above equivalent linear model. The nominal covariance matrix of $\mathbf{X}$ and $\mathbf{Y}$ are respectively given by

$$\begin{aligned} \mathbf{C}_x &= \mathbf{G}\left(\boldsymbol{\theta}, \boldsymbol{\phi}\right)\mathbf{C}_s\mathbf{G}^H\left(\boldsymbol{\theta}, \boldsymbol{\phi}\right) + \mathbf{C}_n \\ \mathbf{C}_y &= \mathbf{G}\left(\boldsymbol{\theta}, \boldsymbol{\phi}\right)\mathbf{C}_s\mathbf{G}^H\left(\boldsymbol{\theta}, \boldsymbol{\phi}\right) + \mathbf{C}_n + \mathbf{U}^{-1}\mathbf{C}_q\mathbf{U}^{-H}, \end{aligned} \tag{6.8}$$

where $\mathbf{C}_q = \text{diag}\{\sigma_{q_{11}}^2, \dots, \sigma_{q_{NM}}^2\}$. The equivalent additive plus quantization noise at the

output of the $\Sigma\Delta$ array, denoted by $\mathbf{W}$, is given by

$$\mathbf{W} = \mathbf{C}_n + \mathbf{U}^{-1}\mathbf{C}_q\mathbf{U}^{-H}. \tag{6.9}$$

6.1.2   Perturbed System Model

In any practical situation, a number of error sources are present simultaneously and affect the DOA estimation performance. In particular, model similar to those in [116, 142] is used and it is assumed that the most significant factors contributing to error are:

- Finite sample effects,

- A perturbed array manifold,

- Inaccurate noise covariance matrix.

Given enough samples T and a sufficiently high SNR, the finite sample effects can be neglected and the dominant sources of error are the imperfect assumptions on the array manifold and the noise covariance.

The perturbations in the array manifold are a result of the fact that the array response may not be known at all times. The array response at the time of measurement may be different from that noted during the time of calibration due to changes in the surrounding environment. The output of the $\Sigma\Delta$ array is assumed to be actually generated from the model:

$$\mathbf{Y} = \mathbf{T}\left(\sqrt{1-\epsilon^2}\mathbf{A}\left(\boldsymbol{\theta}, \boldsymbol{\phi}\right) + \epsilon\tilde{\mathbf{A}}\right)\mathbf{S} + \mathbf{U}^{-1}\mathbf{Q} + \mathbf{N}, \tag{6.10}$$

where ϵ is the standard deviation of perturbation and $\tilde{\mathbf{A}}$ is the perturbation matrix. The perturbations may be due to imprecisely known sensor locations, gain errors, phase errors,

mutual coupling modeling errors, etc. Since a combination of these factors is likely to be present simultaneously, it is reasonable to model the aggregate array response as a random quantity whose mean is the nominal array response $\mathbf{A}(\boldsymbol{\theta}, \boldsymbol{\phi})$. The elements of the array perturbation $\tilde{\mathbf{A}}$, $\tilde{a}_{ij}$, are assumed to be drawn from the distribution $\tilde{a}_{ij} \sim \mathcal{CN}(0, 1)$.

The assumptions on the noise covariance may also not always be valid. The noise field is often unknown and may vary with time, there may be undesirable cross-talk and interference, and the modeling of the quantization noise statistics may be inaccurate. The noise perturbation represents deviations in the statistics of both the additive noise as well as the quantization noise. As with the array perturbation, the perturbation to the noise covariance is modeled as a random variable with known moments. Letting $\mathbf{q}(t)$ be the quantization noise at time t, the "effective" noise at time t, $\tilde{\mathbf{n}}(t) = \mathbf{U}^{-1}\mathbf{q}(t) + \mathbf{n}(t)$, is zero-mean with conditional covariance:

$$
\begin{aligned}
\mathbb{E}\left[\tilde{\mathbf{n}}(t_1)\tilde{\mathbf{n}}^H(t_2)|\tilde{\mathbf{W}}\right] &= \left(\mathbf{W} + \tilde{\mathbf{W}}\right)\delta_{t_1 t_2}, \\
\mathbb{E}\left[\tilde{\mathbf{n}}(t_1)\tilde{\mathbf{n}}^T(t_2)|\tilde{\mathbf{W}}\right] &= \mathbf{0},
\end{aligned}
\tag{6.11}
$$

where $\tilde{\mathbf{W}} \in \mathbb{C}^{MN \times MN}$, the perturbation to the noise covariance matrix, is a Hermitian matrix. Like in [116], $\tilde{\mathbf{W}}$ is treated as a random matrix with zero mean and whose elements, $\tilde{w}_{ij}$, are independent and have variance μ^2, i.e.,

$$
\mathbb{E}[\tilde{w}_{ij}\tilde{w}_{kl}] = \mu^2 \delta_{ik}\delta_{jl}.
\tag{6.12}
$$

From (6.11), it can be seen that the total covariance matrix of the noise is identical to the nominal covariance $\mathbf{W}$. However, the estimation of $[\boldsymbol{\theta}, \boldsymbol{\phi}]$ is affected by the higher order moments of the noise and therefore by the perturbation model. For $\Sigma\Delta$ and standard coarse quantization, the presence of quantization noise at high SNRs results in a biased estimate. The perturbations introduce an additional bias in the estimates and, as a consequence,

the estimation error does not reduce to zero despite increasing the SNR or the number of snapshots T even when the ADCs have ideal resolution. However, in order to develop a mathematically consistent analysis where the covariance of the estimation error depends on both the finite-sample and model errors, we will follow an approach as in [116] to keep their relative magnitudes comparable. This is performed by using the following limiting definitions of perturbation variances:

$$\mu^2 = \tilde{\mu}^2/T$$
$$\epsilon^2 = \tilde{\epsilon}^2/T \tag{6.13}$$

where $\tilde{\mu}$ and $\tilde{\epsilon}$ are independent of T. Then, when the asymptotic performance analysis is carried out assuming that $T \to \infty$, it is ensured that the contribution from modeling errors is commensurate with that from finite-sample effects and neither source of error dominates the other.

6.1.3 Estimation Methods

Various approaches to DOA estimation using one-bit measurements have been considered, for instance, subspace based approaches on ULAs are used in [66, 68, 71, 143], compressed sensing based methods are used in [69, 70, 144] and sparse array estimation is considered in [67, 68, 145]. In [108, 109], the AoAs and AoDs that characterize a sparse mmWave channel are estimated with $\Sigma\Delta$ quantized measurements using MUSIC and beamforming, respectively. However, an analysis of the asymptotic estimation error was not performed. In this section, a closed-form expression for the covariance matrix of the asymptotic estimation error will be derived when the output of the $\Sigma\Delta$ is generated from the perturbed system model in (6.10).

The estimation of $\boldsymbol{\theta}$ and $\boldsymbol{\phi}$ depends on the sample covariance matrix, $\hat{\mathbf{C}}_y$,

$$\hat{\mathbf{C}}_y = \frac{1}{T}\mathbf{Y}\mathbf{Y}^H \tag{6.14}$$

and since the effective noise is spatially correlated, the estimation is based on the prewhitened sample covariance matrix, $\mathbf{W}^{-\frac{1}{2}}\hat{\mathbf{C}}_y\mathbf{W}^{-\frac{1}{2}}$, which takes the form

$$
\begin{aligned}
\mathbf{W}^{-\frac{1}{2}}\hat{\mathbf{C}}_y\mathbf{W}^{-\frac{1}{2}} = {} & \left(\sqrt{1-\epsilon^2}\,\bar{\mathbf{G}} + \epsilon\mathbf{W}^{-\frac{1}{2}}\mathbf{T}\tilde{\mathbf{A}}\right)\hat{\mathbf{C}}_s\left(\sqrt{1-\epsilon^2}\,\bar{\mathbf{G}} + \epsilon\mathbf{W}^{-\frac{1}{2}}\mathbf{T}\tilde{\mathbf{A}}\right)^H \\
& + \left(\sqrt{1-\epsilon^2}\,\bar{\mathbf{G}} + \epsilon\mathbf{W}^{-\frac{1}{2}}\mathbf{T}\tilde{\mathbf{A}}\right)\mathbf{C}_{sn} + \mathbf{C}_{sn}^H\left(\sqrt{1-\epsilon^2}\,\bar{\mathbf{G}} + \epsilon\mathbf{W}^{-\frac{1}{2}}\mathbf{T}\tilde{\mathbf{A}}\right)^H + \mathbf{W}_n.
\end{aligned}
\tag{6.15}
$$

Here,

$$
\begin{aligned}
\bar{\mathbf{G}} &\triangleq \mathbf{W}^{-\frac{1}{2}}\mathbf{G}\left(\boldsymbol{\theta},\boldsymbol{\phi}\right) \\
\hat{\mathbf{C}}_s &= \frac{1}{T}\mathbf{S}\mathbf{S}^H \\
\mathbf{C}_{sn} &= \frac{1}{T}\mathbf{S}\tilde{\mathbf{N}}^H\mathbf{W}^{-\frac{1}{2}} \\
\mathbf{W}_n &= \frac{1}{T}\mathbf{W}^{-\frac{1}{2}}\tilde{\mathbf{N}}\tilde{\mathbf{N}}^H\mathbf{W}^{-\frac{1}{2}},
\end{aligned}
\tag{6.16}
$$

and $\tilde{\mathbf{N}}$ is the effective quantization plus additive noise. The nominal prewhitened covariance matrix and its eigendecomposition are given by

$$\mathbf{W}^{-\frac{1}{2}}\mathbf{C}_y\mathbf{W}^{-\frac{1}{2}} = \bar{\mathbf{G}}\mathbf{C}_s\bar{\mathbf{G}}^H + \mathbf{I}_{MN} = \mathbf{E}_s\boldsymbol{\Lambda}_s\mathbf{E}_s^H + \mathbf{E}_n\mathbf{E}_n^H, \tag{6.17}$$

where the columns of $\mathbf{E}_s \in \mathbb{C}^{MN \times K}$ are the eigenvectors of $\mathbf{W}^{-\frac{1}{2}}\mathbf{C}_y\mathbf{W}^{-\frac{1}{2}}$ corresponding to the signal subspace and the elements of the diagonal matrix $\boldsymbol{\Lambda}_s$ are the respective eigenvalues, and the columns of $\mathbf{E}_n \in \mathbb{C}^{MN \times MN-K}$ are the eigenvectors corresponding to the noise subspace.

In MUSIC, the orthogonality between the signal and noise subspaces is leveraged to find K

distinct minima of the function

$$f_{\mathrm{MU}}\left(\theta, \phi\right) = \mathrm{Tr}\left(\mathbf{P}_{\bar{\mathbf{g}}}\hat{\mathbf{E}}_n \hat{\mathbf{E}}_n^H\right), \tag{6.18}$$

where $\hat{\mathbf{E}}_n$ is an estimate of $\mathbf{E}_n$ and, denoting the functional form of a column of $\bar{\mathbf{G}}$ by $\bar{\mathbf{g}}\left(\theta, \phi\right)$, $\mathbf{P}_{\bar{\mathbf{g}}}$ is the projection matrix

$$\mathbf{P}_{\bar{\mathbf{g}}} = \frac{\bar{\mathbf{g}}\left(\theta, \phi\right)\bar{\mathbf{g}}^H\left(\theta, \phi\right)}{\bar{\mathbf{g}}^H\left(\theta, \phi\right)\bar{\mathbf{g}}\left(\theta, \phi\right)} = \frac{\mathbf{W}^{-\frac{1}{2}}\mathbf{g}\left(\theta, \phi\right)\mathbf{g}^H\left(\theta, \phi\right)\mathbf{W}^{-\frac{1}{2}}}{\mathbf{g}^H\left(\theta, \phi\right)\mathbf{W}^{-1}\mathbf{g}\left(\theta, \phi\right)}.$$

The computational complexity of the associated singular value decomposition (SVD) on the $MN \times MN$ matrix prewhitened covariance matrix is relatively high especially for large MN and to overcome this difficulty, an alternative is to use the traditional beamforming criterion. The beamforming algorithm finds the K distinct minima of the criterion

$$f_{\mathrm{BF}}\left(\theta, \phi\right) = -\mathrm{Tr}\left(\mathbf{P}_{\bar{\mathbf{g}}}\mathbf{W}^{-\frac{1}{2}}\hat{\mathbf{C}}_y \mathbf{W}^{-\frac{1}{2}}\right). \tag{6.19}$$

6.2 Performance analysis

It was shown in [116, 142] that given enough number of samples, expressions for the estimation error can be obtained following a first-order analysis. In this section, we follow similar ideas to derive error expressions for the beamforming and MUSIC algorithms. We derive the asymptotic estimation error covariance matrix under the assumption that the individual sources of error are uncorrelated, that the modeling errors are "small" enough and that T is

"large" enough. For ease of notation, we will define the following matrices

$$
\begin{aligned}
\mathbf{D}_{\boldsymbol{\theta}} &\triangleq \left[\left.\frac{\partial \mathbf{a}\,(\theta, \phi_1)}{\partial \theta}\right|_{\theta=\theta_1}, \ldots, \left.\frac{\partial \mathbf{a}\,(\theta, \phi_K)}{\partial \theta}\right|_{\theta=\theta_K} \right], \\
\mathbf{D}_{\boldsymbol{\phi}} &\triangleq \left[\left.\frac{\partial \mathbf{a}\,(\theta_1, \phi)}{\partial \phi}\right|_{\phi=\phi_1}, \ldots, \left.\frac{\partial \mathbf{a}\,(\theta_K, \phi)}{\partial \phi}\right|_{\phi=\phi_K} \right], \\
\bar{\mathbf{D}}_{\boldsymbol{\theta}} &\triangleq \mathbf{W}^{-\frac{1}{2}}\mathbf{T}\mathbf{D}_{\boldsymbol{\theta}}, \qquad \bar{\mathbf{D}}_{\boldsymbol{\phi}} \triangleq \mathbf{W}^{-\frac{1}{2}}\mathbf{T}\mathbf{D}_{\boldsymbol{\phi}}.
\end{aligned}
\tag{6.20}
$$

In addition to assumption (4) in section 6.1.1 which says that $\mathbf{A}$ is an orthogonal matrix, a standard assumption that is made is that the matrices

$$
\mathbf{A}^H \mathbf{D}_{\boldsymbol{\theta}} \quad \mathbf{A}^H \mathbf{D}_{\boldsymbol{\phi}} \quad \mathbf{D}_{\boldsymbol{\theta}}^H \mathbf{D}_{\boldsymbol{\theta}} \quad \mathbf{D}_{\boldsymbol{\phi}}^H \mathbf{D}_{\boldsymbol{\phi}}
$$

are all diagonal for large MN [146]. Although multiplication by the prewhitening matrix and the mutual coupling matrices compromises orthogonality since they are not unitary matrices in general, the orthogonality assumption is still valid for matrices $\bar{\mathbf{G}}$, $\bar{\mathbf{D}}_{\boldsymbol{\theta}}$ and $\bar{\mathbf{D}}_{\boldsymbol{\phi}}$ when $K \ll MN$. In other words,

$$
\bar{\mathbf{G}}^H \bar{\mathbf{G}} \quad \bar{\mathbf{G}}^H \bar{\mathbf{D}}_{\boldsymbol{\theta}} \quad \bar{\mathbf{G}}^H \bar{\mathbf{D}}_{\boldsymbol{\phi}} \quad \bar{\mathbf{D}}_{\boldsymbol{\theta}}^H \bar{\mathbf{D}}_{\boldsymbol{\theta}} \quad \bar{\mathbf{D}}_{\boldsymbol{\phi}}^H \bar{\mathbf{D}}_{\boldsymbol{\phi}}
$$

are also all diagonal for large M, N.

Let $f(\cdot)$ be an estimator that takes the form of (6.18) for the MUSIC criterion and of (6.19) for the beamforming criterion and let $f(\hat{\theta}_k, \hat{\phi}_k)$ be the function evaluated at the estimated angles of the kth user, $[\hat{\theta}_k, \hat{\phi}_k]$. Using a first-order expansion of the gradient of $f(\hat{\theta}_k, \hat{\phi}_k)$ about the true value $[\theta_k, \phi_k]$, we have

$$
\nabla f(\theta_k, \phi_k) + \nabla^2 f(\theta_k, \phi_k) \begin{pmatrix} \hat{\theta}_k - \theta_k \\ \hat{\phi}_k - \phi_k \end{pmatrix} \simeq \mathbf{0}
\tag{6.21}
$$

where $\nabla f(\theta_k, \phi_k)$ and $\nabla^2 f(\theta_k, \phi_k)$ are, respectively, the gradient and Hessian of $f(\theta, \phi)$ evaluated at $[\theta_k, \phi_k]$. The estimation error is given by

$$\begin{pmatrix} \hat{\theta}_k - \theta_k \\ \hat{\phi}_k - \phi_k \end{pmatrix} = - \left[\nabla^2 f(\theta_k, \phi_k) \right]^{-1} \nabla f(\theta_k, \phi_k). \tag{6.22}$$

The asymptotic second-order statistics of the DOA estimation error is given by

$$\mathbb{E} \left[\begin{pmatrix} \hat{\theta}_k - \theta_k \\ \hat{\phi}_k - \phi_k \end{pmatrix} \begin{pmatrix} \hat{\theta}_k - \theta_k \\ \hat{\phi}_k - \phi_k \end{pmatrix}^T \right] = \frac{1}{T} \left[\nabla^2 f(\theta_k, \phi_k) \right]^{-1} \mathbf{Q}_k \left[\nabla^2 f(\theta_k, \phi_k) \right]^{-1}, \tag{6.23}$$

where $\mathbf{Q}_k$ is the limiting covariance matrix of the gradient and is given by

$$\mathbf{Q}_k = \lim_{T \to \infty} T \mathbb{E} \left[\nabla f(\theta_k, \phi_k) \nabla f(\theta_k, \phi_k)^T \right]. \tag{6.24}$$

Neglecting second-order error terms, the Hessian is shown to be dependent on only finite-sample covariance in [116] and is given by

$$\nabla^2 f_{\mathrm{MU}}(\theta_k, \phi_k) = \frac{2}{\|\bar{\mathbf{g}}_k\|^2} \mathrm{Re} \left(\begin{bmatrix} \bar{\mathbf{d}}_{\theta_k}^H \mathbf{P}_{\bar{\mathbf{G}}}^{\perp} \bar{\mathbf{d}}_{\theta_k} & \bar{\mathbf{d}}_{\theta_k}^H \mathbf{P}_{\bar{\mathbf{G}}}^{\perp} \bar{\mathbf{d}}_{\phi_k} \\ & \\ \bar{\mathbf{d}}_{\theta_k}^H \mathbf{P}_{\bar{\mathbf{G}}}^{\perp} \bar{\mathbf{d}}_{\phi_k} & \bar{\mathbf{d}}_{\phi_k}^H \mathbf{P}_{\bar{\mathbf{G}}}^{\perp} \bar{\mathbf{d}}_{\phi_k} \end{bmatrix} \right) \tag{6.25}$$

for the MUSIC criterion and by

$$\nabla^2 f_{\mathrm{BF}}(\theta_k, \phi_k) = 2 p_k \mathrm{Re} \left(\begin{bmatrix} \bar{\mathbf{d}}_{\theta_k}^H \mathbf{P}_{\bar{\mathbf{g}}_k}^{\perp} \bar{\mathbf{d}}_{\theta_k} & \bar{\mathbf{d}}_{\theta_k}^H \mathbf{P}_{\bar{\mathbf{g}}_k}^{\perp} \bar{\mathbf{d}}_{\phi_k} \\ & \\ \bar{\mathbf{d}}_{\theta_k}^H \mathbf{P}_{\bar{\mathbf{g}}_k}^{\perp} \bar{\mathbf{d}}_{\phi_k} & \bar{\mathbf{d}}_{\phi_k}^H \mathbf{P}_{\bar{\mathbf{g}}_k}^{\perp} \bar{\mathbf{d}}_{\phi_k} \end{bmatrix} \right) \tag{6.26}$$

for the beamforming criterion. Here, p_k is the transmit power of the kth user, $\bar{\mathbf{d}}_{\theta_k}$ and $\bar{\mathbf{d}}_{\phi_k}$

are the kth columns of $\bar{\mathbf{D}}_{\boldsymbol{\theta}}$ and $\bar{\mathbf{D}}_{\boldsymbol{\phi}}$, respectively, and $\mathbf{P}^{\perp}_{\bar{\mathbf{g}}_k}$ and $\mathbf{P}^{\perp}_{\bar{\mathbf{G}}}$ are projection matrices orthogonal to $\bar{\mathbf{g}}\left(\theta_k, \phi_k\right)$ and $\bar{\mathbf{G}}$ given by

$$\mathbf{P}^{\perp}_{\bar{\mathbf{g}}_k} = \mathbf{I}_{MN} - \frac{\bar{\mathbf{g}}\left(\theta_k, \phi_k\right)\bar{\mathbf{g}}^H\left(\theta_k, \phi_k\right)}{\bar{\mathbf{g}}^H\left(\theta_k, \phi_k\right)\bar{\mathbf{g}}\left(\theta_k, \phi_k\right)}$$

$$\mathbf{P}^{\perp}_{\bar{\mathbf{G}}} = \mathbf{I}_{MN} - \bar{\mathbf{G}}\left(\bar{\mathbf{G}}^H\bar{\mathbf{G}}\right)^{-1}\bar{\mathbf{G}}^H.$$

The matrix $\mathbf{Q}_k$ is dependent on the gradient of each criterion and in what follows, an expression for $\mathbf{Q}_k$ and the covariance matrix of the estimation error will be derived.

6.2.1 Beamforming

Using the first-order analysis outlined in (6.21)-(6.23) above, we are able to derive a closed-form expression for the estimation error by computing the expression for $\mathbf{Q}_k$.

Theorem 1: Let $\hat{\theta}_k^{\mathrm{BF}}$ and $\hat{\phi}_k^{\mathrm{BF}}$ be the k-th user DOAs estimated from (6.19). Assuming that the users are uncorrelated and that the assumptions in section 6.1.1 hold, the asymptotic second-order statistics of the estimation errors is given by (6.27) at the top of the next page.

Proof: See Appendix E. ∎

From (6.27), it can be seen that the first term of $\mathbf{Q}_k^{\mathrm{BF}}$ represents the finite sample effects, and the remaining two terms represent the effects of noise modeling errors and array perturbation, respectively.

Theorems 1 shows that in the limiting case $T \to \infty$ the covariance matrix of the estimation error is given by (6.27). However, for finite T, we can substitute $\tilde{\epsilon}^2 = T\epsilon^2$ and $\tilde{\mu}^2 = T\mu^2$ and use (6.23) to predict the variance of the estimation error. When the effects of array perturbation and noise covariance modeling errors are negligible and the limiting source of

$$\mathbb{E}\left[\begin{pmatrix} \hat{\theta}_k - \theta_k \\ \hat{\phi}_k - \phi_k \end{pmatrix}\begin{pmatrix} \hat{\theta}_k - \theta_k \\ \hat{\phi}_k - \phi_k \end{pmatrix}^T\right]$$

$$= \frac{1}{2Tp_k^2}\mathrm{Re}\left(\begin{bmatrix} \bar{\mathbf{d}}_{\theta_k}^H \mathbf{P}_{\bar{\mathbf{g}}_k}^\perp \bar{\mathbf{d}}_{\theta_k} & \bar{\mathbf{d}}_{\theta_k}^H \mathbf{P}_{\bar{\mathbf{g}}_k}^\perp \bar{\mathbf{d}}_{\phi_k} \\ \bar{\mathbf{d}}_{\theta_k}^H \mathbf{P}_{\bar{\mathbf{g}}_k}^\perp \bar{\mathbf{d}}_{\phi_k} & \bar{\mathbf{d}}_{\phi_k}^H \mathbf{P}_{\bar{\mathbf{g}}_k}^\perp \bar{\mathbf{d}}_{\phi_k} \end{bmatrix}\right)^{-1} \mathbf{Q}_k^{\mathrm{BF}} \mathrm{Re}\left(\begin{bmatrix} \bar{\mathbf{d}}_{\theta_k}^H \mathbf{P}_{\bar{\mathbf{g}}_k}^\perp \bar{\mathbf{d}}_{\theta_k} & \bar{\mathbf{d}}_{\theta_k}^H \mathbf{P}_{\bar{\mathbf{g}}_k}^\perp \bar{\mathbf{d}}_{\phi_k} \\ \bar{\mathbf{d}}_{\theta_k}^H \mathbf{P}_{\bar{\mathbf{g}}_k}^\perp \bar{\mathbf{d}}_{\phi_k} & \bar{\mathbf{d}}_{\phi_k}^H \mathbf{P}_{\bar{\mathbf{g}}_k}^\perp \bar{\mathbf{d}}_{\phi_k} \end{bmatrix}\right)^{-1},$$

$$[\mathbf{Q}_k^{\mathrm{BF}}]_{11} = (p_k + \epsilon_g - 2\epsilon^2 p_k)\,\mathrm{Re}\left(\bar{\mathbf{d}}_{\theta_k}^H \mathbf{P}_{\bar{\mathbf{g}}_k}^\perp \bar{\mathbf{d}}_{\theta_k}\right) + \tilde{\mu}^2 \epsilon_g \mathrm{Re}\left(\bar{\mathbf{d}}_{\theta_k}^H \mathbf{P}_{\bar{\mathbf{g}}_k}^\perp \bar{\mathbf{d}}_{\theta_k}\right)$$

$$+ p_k^2 \epsilon^2 \left(1 - \epsilon^2\right)\mathrm{Re}\left(\bar{\mathbf{d}}_{\theta_k}^H \mathbf{P}_{\bar{\mathbf{g}}_k}^\perp \mathbf{W}^{-\frac{1}{2}}\mathbf{T}\mathbf{T}^H \mathbf{W}^{-\frac{1}{2}} \mathbf{P}_{\bar{\mathbf{g}}_k}^\perp \bar{\mathbf{d}}_{\theta_k}\right)$$

$$[\mathbf{Q}_k^{\mathrm{BF}}]_{12} = (p_k + \epsilon_g - 2\epsilon^2 p_k)\,\mathrm{Re}\left(\bar{\mathbf{d}}_{\phi_k}^H \mathbf{P}_{\bar{\mathbf{g}}_k}^\perp \bar{\mathbf{d}}_{\theta_k}\right) + \tilde{\mu}^2 \epsilon_g \mathrm{Re}\left(\bar{\mathbf{d}}_{\phi_k}^H \mathbf{P}_{\bar{\mathbf{g}}_k}^\perp \bar{\mathbf{d}}_{\theta_k}\right)$$

$$+ p_k^2 \epsilon^2 \left(1 - \epsilon^2\right)\mathrm{Re}\left(\bar{\mathbf{d}}_{\theta_k}^H \mathbf{P}_{\bar{\mathbf{g}}_k}^\perp \mathbf{W}^{-\frac{1}{2}}\mathbf{T}\mathbf{T}^H \mathbf{W}^{-\frac{1}{2}} \mathbf{P}_{\bar{\mathbf{g}}_k}^\perp \bar{\mathbf{d}}_{\phi_k}\right)$$

$$[\mathbf{Q}_k^{\mathrm{BF}}]_{22} = (p_k + \epsilon_g - 2\epsilon^2 p_k)\,\mathrm{Re}\left(\bar{\mathbf{d}}_{\phi_k}^H \mathbf{P}_{\bar{\mathbf{g}}_k}^\perp \bar{\mathbf{d}}_{\phi_k}\right) + \tilde{\mu}^2 \epsilon_g \mathrm{Re}\left(\bar{\mathbf{d}}_{\phi_k}^H \mathbf{P}_{\bar{\mathbf{g}}_k}^\perp \bar{\mathbf{d}}_{\phi_k}\right)$$

$$+ p_k^2 \epsilon^2 \left(1 - \epsilon^2\right)\mathrm{Re}\left(\bar{\mathbf{d}}_{\phi_k}^H \mathbf{P}_{\bar{\mathbf{g}}_k}^\perp \mathbf{W}^{-\frac{1}{2}}\mathbf{T}\mathbf{T}^H \mathbf{W}^{-\frac{1}{2}} \mathbf{P}_{\bar{\mathbf{g}}_k}^\perp \bar{\mathbf{d}}_{\phi_k}\right)$$

$$\epsilon_g = 1/\left(\bar{\mathbf{g}}_k^H \bar{\mathbf{g}}_k\right)$$

$$(6.27)$$

error is the finite sample effect, (6.27) can be simplified by taking the limit $\tilde{\mu} \to 0$ and $\tilde{\epsilon} \to 0$. In this case, the estimation errors reduce to the well-known expressions [146]

$$\mathbb{E}\left[(\hat{\theta}_k - \theta_k)^2\right] = \frac{1/\left(2Tp_k\right)}{\bar{\mathbf{d}}_{\theta_k}^H \mathbf{P}_{\bar{\mathbf{g}}_k}^\perp \bar{\mathbf{d}}_{\theta_k} - \left(\mathrm{Re}\left(\bar{\mathbf{d}}_{\theta_k}^H \mathbf{P}_{\bar{\mathbf{g}}_k}^\perp \bar{\mathbf{d}}_{\phi_k}\right)\right)^2 / \left(\bar{\mathbf{d}}_{\phi_k}^H \mathbf{P}_{\bar{\mathbf{g}}_k}^\perp \bar{\mathbf{d}}_{\phi_k}\right)}$$

$$\mathbb{E}\left[(\hat{\phi}_k - \phi_k)^2\right] = \frac{1/(2Tp_k)}{\bar{\mathbf{d}}_{\phi_k}^H \mathbf{P}_{\bar{\mathbf{g}}_k}^\perp \bar{\mathbf{d}}_{\phi_k} - \left(\mathrm{Re}\left(\bar{\mathbf{d}}_{\theta_k}^H \mathbf{P}_{\bar{\mathbf{g}}_k}^\perp \bar{\mathbf{d}}_{\phi_k}\right)\right)^2 / \left(\bar{\mathbf{d}}_{\theta_k}^H \mathbf{P}_{\bar{\mathbf{g}}_k}^\perp \bar{\mathbf{d}}_{\theta_k}\right)}.$$

$$(6.28)$$

6.2.2 MUSIC Estimation

In order to perform a similar expression for the estimation error for the MUSIC algorithm, we make use of the relationship between $\mathbf{E}_s$ and $\bar{\mathbf{G}}$. There exists a full rank matrix $\mathbf{B}$ such that

$$\mathbf{B} = \bar{\mathbf{G}}^\dagger \mathbf{E}_s.$$

$$\mathbb{E}\left[\begin{pmatrix} \hat{\theta}_k - \theta_k \\ \hat{\phi}_k - \phi_k \end{pmatrix} \begin{pmatrix} \hat{\theta}_k - \theta_k \\ \hat{\phi}_k - \phi_k \end{pmatrix}^T \right]$$

$$= \frac{1}{2T}\mathrm{Re}\left(\begin{bmatrix} \bar{\mathbf{d}}_{\theta_k}^H \mathbf{P}_{\bar{\mathbf{G}}}^\perp \bar{\mathbf{d}}_{\theta_k} & \bar{\mathbf{d}}_{\theta_k}^H \mathbf{P}_{\bar{\mathbf{G}}}^\perp \bar{\mathbf{d}}_{\phi_k} \\ \bar{\mathbf{d}}_{\theta_k}^H \mathbf{P}_{\bar{\mathbf{G}}}^\perp \bar{\mathbf{d}}_{\phi_k} & \bar{\mathbf{d}}_{\phi_k}^H \mathbf{P}_{\bar{\mathbf{G}}}^\perp \bar{\mathbf{d}}_{\phi_k} \end{bmatrix}\right)^{-1} \mathbf{Q}_k^{\mathrm{MU}} \mathrm{Re}\left(\begin{bmatrix} \bar{\mathbf{d}}_{\theta_k}^H \mathbf{P}_{\bar{\mathbf{G}}}^\perp \bar{\mathbf{d}}_{\theta_k} & \bar{\mathbf{d}}_{\theta_k}^H \mathbf{P}_{\bar{\mathbf{G}}}^\perp \bar{\mathbf{d}}_{\phi_k} \\ \bar{\mathbf{d}}_{\theta_k}^H \mathbf{P}_{\bar{\mathbf{G}}}^\perp \bar{\mathbf{d}}_{\phi_k} & \bar{\mathbf{d}}_{\phi_k}^H \mathbf{P}_{\bar{\mathbf{G}}}^\perp \bar{\mathbf{d}}_{\phi_k} \end{bmatrix}\right)^{-1}$$

$$[\mathbf{Q}_k^{\mathrm{MU}}]_{11} = (1-\epsilon^2)\mathrm{Re}\left(\bar{\mathbf{d}}_{\theta_k}^H \mathbf{P}_{\bar{\mathbf{g}}_k}^\perp \bar{\mathbf{d}}_{\theta_k} \mathbf{b}_k^H \tilde{\mathbf{\Lambda}}^{-1} \mathbf{\Lambda}_s \tilde{\mathbf{\Lambda}}^{-1} \mathbf{b}_k\right) + \tilde{\mu}^2 \mathrm{Re}\left(\bar{\mathbf{d}}_{\theta_k}^H \mathbf{P}_{\bar{\mathbf{g}}_k}^\perp \bar{\mathbf{d}}_{\theta_k} \mathbf{b}_k^H \tilde{\mathbf{\Lambda}}^{-2} \mathbf{b}_k\right)$$
$$+ \epsilon^2\left(1-\epsilon^2\right) \mathrm{Re}\left(\bar{\mathbf{d}}_{\theta_k}^H \mathbf{P}_{\bar{\mathbf{g}}_k}^\perp \mathbf{W}^{-\frac{1}{2}} \mathbf{T}\mathbf{T}^H \mathbf{W}^{-\frac{1}{2}} \mathbf{P}_{\bar{\mathbf{g}}_k}^\perp \bar{\mathbf{d}}_{\theta_k} \mathbf{b}_k^H \tilde{\mathbf{\Lambda}}^{-1} \mathbf{\Lambda}_s \mathbf{B}^H \mathbf{B}\mathbf{\Lambda}_s \tilde{\mathbf{\Lambda}}^{-1} \mathbf{b}_k\right) \quad (6.30)$$

$$[\mathbf{Q}_k^{\mathrm{MU}}]_{12} = (1-\epsilon^2)\mathrm{Re}\left(\bar{\mathbf{d}}_{\theta_k}^H \mathbf{P}_{\bar{\mathbf{g}}_k}^\perp \bar{\mathbf{d}}_{\phi_k} \mathbf{b}_k^H \tilde{\mathbf{\Lambda}}^{-1} \mathbf{\Lambda}_s \tilde{\mathbf{\Lambda}}^{-1} \mathbf{b}_k\right) + \tilde{\mu}^2 \mathrm{Re}\left(\bar{\mathbf{d}}_{\theta_k}^H \mathbf{P}_{\bar{\mathbf{g}}_k}^\perp \bar{\mathbf{d}}_{\phi_k} \mathbf{b}_k^H \tilde{\mathbf{\Lambda}}^{-2} \mathbf{b}_k\right)$$
$$+ \epsilon^2\left(1-\epsilon^2\right) \mathrm{Re}\left(\bar{\mathbf{d}}_{\theta_k}^H \mathbf{P}_{\bar{\mathbf{g}}_k}^\perp \mathbf{W}^{-\frac{1}{2}} \mathbf{T}\mathbf{T}^H \mathbf{W}^{-\frac{1}{2}} \mathbf{P}_{\bar{\mathbf{g}}_k}^\perp \bar{\mathbf{d}}_{\phi_k} \mathbf{b}_k^H \tilde{\mathbf{\Lambda}}^{-1} \mathbf{\Lambda}_s \mathbf{B}^H \mathbf{B}\mathbf{\Lambda}_s \tilde{\mathbf{\Lambda}}^{-1} \mathbf{b}_k\right)$$

$$[\mathbf{Q}_k^{\mathrm{MU}}]_{22} = (1-\epsilon^2)\mathrm{Re}\left(\bar{\mathbf{d}}_{\phi_k}^H \mathbf{P}_{\bar{\mathbf{g}}_k}^\perp \bar{\mathbf{d}}_{\phi_k} \mathbf{b}_k^H \tilde{\mathbf{\Lambda}}^{-1} \mathbf{\Lambda}_s \tilde{\mathbf{\Lambda}}^{-1} \mathbf{b}_k\right) + \tilde{\mu}^2 \mathrm{Re}\left(\bar{\mathbf{d}}_{\phi_k}^H \mathbf{P}_{\bar{\mathbf{g}}_k}^\perp \bar{\mathbf{d}}_{\phi_k} \mathbf{b}_k^H \tilde{\mathbf{\Lambda}}^{-2} \mathbf{b}_k\right)$$
$$+ \epsilon^2\left(1-\epsilon^2\right) \mathrm{Re}\left(\bar{\mathbf{d}}_{\phi_k}^H \mathbf{P}_{\bar{\mathbf{g}}_k}^\perp \mathbf{W}^{-\frac{1}{2}} \mathbf{T}\mathbf{T}^H \mathbf{W}^{-\frac{1}{2}} \mathbf{P}_{\bar{\mathbf{g}}_k}^\perp \bar{\mathbf{d}}_{\phi_k} \mathbf{b}_k^H \tilde{\mathbf{\Lambda}}^{-1} \mathbf{\Lambda}_s \mathbf{B}^H \mathbf{B}\mathbf{\Lambda}_s \tilde{\mathbf{\Lambda}}^{-1} \mathbf{b}_k\right)$$

Defining $\tilde{\mathbf{\Lambda}}$ to be the diagonal matrix given by

$$\tilde{\mathbf{\Lambda}} = \mathbf{\Lambda}_s - \mathbf{I}_{MN},$$

we also have [117]

$$\mathbf{C}_s = \bar{\mathbf{G}}^\dagger \mathbf{E}_s \tilde{\mathbf{\Lambda}} \mathbf{E}_s^H \left(\bar{\mathbf{G}}^\dagger\right)^H = \mathbf{B}\tilde{\mathbf{\Lambda}}\mathbf{B}^H. \tag{6.29}$$

Theorem 2: Let $\hat{\theta}_k^{\mathrm{MU}}$ and $\hat{\phi}_k^{\mathrm{MU}}$ be the k-th user DOAs estimated from (6.18). Assuming that the assumptions in section 6.1.1 hold, the asymptotic second-order statistics of the estimation errors is given by (6.30) at the top of the next page.

Proof: See Appendix F. ∎

Again, when the array perturbation and noise modeling errors are small, we can take the

limit $\tilde{\mu} \to 0$ and $\tilde{\epsilon} \to 0$ in (6.30) to get

$$
\begin{aligned}
\mathbb{E}\left[(\hat{\theta}_k - \theta_k)^2\right] &= \frac{\left([\mathbf{C}_s]_{kk}^{-1} + [\mathbf{C}_s]_{kk}^{-2}/(\bar{\mathbf{g}}_k^H \bar{\mathbf{g}}_k)\right)/(2T)}{\bar{\mathbf{d}}_{\theta_k}^H \mathbf{P}_{\bar{\mathbf{G}}}^{\perp} \bar{\mathbf{d}}_{\theta_k} - \left(\operatorname{Re}\left(\bar{\mathbf{d}}_{\theta_k}^H \mathbf{P}_{\bar{\mathbf{G}}}^{\perp} \bar{\mathbf{d}}_{\phi_k}\right)\right)^2/\left(\bar{\mathbf{d}}_{\phi_k}^H \mathbf{P}_{\bar{\mathbf{G}}}^{\perp} \bar{\mathbf{d}}_{\phi_k}\right)} \\
\mathbb{E}\left[(\hat{\phi}_k - \phi_k)^2\right] &= \frac{\left([\mathbf{C}_s]_{kk}^{-1} + [\mathbf{C}_s]_{kk}^{-2}/(\bar{\mathbf{g}}_k^H \bar{\mathbf{g}}_k)\right)/(2T)}{\bar{\mathbf{d}}_{\phi_k}^H \mathbf{P}_{\bar{\mathbf{G}}}^{\perp} \bar{\mathbf{d}}_{\phi_k} - \left(\operatorname{Re}\left(\bar{\mathbf{d}}_{\theta_k}^H \mathbf{P}_{\bar{\mathbf{G}}}^{\perp} \bar{\mathbf{d}}_{\phi_k}\right)\right)^2/\left(\bar{\mathbf{d}}_{\theta_k}^H \mathbf{P}_{\bar{\mathbf{G}}}^{\perp} \bar{\mathbf{d}}_{\theta_k}\right)}.
\end{aligned}
\tag{6.31}
$$

Comparing (6.31) and (6.28), we see that the estimation errors of the beamformer and MUSIC estimators coincide when the array is large and the source covariance matrix is diagonal. However, by considering suitable weighted versions of the algorithm, MUSIC has been shown to have a lower variance when the array errors are non-uniform from antenna to antenna [116, 117].

6.2.3   Impact of Array Perturbations

With the substitution $\tilde{\epsilon}^2 = T\epsilon^2$ and $\tilde{\mu}^2 = T\mu^2$, the estimation error does not go to zero even when $T \to \infty$ and the covariance matrix converges to an expression for model errors only. We will additionally set $\mu = 0$ and $K = 1$, and consider an SNR sufficiently high enough to study only the impact of array perturbations on the estimation performance for a single user. Under these assumptions, we have that

$$
\begin{aligned}
\tilde{\boldsymbol{\Lambda}} &\approx \boldsymbol{\Lambda}_s \\
\mathbf{b}_k = \mathbf{B} &= \frac{1}{\|\bar{\mathbf{g}}\|^2},
\end{aligned}
\tag{6.32}
$$

and the MUSIC estimation error covariance matrix in (6.30) can be simplified to

$$
\mathbb{E}\left[\begin{pmatrix} \hat{\theta}-\theta \\ \hat{\phi}-\phi \end{pmatrix}\begin{pmatrix} \hat{\theta}-\theta \\ \hat{\phi}-\phi \end{pmatrix}^T\right] = \frac{\epsilon^2\left(1-\epsilon^2\right)}{2T}\mathrm{Re}\left(\begin{bmatrix} \bar{\mathbf{d}}_{\theta_k}^H\mathbf{P}_{\bar{\mathbf{G}}}^{\perp}\bar{\mathbf{d}}_{\theta_k} & \bar{\mathbf{d}}_{\theta_k}^H\mathbf{P}_{\bar{\mathbf{G}}}^{\perp}\bar{\mathbf{d}}_{\phi_k} \\ \\ \bar{\mathbf{d}}_{\theta_k}^H\mathbf{P}_{\bar{\mathbf{G}}}^{\perp}\bar{\mathbf{d}}_{\phi_k} & \bar{\mathbf{d}}_{\phi_k}^H\mathbf{P}_{\bar{\mathbf{G}}}^{\perp}\bar{\mathbf{d}}_{\phi_k} \end{bmatrix}\right)^{-1}
$$
$$
\begin{bmatrix} \|\mathbf{T}^H\mathbf{W}^{-\frac{1}{2}}\mathbf{P}_{\bar{\mathbf{g}}_k}^{\perp}\bar{\mathbf{d}}_{\theta_k}\|^2 & \mathrm{Re}\begin{pmatrix} \bar{\mathbf{d}}_{\theta_k}^H\mathbf{P}_{\bar{\mathbf{g}}_k}^{\perp}\mathbf{W}^{-\frac{1}{2}}\mathbf{T} \\ \mathbf{T}^H\mathbf{W}^{-\frac{1}{2}}\mathbf{P}_{\bar{\mathbf{g}}_k}^{\perp}\bar{\mathbf{d}}_{\phi_k} \end{pmatrix} \\ \\ \mathrm{Re}\begin{pmatrix} \bar{\mathbf{d}}_{\theta_k}^H\mathbf{P}_{\bar{\mathbf{g}}_k}^{\perp}\mathbf{W}^{-\frac{1}{2}}\mathbf{T} \\ \mathbf{T}^H\mathbf{W}^{-\frac{1}{2}}\mathbf{P}_{\bar{\mathbf{g}}_k}^{\perp}\bar{\mathbf{d}}_{\phi_k} \end{pmatrix} & \|\mathbf{T}^H\mathbf{W}^{-\frac{1}{2}}\mathbf{P}_{\bar{\mathbf{g}}_k}^{\perp}\bar{\mathbf{d}}_{\phi_k}\|^2 \end{bmatrix} \mathrm{Re}\left(\begin{bmatrix} \bar{\mathbf{d}}_{\theta_k}^H\mathbf{P}_{\bar{\mathbf{G}}}^{\perp}\bar{\mathbf{d}}_{\theta_k} & \bar{\mathbf{d}}_{\theta_k}^H\mathbf{P}_{\bar{\mathbf{G}}}^{\perp}\bar{\mathbf{d}}_{\phi_k} \\ \\ \bar{\mathbf{d}}_{\theta_k}^H\mathbf{P}_{\bar{\mathbf{G}}}^{\perp}\bar{\mathbf{d}}_{\phi_k} & \bar{\mathbf{d}}_{\phi_k}^H\mathbf{P}_{\bar{\mathbf{G}}}^{\perp}\bar{\mathbf{d}}_{\phi_k} \end{bmatrix}\right)^{-1}.
$$

$$(6.33)$$

Note that even though it was assumed in Sec. 6.1.2 that the covariance matrix of $\tilde{\mathbf{A}}$ is a scaled identity matrix, the effective covariance matrix of array perturbations at the prewhitened output is $\mathbf{W}^{-\frac{1}{2}}\mathbf{T}\mathbf{T}^H\mathbf{W}^{-\frac{1}{2}}$. The expressions in (6.33) are particularly difficult to compute analytically due to the presence of the MCM $\mathbf{T}$ and the prewhitening matrix $\mathbf{W}^{-\frac{1}{2}}$. Hence, we will consider the impact of severe array calibrations in the Sec. 6.3 where (6.33) is computed empirically.

6.2.4   Asymptotic Analysis - ULAs

The estimation of either the elevation or the azimuth angles using a one-dimensional array can be treated as a special case of the two-dimensional DOA estimation and the variance of the 1D beamformer can be derived in a straightforward manner from (6.27). Due to the interdependence of the parameters θ_k and ϕ_k in the expressions for the estimation error variances, it is difficult to characterize the behavior of the estimator and study the effect of

system parameters on the performance. The analysis is further complicated by the presence of mutual coupling and modeling errors. In this section, we consider an N-element ULA equipped with $\Sigma\Delta$ ADCs and derive an expression for the estimation error of θ_k. For simplicity, we will assume that the mutual coupling between antennas is insignificant, $K = 1$, and that there are no modeling errors.

We begin by using the result from [103] that in the limit of a large number of antennas, the quantization noise power converges to a constant value given by

$$
\sigma_q^2 = \sigma_x^2 \frac{k'-2}{4-k'}
$$

$$
k' = \begin{cases} \pi\beta^2, \ b = 1 \\ \alpha^2 \sum_{i=1}^4 \nu_i^2 \left(\Psi\left(\frac{\sigma_r}{\sqrt{2}}\nu_i^{\text{hi}}\right) - \Psi\left(\frac{\sigma_r}{\sqrt{2}}\nu_i^{\text{lo}}\right) \right), \ b = 2. \end{cases} \tag{6.34}
$$

We will assume that the $\Sigma\Delta$ ADC array is steered to the broadside direction ($\psi = 0$), although the extension to an arbitray ψ is straightforward. Thus, $\mathbf{T} = \mathbf{I}_N$, $\mathbf{C}_n = \mathbf{I}$ and $\mathbf{W} = \mathbf{I} + \sigma_q^2 \mathbf{U}^{-1}\mathbf{U}^{-H}$. Then, (6.28) reduces to

$$
\mathbb{E}\left[\hat{\theta} - \theta\right]^2 = \frac{1/\rho}{2T\left(\bar{\mathbf{d}}_\theta^H \mathbf{P}_{\bar{\mathbf{g}}}^\perp \bar{\mathbf{d}}_\theta\right)}, \tag{6.35}
$$

where ρ is the transmit power of the user. In a similar manner, it can be shown that (6.31) also converges to the expression in (6.35). Then, observing that $\mathbf{W}$ is a symmteric tridiagonal Topelitz matrix, we compute the inverse of this matrix. While the inverse of a symmetric Toeplitz matrix can be evaluated in closed-form, is not Toeplitz in general (it is centrosymmetric). However, the differences between the elements along any of the diagonals are small enough to be ignored and the inverse can be approximated by a Toeplitz matrix. The inverse of the tridiagonal matrix is obtained by following the method in [147] and is given by

$$
\left[\mathbf{W}^{-1}\right]_{nm} = \frac{1}{\lambda_q^2(1+2\sigma_q^2)} l_q^{|m-n|} \tag{6.36}
$$

where

$$l_q = \frac{\sigma_q^2}{(1 + 2\sigma_q^2)}$$

$$\lambda_q = \left(1 + \sqrt{1 + 4\sigma_q^2/(1 + 2\sigma_q^2)}\right)/2. \tag{6.37}$$

The variance of the estimator can be computed by evaluating the individual terms in (6.35) and is given by

$$\mathbb{E}\left[\hat{\theta} - \theta\right]^2 = \frac{\lambda_q^2(1 + 2\sigma_q^2)\left(1 - 2l_q\cos\left(\frac{2\pi d\sin\theta}{\lambda}\right) + l_q^2\right)}{\rho\frac{N^3 T}{6}\left(2\pi\frac{d}{\lambda}\cos\theta\right)^2\left(1 - l_q^2\right)}.. \tag{6.38}$$

The derivation of the above expression is shown in Appendix G. A similar analysis is performed for standard low resolution quantization and ideal resolution ADCs in Appendix H and the resulting variance of the beamformer estimator applied to these ADC arrays is given by Eqs. (H.3) and (H.4), respectively. Inspection of Eqs. (6.38), (H.3) and (H.4) reveals that in each case, the estimation error decreases inversely with N^3 and inversely with the square of the cosine of the true DOA. In both of the low resolution schemes, the estimation error is affected by the particular value of the quantization noise power. We can make an additional observation regarding the numerator term in (6.38). Increasing θ causes $\cos(2\pi d\sin\theta/\lambda)$ to decrease and the numerator to increase overall. The net effect of increasing θ is that the numerator increases while the denominator decreases simultaneously, and the estimator variance increases at a higher rate compared to standard quantization schemes.

The high SNR estimation error floor can be computed from (6.38) by setting $\sigma_x^2 = \rho$ and taking the limit $\rho \to \infty$. Let $k'' = \frac{k'-2}{4-k'}$. Then, from (6.34), $\sigma_q^2 = \rho k''$ and the limiting values of λ_q and l_q are both computed to be equal to $1/2$. Then, the estimation error in the high

SNR limit is

$$\lim_{\rho \to \infty} \mathbb{E}\left[\hat{\theta} - \theta\right]^2 = \frac{k''\left(\frac{5}{4} - \cos\left(\frac{2\pi d\sin\theta}{\lambda}\right)\right)}{T\left(\frac{\pi d\cos\theta}{\lambda}\right)^2 N^3}\left(1 + \frac{\frac{2}{3}k''\left(\frac{5}{4} - \cos\left(\frac{2\pi d\sin\theta}{\lambda}\right)\right)}{N}\right). \tag{6.39}$$

Similarly, the estimation error for standard quantization with $\rho \to \infty$ is computed in Appendix H. Following a similar reasoning as above, it can be shown that the error floor is lower than that obtained with standard low resolution ADCs when $\theta \to 0°$ and higher when $\theta \to 90°$.

6.3 Simulation Results

In this section, we evaluate the RMSE performance of the DOA estimators with the $\Sigma\Delta$ quantized output and compare it with that of an ADC array of infinite resolution. The effect of array and noise covariance perturbation on the RMS performance is evaluated and the sample RMSE of the estimates is compared to the corresponding theoretical expressions. The parameters used in modeling the MCM are selected as follows: $R = 50\Omega$, $T_A = 290K$, $\varrho_n = -0.35 + j0.7$, $B = 20MHz$, $R_N = R$, and $\sigma_i^2 = 2k_B T_A B/R$. For the simulations performed in the absence of mutual coupling, we assume that $\mathbf{Z} = R\mathbf{I}$ and $\mathbf{T} = 0.5\mathbf{I}$ [113]. In computing the quantization noise matrix for prewhitening, the value of β selected for one-bit $\Sigma\Delta$ quantization is 1.05, and unless otherwise specified, the parameter ψ is selected to steer the array to the mean of the elevation angular sector spanned by the users. For two-bit ADCs, the optimum levels $\{\nu_1, \nu_2, \nu_3, \nu_4\}$ are chosen as per [119]. The simulations are conducted for a 30×30 planar array with $K = 7$ users. The elevation angles are uniformly distributed in the range $[-10°, 10°]$ and the azimuth angles are uniformly distributed in the range $[-45°, 45°]$. The inter-element spacings of the rectangular array along the z- and $y-$

axes are $\lambda/6$ and $\lambda/2$, respectively.

We use an iterative Newton method for optimizing the different criteria. Since we are interested in the asymptotic estimation error, the algorithms are initialized at the true values of $\boldsymbol{\theta}$ and $\boldsymbol{\phi}$. The source symbols are drawn randomly from a circularly symmetric Gaussian random process with $\mathbf{C}_s = \rho\mathbf{I}_K$. Then, the average SNR per-user is defined as

$$\text{SNR} = \frac{\rho\text{Tr}\left(\mathbf{TA}\left(\boldsymbol{\theta}, \boldsymbol{\phi}\right)\mathbf{A}^H\left(\boldsymbol{\theta}, \boldsymbol{\phi}\right)\mathbf{T}^H\right)}{\text{Tr}\left(\mathbf{C}_n\right)}. \tag{6.40}$$

We also compare with the RMSE obtained with standard low-resolution ADC arrays. For the standard one-bit ADC array, the vector-wise Bussgang decomposition in [27] is used to obtain the quantization noise covariance matrix, while for the two-bit case, an element-wise Bussgang decomposition is used in a manner similar to that described in [148]. We note that an asymptotic analysis of neither the MUSIC algorithm nor the conventional beamformer with regular ADCs exists in prior literature and although a direct application of equations (6.27) and (6.30) is possible, they do not yield accurate analytical results for the rectangular array. For this reason, we exclude theoretical results for standard one and two-bit ADC arrays.

In all simulations, solid lines and ◁, respectively, indicate the simulation error and theoretical values predicted by (6.27) obtained with the MUSIC algorithm, while dash-dotted lines and circles, respectively, indicate the simulation error and theoretical values predicted by (6.30) with the Bartlett beamformer.

In Fig. 6.2, we plot the RMSE of the estimated DOAs as a function of the SNR with the perturbation variances $\epsilon = 0.01$ and $\mu = 10^{-4}$. It can be seen that there is good agreement between the simulated and analytical RMSE values. in the estimation of both $\boldsymbol{\theta}$ and $\boldsymbol{\phi}$, the RMSEs achieved with the estimators based on $\Sigma\Delta$ ADC outputs are nearly identical
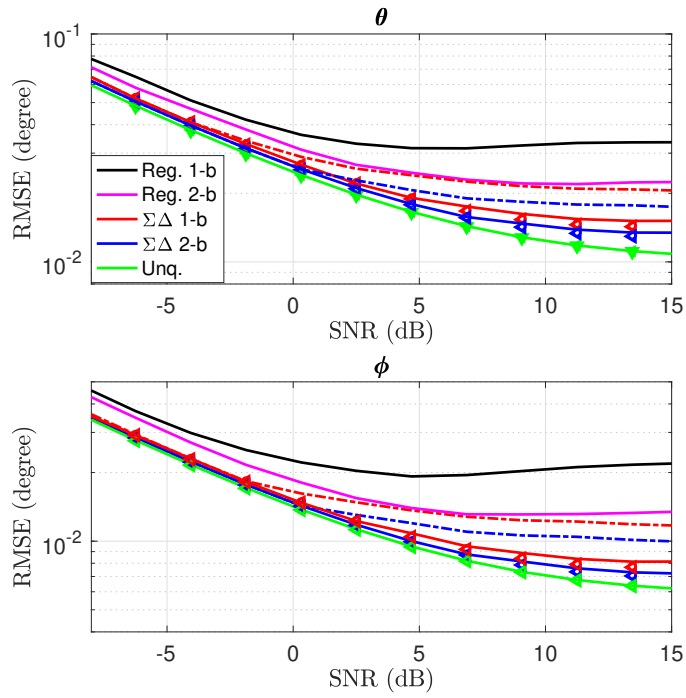
Figure 6.2: RMSE as a function of the SNR for a 30×30 planar array with $\epsilon = 0.01$ and $\mu = 10^{-4}$.
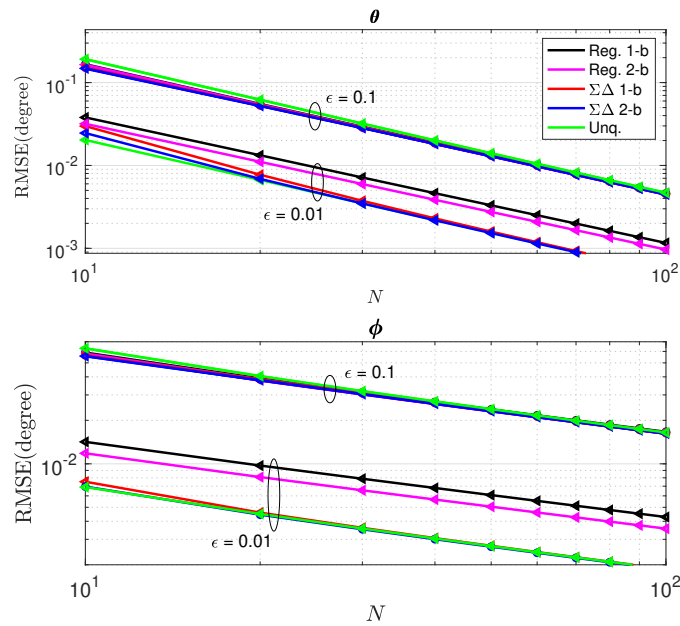
Figure 6.3: RMSE as a function of N for $\epsilon = 0.1$ and $\epsilon = 0.01$.
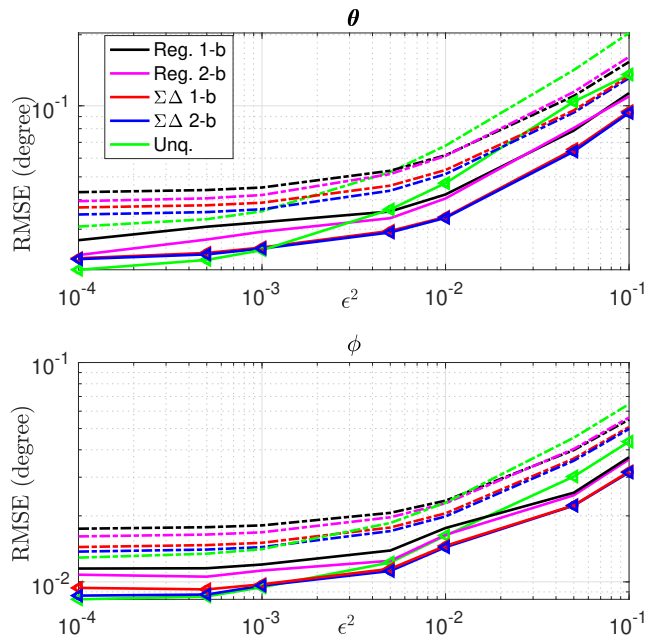
Figure 6.4: RMSE as a function of perturbation variance ϵ^2 for an SNR of 0dB.

to that obtained from infinite (ideal) resolution ADC outputs at low to moderate SNRs. At high SNRs, the gap between the RMSEs of $\Sigma\Delta$ and ideal ADCs is quite small- of the order of $0.01°$ or less in case of the estimation of $\boldsymbol{\theta}$ and of the order of $0.001°$ or less in case of the estimation of $\boldsymbol{\phi}$. On the other hand, the gap between the RMSEs of standard and ideal ADCs is slightly higher- around $0.02°$ or less in case of the estimation of $\boldsymbol{\theta}$ and of the order of $0.01°$ or less in case of the estimation of $\boldsymbol{\phi}$. The analytical values predicted for the MUSIC algorithm and the beamformer are identical. Although there is a mismatch between the simulated and theoretical RMSEs achieved with the beamformer, the gap between them is around a hundredths of a degree.

In Fig. 6.3, the impact of array calibration error is studied by plotting the elevation and azimuth estimation errors predicted by (6.33) for two levels of array calibration errors: $\epsilon = 0.1$ and $\epsilon = 0.01$. A single user is assumed to be located at $[10°, 25°]$ and $\psi = 10°$, the SNR is 10dB, $M = 10$ antennas and N is varied from 10 to 100, although similar results are obtained when N is fixed and M is varied. For $\epsilon = 0.01$, it is seen that the performance of estimation
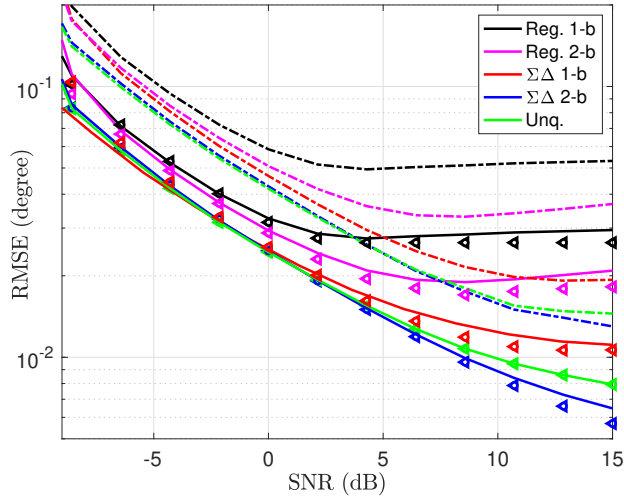
Figure 6.5: RMSE of DOA estimation for a ULA with 100 antennas.

errors achieved with $\Sigma\Delta$ ADCs is close to that achieved with ideal resolution ADCs whereas the regular quantizer arrays have a visibly worse performance. For $\epsilon = 0.1$, however, both $\Sigma\Delta$ and standard ADCs have a lower estimation error compared to ideal ADCs for small values of N. This is similar to the observation by the authors in [149] where it was noted that one-bit quantizers are less affected by antenna gain sensors than ideal ADCs.

In Fig. 6.4, we ignore the effect of noise modeling errors and illustrate the RMSE for an SNR of 0dB as a function of the array modeling error variance ϵ alone. As ϵ is increased, the estimation performance for all methods progressively worsen. Somewhat surprisingly, at high values of ϵ, estimators employing any of the low-resolution quantizers perform better than one employing ideal resolution ADCs. This is also validated by analytical RMSE values. Thus at high levels of perturbation variance when the array steering vectors are imperfectly known, low-resolution ADCs are preferable to the use of expensive high-precision ADCs.

In the rest of the simulations, we perform experiments on ULAs with the interelement spacing equal to 1/6. The 5 users are uniformly distributed between $[-10°, 10°]$. In Fig. (6.5), we plot the RMSE on a 100-element ULA when the array perturbation variance ϵ is equal to 0.03 and assume that there are no noise modeling errors. As before, the experimental
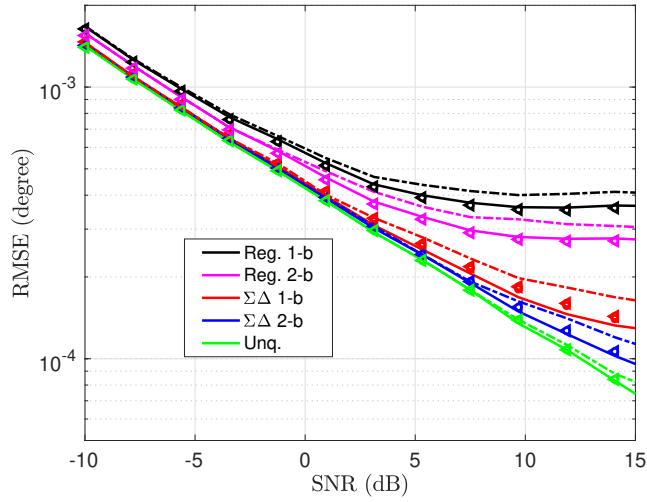
Figure 6.6: RMSE for a ULA with 1000 antennas.
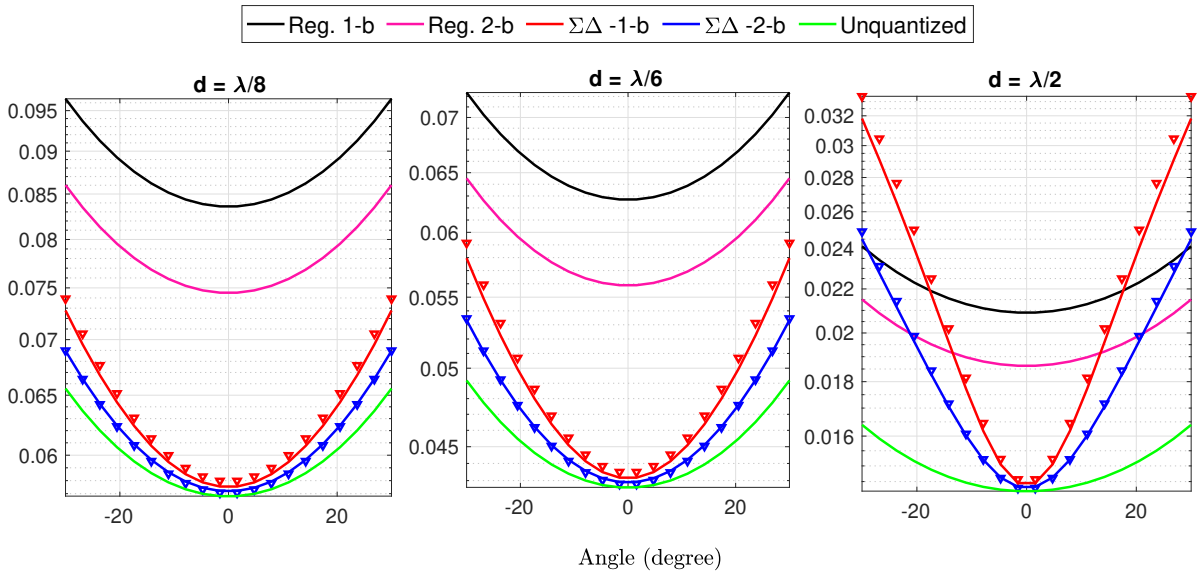
Figure 6.7: RMSE as a function of the DOA for different inter-element antenna spacings.

RMSEs agree with the analytical values. DOA estimators employing $\Sigma\Delta$ ADCs perform significantly better than those employing standard low-resolution ADCs. At high SNRs, the $\Sigma\Delta$ array equipped with two-bit ADCs has a performance nearly identical to that achieved with infinite precision ADCs. The worse performance of the Bartlett beamformer can be

126

attributed to the inherent problem of the beamformer with the resolution of closely spaced sources. However, this difference can be considerably alleviated by increasing the number of antennas as shown in Fig. 6.6. In Fig. 6.6, we plot the RMSE for a 1000-element ULA and assume that the array modeling errors are also negligible. The asymptotic equivalence of MUSIC and the beamformer is evident and the difference between the two estimators is small, less than 1/1000th of a degree.

Finally, in Fig. 6.7, we study the RMSE performance for various interelement spacings as a function of the DOA, θ, in the absence of mutual coupling and modeling errors. For the $\Sigma\Delta$ plots, inverted triangles indicate values predicted by (6.38). The analytical value is evaluated directly from (6.35) in addition to the approximation from (6.38) for the $\Sigma\Delta$ case. It is seen that for closer antenna spacings, the $\Sigma\Delta$ ADC array with both one and two-bit resolutions have a lower estimation error than their corresponding standard quantization counterparts. However, the range of angles over which $\Sigma\Delta$ ADC arrays have an advantage decreases upon increasing the antenna spacing. For instance, for $d/\lambda = 1/2$, DOA estimation with $\Sigma\Delta$ ADCs has a better performance than that with standard ADCs over the angular sectors $[-18°, 18°]$ and $[-20°, 20°]$ for $b = 1$ and $b = 2$ respectively. On the other hand, for $d/\lambda = 1/6$, the widths of these sectors are more than $60°$. Additionally, there is good agreement between the theoretical prediction obtained from our analysis given by (6.38) and that obtained from (6.35). The noise shaping effect of $\Sigma\Delta$ ADCs also means that the estimation of user DOAs lying outside of the sector centered at the array broadside suffers due to lower SQNR in these regions. This can be alleviated by a judicious choice of ψ but this would require prior knowledge of the sectors in which the users are located. One solution is to use adaptive beamformers as in [109], although this would entail a delay in estimation and an increase in estimation complexity.

Chapter 7

Concluding Remarks

In this dissertation, the performance of massive MIMO systems equipped with oversampled low-resolution ADCs was considered. In this chapter, the salient findings are summarized and directions for future work are provided.

7.1 Conclusion

The first part considered mmWave massive MIMO systems equipped with one-bit ADCs that are temporally oversampled. In Chapter 3, CRB performance bounds for channel estimation were derived for three different channel models: a structured mmWave channel characterized by path loss coefficients and DOAs of the sparse channel, an unstructured channel appropriate when the number of paths is large, and a dictionary based channel where this are grid errors. A system model with array calibration errors was also considered. The results showed that even when the precise array calibration is unknown, using a structured channel model can result in a lower channel estimation error. Increasing the bandwidth and the oversampling factor can reduce the estimation error variance. Temporal oversampling ex-

ploits the correlation between adjacent samples of the input and reduce the loss beyond the $2/\pi$ limit. However, temporal oversampling exacerbates the data rate requirements on the remote radio head (RRH).

Alternatively, spatial oversampling could be used. In Chapters 4-6, the effect of one- and two-bit spatial $\Sigma\Delta$ ADCs on the system performance was analyzed. Equivalent linear models were used to develop a channel estimator in Chapter 4 and the resulting impact on the spectral efficiency efficiency was studied. In Chapter 5, spatial $\Sigma\Delta$ modulation was used to estimate the azimuth and elevation angles of signals impinging on a rectangular array. Closed form analytical results were derived for the channel estimation error and the DOA estimation error. In both cases, the simulation results show superior performance of $\Sigma\Delta$ ADCs compared to conventional ADCs when the desired signals arrive from a sector narrow relative to the array broadside, or equivalently, from low spatial frequencies. Estimation errors close to that achieved with ideal precision ADCs can be achieved with a nominal increase in hardware complexity and cost compared to conventional ADCs.

7.2   Suggestions for Future Work

The research for this dissertation has generated a number of possible areas for future work. Some possible directions for extending the solutions presented in this dissertation are listed below.

In Chapter 3, the CRB, a measure that is relatively easy to compute for most problems, was used to analyze the performance of mmWave channel estimation. Deriving a dedicated channel estimator for each channel model considered was beyond the scope of this dissertation. Nevertheless, it will be interesting to see how close the performance of these estimators is to the CRB. Any unbiased channel estimator designed would only be able to approach the

CRB but not achieve it due the nonlinearity of the quantization operation and the nonlinear functions of the parameters to be estimated. Versions of the CRB and other tighter bounds that can be applied to biased estimators exist when the bias function can be determined. Since the CRB is closely related to the MSE that could be achieved, an additional direction that can be explored is in characterizing an upper bound on the capacity of the massive MIMO system with imperfect CSI without a particular channel estimator being specified.

Extending the CRB analysis for a system equipped with $\Sigma\Delta$ arrays considered in the second part of this dissertation does not appear to be straightforward. Computation of the FIM requires complete knowledge of the analytical form of the underlying distribution and its exact dependence on the parameters. For the $\Sigma\Delta$ output, the characterization of its pdf is particularly difficult and hence, the computation of the FIM is complicated. However, there are alternatives when the statistical model is unknown. One approach is to estimate the underlying pdf along with its gradient or Hessian. There are methods to estimate the non-parametric density by performing controlled experiments to generate data with tunable parameters. The FIM could then be computed by averaging the numerical gradients of the log-densities estimated from each of the perturbed experiments [150]. Alternatively, the FIM could be computed by generating an estimate of a divergence measure directly from the data [151]. This approach has been used for dimensionality reduction and characterization of the criticality behavior in neural networks [152, 153].

It is well-known that with conventional ADCs of resolution 4 bits or higher, a nearly ideal performance could be achieved. Chapters 5 and 6 have shown that an almost ideal performance could also be achieved with low-resolution $\Sigma\Delta$ ADCs. The additional hardware complexity of $\Sigma\Delta$ ADCs appears to be minimal, but the additional power consumption in the RF chain of each antenna is undeniable. A natural research problem would be a comparison of the associated trade-offs between the hardware complexity and power consumption for each class of ADC architecture. Future studies could accurately quantify the gains in

energy efficiency as well.

In the research on channel estimation and direction finding using spatial $\Sigma\Delta$ ADCs, the simulations were set up for scenarios where the users were constrained to relatively narrow angular sectors. If the users were to be distributed over a wider angular sector, for instance, the methods proposed in this dissertation would reasonably lead to higher estimation errors than conventional ADCs. However, with the handle provided by the steering angle could be used to divide the wider angular sector into several narrower angular sectors and an adaptive beamformer that sequentially scans these sectors could be designed. The resulting estimation error can be expected to be significantly lower than an approach that uses a fixed value of the steering angle since the $\Sigma\Delta$ array would outperform conventional ADCs in each of these narrower sectors. However, this beam-scanning approach would entail a larger processing delay since multiple measurements would have to be recorded for each of the scanned sectors. A more detailed study into the acceptable delays and algorithm complexity for different applications is necessary.

While the delay in the $\Sigma\Delta$ array for narrowband systems could be compensated for by choosing appropriate phase shifts between stages, care should be taken for the extension to the wideband/mmWave scenario due to the "beam squint" problem. In a mmWave system, the delay in $\Sigma\Delta$ processing is of the same order as the symbol duration and would have to be accounted for in a different manner. An additional interesting problem is to exploit temporal correlation by temporal oversampling in addition to spatial oversampling to further improve the SQNR. This approach would alleviate the need for a high spatial oversampling factor and reduce the performance degradation caused due to mutual coupling.

Overall, there are several opportunities to study the performance of low-resolutions quantizers in next generation wireless systems. $\Sigma\Delta$ ADCs, in particular, have the potential to open new areas of research in the broad field of signal processing.

Bibliography

[1] A. J. Paulraj and T. Kailath, "Increasing capacity in wireless broadcast systems using distributed transmission/directional reception (DTDR)," Sept. 6 1994, US Patent 5,345,599.

[2] F.R. Farrokhi, A. Lozano, G.J. Foschini, and R. A. Valenzuela, "Spectral efficiency of FDMA/TDMA wireless systems with transmit and receive antenna arrays," *IEEE Trans. Wireless Commun.*, vol. 1, no. 4, pp. 591–599, 2002.

[3] A. Lozano and A. M. Tulino, "Capacity of multiple-transmit multiple-receive antenna architectures," *IEEE Trans. Inf. Theory*, vol. 48, no. 12, pp. 3117–3128, 2002.

[4] T. L. Marzetta, "Noncooperative cellular wireless with unlimited numbers of base station antennas," *IEEE Trans. Wireless Commun.*, vol. 9, no. 11, pp. 3590–3600, 2010.

[5] E. G. Larsson, O. Edfors, F. Tufvesson, and T. L. Marzetta, "Massive MIMO for next generation wireless systems," *IEEE Commun. Mag.*, vol. 52, no. 2, pp. 186–195, 2014.

[6] F. Rusek, D. Persson, B. K. Lau, E. G. Larsson, T. L. Marzetta, O. Edfors, and F. Tufvesson, "Scaling up MIMO: Opportunities and challenges with very large arrays," *IEEE Signal Process. Mag.*, vol. 30, no. 1, pp. 40–60, 2012.

[7] H. Q. Ngo, A. Ashikhmin, H. Yang, E. G. Larsson, and T. L. Marzetta, "Cell-free massive MIMO versus small cells," *IEEE Trans. Wireless Commun.*, vol. 16, no. 3, pp. 1834–1850, 2017.

[8] E. Nayebi, A. Ashikhmin, T. L. Marzetta, H. Yang, and B. D. Rao, "Precoding and power optimization in cell-free massive MIMO systems," *IEEE Trans. Wireless Commun.*, vol. 16, no. 7, pp. 4445–4459, 2017.

[9] S. Rangan, T. S. Rappaport, and E. Erkip, "Millimeter-wave cellular wireless networks: Potentials and challenges," *Proc. IEEE*, vol. 102, no. 3, pp. 366–385, 2014.

[10] K. Zheng, L. Zhao, J. Mei, M. Dohler, W. Xiang, and Y. Peng, "10 Gb/s hetsnets with millimeter-wave communications: access and networking - challenges and protocols," *IEEE Commun. Mag.*, vol. 53, no. 1, pp. 222–231, 2015.

[11] A. L. Swindlehurst, E. Ayanoglu, P. Heydari, and F. Capolino, "Millimeter-wave massive MIMO: the next wireless revolution?," *IEEE Commun. Mag.*, vol. 52, no. 9, pp. 56–62, 2014.

[12] T. S. Rappaport, F. Gutierrez, E. Ben-Dor, J. N. Murdock, Y. Qiao, and J. I. Tamir, "Broadband millimeter-wave propagation measurements and models using adaptive-beam antennas for outdoor urban cellular communications," *IEEE Trans. Antennas Propag.*, vol. 61, no. 4, pp. 1850–1859, 2013.

[13] W. Roh, J.-Y. Seol, J. Park, B. Lee, J. Lee, Y. Kim, J. Cho, K. Cheun, and F. Aryanfar, "Millimeter-wave beamforming as an enabling technology for 5g cellular communications: theoretical feasibility and prototype results," *IEEE Commun. Mag.*, vol. 52, no. 2, pp. 106–113, 2014.

[14] J. Vieira, S. Malkowsky, K. Nieman, Z. Miers, N. Kundargi, L. Liu, I. Wong, V. Öwall, O. Edfors, and F. Tufvesson, "A flexible 100-antenna testbed for massive MIMO," in *Proc. Globecom*. IEEE, 2014, pp. 287–293.

[15] P. Harris, S. Zang, A. Nix, M. Beach, S. Armour, and A. Doufexi, "A distributed massive MIMO testbed to assess real-world performance and feasibility," in *Proc. VTC (Spring)*. IEEE, 2015, pp. 1–2.

[16] J. Singh, O. Dabeer, and U. Madhow, "Communication limits with low precision analog-to-digital conversion at the receiver," in *Proc. ICC*, 2007, pp. 6269–6274.

[17] O. El Ayach, S. Rajagopal, S. Abu-Surra, Z. Pi, and R. W. Heath, "Spatially sparse precoding in millimeter wave MIMO systems," *IEEE Trans. Wireless Commun.*, vol. 13, no. 3, pp. 1499–1513, 2014.

[18] S. Hur, T. Kim, D. J. Love, J. V. Krogmeier, T. A. Thomas, and A. Ghosh, "Millimeter wave beamforming for wireless backhaul and access in small cell networks," *IEEE Trans. Commun.*, vol. 61, no. 10, pp. 4391–4403, 2013.

[19] V. Venkateswaran and A.-J. van der Veen, "Analog beamforming in MIMO communications with phase shift networks and online channel estimation," *IEEE Trans. Signal Process.*, vol. 58, no. 8, pp. 4131–4143, 2010.

[20] A. Alkhateeb, O. El Ayach, G. Leus, and R. W. Heath, "Channel estimation and hybrid precoding for millimeter wave cellular systems," *IEEE J. Sel. Topics Sig. Proc.*, vol. 8, no. 5, pp. 831–846, 2014.

[21] A. Alkhateeb, J. Mo, N. Gonzalez-Prelcic, and R. W. Heath, "MIMO precoding and combining solutions for millimeter-wave systems," *IEEE Commun. Mag.*, vol. 52, no. 12, pp. 122–131, 2014.

[22] K. Roth, H. Pirzadeh, A. L. Swindlehurst, and J. A. Nossek, "A comparison of hybrid beamforming and digital beamforming with low-resolution ADCs for multiple users and imperfect CSI," *IEEE J. Sel. Topics Signal Process.*, vol. 12, no. 3, pp. 484–498, 2018.

[23] L. Kong, *Energy-efficient 60GHz phased-array design for multi-Gb/s communication systems*, Ph.D. thesis, EECS Department, University of California, Berkeley, Dec 2014.

[24] R. H. Walden, "Analog-to-digital converter survey and analysis," *IEEE J. Sel. Areas Commun.*, vol. 17, no. 4, pp. 539–550, 1999.

[25] G. P. Fettweis, "Hetnet wireless fronthaul: The challenge missed," *Proc. IEEE Commun. Theory Workshop*, 2014.

[26] A. Mezghani and J. A. Nossek, "On ultra-wideband MIMO systems with 1-bit quantized outputs: Performance analysis and input optimization," in *Proc. IEEE Int. Symp. Inf. Theory.* IEEE, 2007, pp. 1286–1289.

[27] Y. Li, C. Tao, G. Seco-Granados, A. Mezghani, A. L. Swindlehurst, and L. Liu, "Channel estimation and performance analysis of one-bit massive MIMO systems," *IEEE Trans. Signal Process.*, vol. 65, no. 15, pp. 4075–4089, August 2017.

[28] E. Björnson, M. Matthaiou, and M. Debbah, "Massive MIMO with non-ideal arbitrary arrays: Hardware scaling laws and circuit-aware design," *IEEE Trans. Wireless Commun.*, vol. 14, no. 8, pp. 4353–4368, 2015.

[29] S. Jacobsson, G. Durisi, M. Coldrey, U. Gustavsson, and C. Studer, "Throughput analysis of massive MIMO uplink with low-resolution ADCs," *IEEE Trans. Wireless Commun.*, vol. 16, no. 6, pp. 4038–4051, June 2017.

[30] E. Björnson, J. Hoydis, M. Kountouris, and M. Debbah, "Massive MIMO systems with non-ideal hardware: Energy efficiency, estimation, and capacity limits," *IEEE Trans. Inf. Theory*, vol. 60, no. 11, pp. 7112–7139, 2014.

[31] J. Mo and R. W. Heath, "Capacity analysis of one-bit quantized MIMO systems with transmitter channel state information," *IEEE Trans. Signal Process.*, vol. 63, no. 20, pp. 5498–5512, 2015.

[32] C. Risi, D. Persson, and E. G. Larsson, "Massive MIMO with 1-bit ADC," *arXiv preprint arXiv:1404.7736*, 2014.

[33] J. Choi, J. Mo, and R. W. Heath, "Near maximum-likelihood detector and channel estimator for uplink multiuser massive MIMO systems with one-bit ADCs," *IEEE Trans. Commun.*, vol. 64, no. 5, pp. 2005–2018, May 2016.

[34] H. Jedda, A. Mezghani, A. L. Swindlehurst, and J. A. Nossek, "Quantized constant envelope precoding with PSK and QAM signaling," *IEEE Trans. Wireless Commun.*, vol. 17, no. 12, pp. 8022–8034, 2018.

[35] L. Landau, M. Dörpinghaus, and G. P. Fettweis, "1-bit quantization and oversampling at the receiver: Communication over bandlimited channels with noise," *IEEE Commun. Lett.*, vol. 21, no. 5, pp. 1007–1010, 2017.

[36] D. M.V. Melo, L. T. N. Landau, and R. C. de Lamare, "Zero-crossing precoding with MMSE criterion for channels with 1-bit quantization and oversampling," in *Proc. Int. ITG Workshop on Smart Antennas*. VDE, 2020.

[37] A. K. Saxena, I. Fijalkow, and A. L. Swindlehurst, "Analysis of one-bit quantized precoding for the multiuser massive MIMO downlink," *IEEE Trans. Signal Process.*, vol. 65, no. 17, pp. 4624–4634, 2017.

[38] D. K. W. Ho and B. D. Rao, "Antithetic dithered 1-bit massive MIMO architecture: Efficient channel estimation via parameter expansion and PML," *IEEE Trans. Signal Process.*, vol. 67, no. 9, pp. 2291–2303, 2019.

[39] C. Mollén, J. Choi, E. G. Larsson, and R. W. Heath, "Uplink performance of wideband massive MIMO with one-bit ADCs," *IEEE Trans. Wireless Commun.*, vol. 16, no. 1, pp. 87–100, Jan 2017.

[40] S. Jacobsson, G. Durisi, M. Coldrey, and C. Studer, "Massive MU-MIMO-OFDM downlink with one-bit DACs and linear precoding," in *Proc. Globecom*. IEEE, 2017.

[41] D. Verenzuela, E. Björnson, and M. Matthaiou, "Hardware design and optimal ADC resolution for uplink massive MIMO systems," in *Sensor Array Multichannel Sig. Proc. Workshop (SAM)*, 2016, pp. 1–5.

[42] J. Zhang, L. Dai, S. Sun, and Z. Wang, "On the spectral efficiency of massive MIMO systems with low-resolution ADCs," *IEEE Commun. Lett.*, vol. 20, no. 5, pp. 842–845, 2016.

[43] L. Fan, S. Jin, C.-K. Wen, and H. Zhang, "Uplink achievable rate for massive MIMO systems with low-resolution ADC," *IEEE Commun. Lett.*, vol. 19, no. 12, pp. 2186–2189, 2015.

[44] Y. Li, C. Tao, A. L. Swindlehurst, A. Mezghani, and L. Liu, "Downlink achievable rate analysis in massive MIMO systems with one-bit DACs," *IEEE Commun. Lett.*, vol. 21, no. 7, pp. 1669–1672, 2017.

[45] Y.-S. Jeon, N. Lee, S.-N. H., and R. W. Heath, "One-bit sphere decoding for uplink massive MIMO systems with one-bit ADCs," *IEEE Trans. Wireless Commun.*, vol. 17, no. 7, pp. 4509–4521, 2018.

[46] P. Dong, H. Zhang, W. Xu, G. Y. Li, and X. You, "Performance analysis of multiuser massive MIMO with spatially correlated channels using low-precision ADC," *IEEE Commun. Lett.*, vol. 22, no. 1, pp. 205–208, 2017.

[47] H. Pirzadeh and A. L. Swindlehurst, "Spectral efficiency of mixed-ADC massive MIMO," *IEEE Trans. Signal Process.*, vol. 66, no. 13, pp. 3599–3613, 2018.

[48] N. Liang and W. Zhang, "Mixed-ADC massive MIMO," *IEEE J. Sel. Areas Commun.*, vol. 34, no. 4, pp. 983–997, 2016.

[49] M. T. Ivrlac and J. A. Nossek, "On MIMO channel estimation with single-bit signal-quantization," in *ITG smart antenna workshop*, 2007.

[50] O. Dabeer and U. Madhow, "Channel estimation with low-precision analog-to-digital conversion," in *Proc. Int'l Conf. Communications (ICC)*. IEEE, 2010.

[51] C. Studer and G. Durisi, "Quantized massive mu-MIMO-OFDM uplink," *IEEE Trans. Commun.*, vol. 64, no. 6, pp. 2387–2399, 2016.

[52] J. Choi, Y. Cho, B. L. Evans, and A. Gatherer, "Robust learning-based ML detection for massive MIMO systems with one-bit quantized signals," in *Proc. IEEE Global Communications Conf. (GLOBECOM)*, 2019.

[53] S. Hong, S. Kim, and N. Lee, "A weighted minimum distance decoding for uplink multiuser MIMO systems with low-resolution ADCs," *IEEE Trans. Commun.*, vol. 66, no. 5, pp. 1912–1924, 2018.

[54] L. V. Nguyen, D. T. Ngo, N. H. Tran, A. Swindlehurst, and D. H. N. Nguyen, "Supervised and Semi-Supervised Learning for MIMO Blind Detection With Low-Resolution ADCs," *IEEE Trans. Wireless Commun.*, vol. 19, no. 4, pp. 2427–2442, 2020.

[55] L. V. Nguyen, A. Swindlehurst, and D. H. N. Nguyen, "Linear and Deep Neural Network-based Receivers for Massive MIMO Systems with One-Bit ADCs," *IEEE Trans. Wireless Commun.*, 2021.

[56] L. You, X. Gao, A. L. Swindlehurst, and W. Zhong, "Channel acquisition for massive MIMO-OFDM with adjustable phase shift pilots," *IEEE Trans. Signal Process.*, vol. 64, no. 6, pp. 1461–1476, March 2016.

[57] K. Venugopal, A. Alkhateeb, N. G. Prelcic, and R. W. Heath, "Channel estimation for hybrid architecture-based wideband millimeter wave systems," *IEEE J. Sel. Areas Commun.*, vol. 35, no. 9, pp. 1996–2009, 2017.

[58] M. Kokshoorn, H. Chen, Y. Li, and B. Vucetic, "RACE: A rate adaptive channel estimation approach for millimeter wave MIMO systems," in *Proc. Globecom*, 2016.

[59] Y. Ding and B. D. Rao, "Dictionary learning-based sparse channel representation and estimation for FDD massive MIMO systems," *IEEE Trans. Wireless Commun.*, vol. 17, no. 8, pp. 5437–5451, 2018.

[60] H. Ghauch, T. Kim, M. Bengtsson, and M. Skoglund, "Subspace estimation and decomposition for large millimeter-wave MIMO systems," *IEEE J. Sel. Topics Sig. Proc.*, vol. 10, no. 3, pp. 528–542, April 2016.

[61] Z. Gao, C. Hu, L. Dai, and Z. Wang, "Channel estimation for millimeter-wave massive MIMO with hybrid precoding over frequency-selective fading channels," *IEEE Commun. Lett.*, vol. 20, no. 6, pp. 1259–1262, 2016.

[62] J. Mo, P. Schniter, and R. W. Heath, "Channel estimation in broadband millimeter wave MIMO systems with few-bit ADCs," *IEEE Trans. Signal Process.*, 2017.

[63] A. Mezghani and A. L. Swindlehurst, "Blind estimation of sparse broadband massive MIMO channels with ideal and one-bit ADCs," *IEEE Trans. Signal Process.*, vol. 66, no. 11, pp. 2972–2983, June 2018.

[64] S. Wang, Y. Li, and J. Wang, "Multiuser detection in massive spatial modulation MIMO with low-resolution ADCs," *IEEE Trans. Wireless Commun.*, vol. 14, no. 4, pp. 2156–2168, 2014.

[65] J. García, J. Munir, K. Roth, and J. A. Nossek, "Channel estimation and data equalization in frequency-selective MIMO systems with one-bit quantization," *arXiv preprint arXiv:1609.04536*, 2016.

[66] O. Bar-Shalom and A. J. Weiss, "DOA estimation using one-bit quantized measurements," *IEEE Trans. Aerosp. Electron. Syst.*, vol. 38, no. 3, pp. 868–884, 2002.

[67] C.L. Liu and P.P. Vaidyanathan, "One-bit sparse array DOA estimation," in *Proc. ICASSP*. IEEE, 2017, pp. 3126–3130.

[68] S. Sedighi, B. Shankar, M. Soltanalian, and B. Ottersten, "One-bit DoA estimation via sparse linear arrays," in *Proc. ICASSP*, 2020, pp. 9135–9139.

[69] K. Yu, Y. D. Zhang, M. Bao, Y. Hu, and Z. Wang, "DOA estimation from one-bit compressed array data via joint sparse representation," *IEEE Signal Process. Lett.*, vol. 23, no. 9, pp. 1279–1283, 2016.

[70] C. Stöckle, J. Munir, A. Mezghani, and J. A. Nossek, "1-bit direction of arrival estimation based on compressed sensing," in *Proc. IEEE. Int. Workshop on Sig. Proc. Advances in Wireless Communications (SPAWC)*, 2015, pp. 246–250.

[71] X. Huang and B. Liao, "One-bit MUSIC," *IEEE Signal Process. Lett.*, vol. 26, no. 7, pp. 961–965, 2019.

[72] R. A. Fisher, "Theory of statistical estimation," in *Math. proc. of the Cambridge philosophical society*. Cambridge University Press, 1925, vol. 22, pp. 700–725.

[73] H. Cramér, "A contribution to the theory of statistical estimation," *Scandinavian Actuarial Journal*, vol. 1946, no. 1, pp. 85–94, 1946.

[74] C. R. Rao, "Information and the accuracy attainable in the estimation of statistical parameters," in *Breakthroughs in statistics*, pp. 235–247. Springer, 1992.

[75] M. S. Stein, J. A. Nossek, and K. Barbé, "Fisher information lower bounds with applications in hardware-aware nonlinear signal processing, compression and inference," *CoRR*, vol. abs/1512.03473, 2015.

[76] M. Stein, K. Barbe, and J. A. Nossek, "DOA parameter estimation with 1-bit quantization bounds, methods and the exponential replacement," in *Proc. Int. ITG Workshop on Smart Antennas*, March 2016.

[77] F. Liu, H. Zhu, J. Li, P. Wang, and P. V. Orlik, "Massive MIMO channel estimation using signed measurements with antenna-varying thresholds," in *IEEE Stat. Sig. Proc. Workshop (SSP)*, June 2018, pp. 188–192.

[78] P. Wang, J. Li, M. Pajovic, P. T. Boufounos, and P. V. Orlik, "On angular-domain channel estimation for one-bit massive MIMO systems with fixed and time-varying thresholds," in *Asilomar Conf. on Signals, Systems, and Computers*, Oct 2017, pp. 1056–1060.

[79] M. Cai, K. Gao, D. Nie, B. Hochwald, J. N. Laneman, H. Huang, and K. Liu, "Effect of wideband beam squint on codebook design in phased-array wireless systems," in *Proc. Globecom*, Dec 2016.

[80] R. L. Haupt, "Antenna arrays in the time domain: An introduction to timed arrays.," *IEEE Antennas Propag. Mag.*, vol. 59, no. 3, pp. 33–41, June 2017.

[81] B. Wang, F. Gao, S. Jin, H. Lin, and G. Y. Li, "Spatial- and frequency-wideband effects in millimeter-wave massive MIMO systems," *IEEE Trans. Signal Process.*, vol. 66, no. 13, pp. 3393–3406, July 2018.

[82] B. Wang, F. Gao, S. Jin, H. Lin, G. Y. Li, S. Sun, and T. S. Rappaport, "Spatial-wideband effect in massive MIMO with application in mmWave systems," *IEEE Commun. Mag.*, vol. 56, no. 12, pp. 134–141, Dec 2018.

[83] T. Koch and A. Lapidoth, "Increased capacity per unit-cost by oversampling," in *Conv. Elect. and Electron. Eng. Israel (IEEEI)*, 2010, pp. 684–688.

[84] S. Shamai, "Information rates by oversampling the sign of a bandlimited process," *IEEE Trans. Inf. Theory*, vol. 40, no. 4, pp. 1230–1236, 1994.

[85] S. Krone and G. Fettweis, "Capacity of communications channels with 1-bit quantization and oversampling at the receiver," in *IEEE Sarnoff Symp.*, 2012, pp. 1–7.

[86] A. Gokceoglu, E. Björnson, E. G. Larsson, and M. Valkama, "Spatio-temporal waveform design for multiuser massive MIMO downlink with 1-bit receivers," *IEEE J. Sel. Topics Sig. Proc.*, vol. 11, no. 2, pp. 347–362, March 2017.

[87] A. B. Üçüncü and A. Ö. Yilmaz, "Oversampling in one-bit quantized massive MIMO systems and performance analysis," *IEEE Trans. Wireless Commun.*, vol. 17, no. 12, pp. 7952–7964, Dec. 2018.

[88] Z. Shao, L. T. N. Landau, and R. C. De Lamare, "Channel estimation for large-scale multiple-antenna systems using 1-bit ADCs and oversampling," *IEEE Access*, vol. 8, pp. 85243–85256, 2020.

[89] M. S. Stein, "Performance analysis for time-of-arrival estimation with oversampled low-complexity 1-bit A/D conversion," in *Proc. ICASSP*. IEEE, 2017, pp. 4491–4495.

[90] M. Schlüter, M. Dörpinghaus, and G. P. Fettweis, "Bounds on channel parameter estimation with 1-bit quantization and oversampling," in *Proc. IEEE. Int. Workshop on Sig. Proc. Advances in Wireless Communications (SPAWC)*, June 2018.

[91] P. M. Aziz, H. V. Sorensen, and J. Van der Spiegel, "An overview of sigma-delta converters," *IEEE Signal Process. Mag.*, vol. 13, no. 1, pp. 61–84, 1996.

[92] R Gray, "Oversampled sigma-delta modulation," *IEEE Trans. Commun.*, vol. 35, no. 5, pp. 481–489, 1987.

[93] R. M. Gray, W. Chou, and P. W. Wong, "Quantization noise in single-loop sigma-delta modulation with sinusoidal inputs," *IEEE Trans. Commun.*, vol. 37, no. 9, pp. 956–968, Sep 1989.

[94] D. S. Palguna, D. J. Love, T. A. Thomas, and A. Ghosh, "Millimeter wave receiver design using low precision quantization and parallel $\Delta\Sigma$ architecture," *IEEE Trans. Wireless Commun.*, vol. 15, no. 10, pp. 6556–6569, Oct 2016.

[95] V. Venkateswaran and A. van der Veen, "Multichannel $\Sigma\Delta$ ADCs with integrated feedback beamformers to cancel interfering communication signals," *IEEE Trans. Signal Process.*, vol. 59, no. 5, pp. 2211–2222, May 2011.

[96] J. J. Bussgang, "Crosscorrelation functions of amplitude-distorted Gaussian signals," Tech. Rep., MIT Research Lab. Electronics, March 1952, 216.

[97] R. Price, "A useful theorem for nonlinear devices having Gaussian inputs," *IRE Trans. Inf. Theory*, vol. 4, no. 2, pp. 69–72, 1958.

[98] K. Hosseini, M. P. Kennedy, S. H. Lewis, and B. C. Levy, "Prediction of the spectrum of a digital delta–sigma modulator followed by a polynomial nonlinearity," *IEEE Trans. Circuits Syst. I, Reg. Papers*, vol. 57, no. 8, pp. 1905–1913, 2010.

[99] R. M. Corey and A. C. Singer, "Spatial sigma-delta signal acquisition for wideband beamforming arrays," in *Proc. Int. ITG Workshop on Smart Antennas*, March 2016.

[100] D. Barac and E. Lindqvist, "Spatial sigma-delta modulation in a massive MIMO cellular system," M.S. thesis, Department of Computer Science and Engineering, Chalmers University of Technology, 2016.

[101] S. Rao, A. L. Swindlehurst, and H. Pirzadeh, "Massive MIMO channel estimation with 1-bit spatial sigma-delta ADCs," in *Proc. ICASSP*. IEEE, 2019, pp. 4484–4488.

[102] M. Shao, W. Ma, Q. Li, and A. L. Swindlehurst, "One-bit sigma-delta MIMO precoding," *IEEE J. Sel. Topics Sig. Proc.*, vol. 13, no. 5, pp. 1046–1061, Sep. 2019.

[103] H. Pirzadeh, G. Seco-Granados, S. Rao, and A. L. Swindlehurst, "Spectral efficiency of one-bit sigma-delta massive MIMO," *IEEE J. Sel. Areas Commun.*, vol. 38, no. 9, pp. 2215–2226, 2020.

[104] D. P. Scholnik, J. O. Coleman, D. Bowling, and M. Neel, "Spatio-temporal delta-sigma modulation for shared wideband transmit arrays," in *Proc. Radar Conf.* IEEE, 2004, pp. 85–90.

[105] J. D. Krieger, C. P. Yeang, and G. W. Wornell, "Dense delta-sigma phased arrays," *IEEE Trans. Antennas Propag.*, vol. 61, no. 4, pp. 1825–1837, April 2013.

[106] A. Madanayake, N. Akram, S. Mandal, J. Liang, and L. Belostotski, "Improving ADC figure-of-merit in wideband antenna array receivers using multidimensional space-time delta-sigma multiport circuits," in *Int. Workshop on Multidimensional (nD) Sys. (nDS)*, Sept 2017.

[107] A. Nikoofard, J. Liang, M. Twieg, S. Handagala, A. Madanayake, L. Belostotski, and S. Mandal, "Low-complexity N-port ADCs using 2-D sigma-delta noise-shaping for N-element array receivers," in *Int. Midwest Symp. on Circuits and Systems (MWSCAS)*, Aug 2017, pp. 301–304.

[108] R.S. Prasobh Sankar and S. P. Chepuri, "Millimeter Wave MIMO Channel Estimation with 1-bit Spatial Sigma-Delta Analog-to-Digital Converters," in *Proc. ICASSP*, 2021, pp. 4810–4814.

[109] R. S. P. Sankar and S. P. Chepuri, "Channel estimation in MIMO systems with one-bit spatial sigma-delta ADCs," 2021.

[110] M. Viberg and A. L. Swindlehurst, "A Bayesian approach to auto-calibration for parametric array signal processing," *IEEE Trans. Signal Process.*, vol. 42, no. 12, pp. 3495–3507, 1994.

[111] B. Wahlberg, B. Ottersten, and M. Viberg, "Robust signal parameter estimation in the presence of array perturbations," in *Proc. ICASSP.* IEEE, 1991, pp. 3277–3280.

[112] J.X. Zhu and H. Wang, "Effects of sensor position and pattern perturbations on CRLB for direction finding of multiple narrow-band sources," in *IEEE ASSP Workshop On Spect. Estim. and Modeling*, 1988, pp. 98–102.

[113] H. Pirzadeh, G. Seco-Granados, A. L. Swindlehurst, and J. A. Nossek, "On the effect of mutual coupling in one-bit spatial sigma-delta massive MIMO systems," in *Proc. IEEE. Int. Workshop on Sig. Proc. Advances in Wireless Communications (SPAWC)*, 2020.

[114] R. Schmidt, "Multiple emitter location and signal parameter estimation," *IEEE Trans. Antennas Propag.*, vol. 34, no. 3, pp. 276–280, 1986.

[115] H. Pirzadeh, S. Rao, and A. L. Swindlehurst, "Direction finding with 2D arrays using spatial sigma-delta ADCs," in *Proc. IEEE. Int. Workshop on Sig. Proc. Advances in Wireless Communications (SPAWC)*, 2021, pp. 391–395.

[116] M. Viberg and A.L. Swindlehurst, "Analysis of the combined effects of finite samples and model errors on array processing performance," *IEEE Trans. Signal Process.*, vol. 42, no. 11, pp. 3073–3083, 1994.

[117] A.L. Swindlehurst and T. Kailath, "A performance analysis of subspace-based methods in the presence of model errors. Part II: Multidimensional algorithms," *IEEE Trans. Signal Process.*, vol. 41, no. 9, pp. 2882–2890, 1993.

[118] S. Lloyd, "Least squares quantization in PCM," *IEEE Trans. Inf. Theory*, vol. 28, no. 2, pp. 129–137, 1982.

[119] J. Max, "Quantizing for minimum distortion," *IRE Trans. Inf. Theory*, vol. 6, no. 1, pp. 7–12, 1960.

[120] P.A. Chou, T. Lookabaugh, and R.M. Gray, "Entropy-constrained vector quantization," *IEEE Trans. Acoust., Speech, Signal Process.*, vol. 37, no. 1, pp. 31–42, 1989.

[121] A.V. Oppenheim and R.W. Schafer, *Discrete-time Signal Processing*, Prentice-Hall signal processing series. Prentice Hall, 1989.

[122] E. W. Barankin, "Locally best unbiased estimates," *The Annals of Mathematical Statistics*, vol. 20, no. 4, pp. 477–501, 1949.

[123] A. Bhattacharyya, "On some analogues of the amount of information and their use in statistical estimation," *Sankhya: The Indian Journal of Statistics (1933-1960)*, vol. 8, no. 1, pp. 1–14, 1946.

[124] J. Ziv and M. Zakai, "Some lower bounds on signal parameter estimation," *IEEE Trans. Inf. Theory*, vol. 15, no. 3, pp. 386–391, 1969.

[125] E. Weinstein and A.J. Weiss, "A general class of lower bounds in parameter estimation," *IEEE Trans. Inf. Theory*, vol. 34, no. 2, pp. 338–342, 1988.

[126] S. M. Kay, *Fundamentals of Statistical Signal Processing: Estimation Theory*, Prentice-Hall, Inc., Upper Saddle River, NJ, USA, 1993.

[127] T.S. Rappaport, *Wireless Communications: Principles and Practice*, Electrical engineering. Prentice Hall PTR, 1996.

[128] A. Goldsmith, *Wireless Communications*, Cambridge University Press, 2005.

[129] M. Schluter, M. Dorpinghaus, and G. P. Fettweis, "Bounds on channel parameter estimation with 1-bit quantization and oversampling," in *Proc. IEEE. Int. Workshop on Sig. Proc. Advances in Wireless Communications (SPAWC)*, June 2018.

[130] C. Mollén, *High-End Performance with Low-End Hardware*, Linköping Studies in Science and Technology. PhD Dissertation. 2018.

[131] H. L. Van Trees, *Detection, estimation, and modulation theory, Part I*, John Wiley & Sons, 2004.

[132] T. S. Rappaport, G. R. MacCartney, M. K. Samimi, and S. Sun, "Wideband millimeter-wave propagation measurements and channel models for future wireless communication system design," *IEEE Trans. Commun.*, vol. 63, no. 9, pp. 3029–3056, 2015.

[133] A. Mezghani, F. Antreich, and J. Nossek, "Multiple parameter estimation with quantized channel output," in *Proc. Int. ITG Workshop on Smart Antennas*. IEEE, 2010.

[134] M. Stein, F. Wendler, A. Mezghani, and J. A. Nossek, "Quantization-loss reduction for signal parameter estimation," in *Proc. ICASSP*. IEEE, 2013, pp. 5800–5804.

[135] M. Lin and L. Yang, "Blind calibration and DOA estimation with uniform circular arrays in the presence of mutual coupling," *IEEE Antennas Wireless Propag. Lett.*, vol. 5, pp. 315–318, 2006.

[136] S.A. Schelkunoff and H.T. Friis, *Antennas: Theory and Practice*, Wiley, 1952.

[137] M. T. Ivrlač and J. A. Nossek, "Toward a circuit theory of communication," *IEEE Trans. Circuits Syst. I, Reg. Papers*, vol. 57, no. 7, pp. 1663–1683, 2010.

[138] Q. Zhang, S. Jin, K.-K. Wong, H. Zhu, and M. Matthaiou, "Power scaling of uplink massive MIMO systems with arbitrary-rank channel means," *IEEE Trans. Signal Process.*, vol. 8, no. 5, pp. 966–981, 2014.

[139] H. Q. Ngo, M. Matthaiou, and E. G. Larsson, "Performance analysis of large scale MU-MIMO with optimal linear receivers," in *Proc. Swe-CTW*, 2012.

[140] X. Li, E. Björnson, E. G. Larsson, S. Zhou, and J. Wang, "A multi-cell MMSE detector for massive MIMO systems and new large system analysis," in *Proc. Globecom*. IEEE, 2015, pp. 1–6.

[141] P. Stoica and A. Nehorai, "Performance study of conditional and unconditional direction-of-arrival estimation," *IEEE Trans. Acoust., Speech, Signal Process.*, vol. 38, no. 10, pp. 1783–1795, 1990.

[142] A. L. Swindlehurst and T. Kailath, "A performance analysis of subspace-based methods in the presence of model errors, Part I. The MUSIC algorithm," *IEEE Trans. Signal Process.*, vol. 40, no. 7, pp. 1758–1774, 1992.

[143] T. Chen, M. Guo, and X. Huang, "Direction finding using compressive one-bit measurements," *IEEE Access*, vol. 6, pp. 41201–41211, 2018.

[144] X. Huang, P. Xiao, and B. Liao, "One-bit direction of arrival estimation with an improved fixed-point continuation algorithm," in *Int. Conf. on Wireless Comm. Sig. Proces. (WCSP)*, 2018, pp. 1–4.

[145] S. Sedighi, M. R. B. Shankar, M. Soltanalian, and B. Ottersten, "On the performance of one-bit doa estimation via sparse linear arrays," 2020.

[146] M. Viberg, B. Ottersten, and A. Nehorai, "Performance analysis of direction finding with large arrays and finite data," *IEEE Trans. Signal Process.*, vol. 43, no. 2, pp. 469–477, 1995.

[147] Y. Huang and W. F. McColl, "Analytical inversion of general tridiagonal matrices," *J. Phy. A: Math. Gen.*, vol. 30, no. 22, pp. 7919–7933, 1997.

[148] S. Rao, G. Seco-Granados, H. Pirzadeh, J. A. Nossek, and A. L. Swindlehurst, "Massive MIMO channel estimation with low-resolution spatial sigma-delta ADCs," *IEEE Access*, vol. 9, pp. 109320–109334, 2021.

[149] K. N. Ramamohan, S. Prabhakar C., D. F. Comesaña, and G. Leus, "Blind calibration of sparse arrays for DOA estimation with analog and one-bit measurements," in *Proc. ICASSP*, 2019, pp. 4185–4189.

[150] J. C. Spall, "Monte carlo computation of the fisher information matrix in nonstandard settings," *Journal of Computational and Graphical Statistics*, vol. 14, no. 4, pp. 889–909, 2005.

[151] V. Berisha and A. O. Hero, "Empirical non-parametric estimation of the Fisher information," *IEEE Signal Process. Lett.*, vol. 22, no. 7, pp. 988–992, 2014.

[152] L. Livi, F. M. Bianchi, and C. Alippi, "Determination of the edge of criticality in echo state networks through Fisher information maximization," *IEEE Trans. on neural networks and learning systems*, vol. 29, no. 3, pp. 706–717, 2017.

[153] Mi. Tu, V. Berisha, M. Woolf, J.-S. Seo, and Y. Cao, "Ranking the parameters of deep neural networks using the fisher information," in *Proc. ICASSP*. IEEE, 2016, pp. 2647–2651.

[154] P. Stoica and A. Nehorai, "MUSIC, maximum likelihood, and Cramér-Rao bound," *IEEE Trans. Acoust., Speech, Signal Process.*, vol. 37, no. 5, pp. 720–741, 1989.

Appendix A

Fisher Information

$$[\mathbf{J}_{\boldsymbol{\theta}}]_{i,j} = \mathbb{E}\left[\frac{\partial l(\mathbf{x};\boldsymbol{\Theta})}{\partial \theta_i}\frac{\partial l(\mathbf{x};\boldsymbol{\Theta})}{\partial \theta_j}\right]$$

$$= \mathbb{E}\left[\sum_{k=1}^{2MN}\sum_{l=1}^{2MN}\frac{4}{\sigma^2}\frac{\Psi'\left(\frac{2}{\sigma}x_k u_k\right)\Psi'\left(\frac{2}{\sigma}x_l u_l\right)}{\Psi\left(\frac{2}{\sigma}x_k u_k\right)\Psi\left(\frac{2}{\sigma}x_l u_l\right)}x_k x_l\left(\mathbf{D}_{\boldsymbol{\theta}}^{(,i)}\right)^T\mathbf{s}^{(k,)}\left(\mathbf{s}^{(l,)}\right)^T\mathbf{D}_{\boldsymbol{\theta}}^{(,j)}\right]$$

$$= \mathbb{E}\left[\sum_{k=1}^{2MN}\left(\frac{2x_k}{\sigma}\frac{\Psi'\left(\frac{2}{\sigma}x_k u_k\right)}{\Psi\left(\frac{2}{\sigma}x_k u_k\right)}\right)^2\left(\mathbf{D}_{\boldsymbol{\theta}}^{(,i)}\right)^T\mathbf{s}^{(k,)}\left(\mathbf{s}^{(k,)}\right)^T\mathbf{D}_{\boldsymbol{\theta}}^{(,j)}\right.$$

$$\left.+\sum_{k=1}^{2MN}\sum_{l\neq k}\frac{4}{\sigma^2}\frac{\Psi'\left(\frac{2}{\sigma}x_k u_k\right)\Psi'\left(\frac{2}{\sigma}x_l u_l\right)}{\Psi\left(\frac{2}{\sigma}x_k u_k\right)\Psi\left(\frac{2}{\sigma}x_l u_l\right)}x_k x_l\left(\mathbf{D}_{\boldsymbol{\theta}}^{(,i)}\right)^T\mathbf{s}^{(k,)}\left(\mathbf{s}^{(l,)}\right)^T\mathbf{D}_{\boldsymbol{\theta}}^{(,j)}\right]$$

$$= \sum_{k=1}^{2MN}\frac{2}{\sigma^2}\frac{\left(\Psi'\left(\frac{\sqrt{2}}{\sigma}u_k\right)\right)^2}{\Psi\left(\frac{\sqrt{2}}{\sigma}u_k\right)\left(1-\Psi\left(\frac{\sqrt{2}}{\sigma}u_k\right)\right)}\left(\mathbf{D}_{\boldsymbol{\theta}}^{(,i)}\right)^T\mathbf{s}^{(k,)}\left(\mathbf{s}^{(k,)}\right)^T\mathbf{D}_{\boldsymbol{\theta}}^{(,j)}$$

$$= \left(\mathbf{D}_{\boldsymbol{\theta}}^{(,i)}\right)^T\mathbf{S}^T\,\boldsymbol{\Psi}_D\,\mathbf{S}\,\mathbf{D}_{\boldsymbol{\theta}}^{(,j)}.$$

Other sub-matrices can be derived in a similar manner.

Appendix B

Jacobians

The Jacobian matrices are computed below.

$$\mathbf{D}_{\boldsymbol{\theta}} = \left[\frac{\partial \mathbf{h}}{\partial \theta_1}, \frac{\partial \mathbf{h}}{\partial \theta_2}, \ldots, \frac{\partial \mathbf{h}}{\partial \theta_R} \right]$$

$$\frac{\partial \mathbf{h}}{\partial \theta_r} = \left[\begin{array}{c} \mathrm{Re}\left(\mathrm{vec}\left(\frac{\partial \mathbf{H}}{\partial \theta_r} \right) \right) \\ \mathrm{Im}\left(\mathrm{vec}\left(\frac{\partial \mathbf{H}}{\partial \theta_r} \right) \right) \end{array} \right]$$

$$\frac{\partial \mathbf{H}}{\partial \theta_r} = \left[\begin{array}{cccc} \frac{\partial \mathbf{h}[0]}{\partial \theta_r} & \frac{\partial \mathbf{h}[1]}{\partial \theta_r} & \cdots & \frac{\partial \mathbf{h}[L-1]}{\partial \theta_r} \\ \frac{\partial \mathbf{h}[\frac{1}{P}]}{\partial \theta_r} & \frac{\partial \mathbf{h}[1+\frac{1}{P}]}{\partial \theta_r} & \cdots & \frac{\partial \mathbf{h}[L-1+\frac{1}{P}]}{\partial \theta_r} \\ \vdots & \vdots & \vdots & \vdots \\ \frac{\partial \mathbf{h}[\frac{P-1}{P}]}{\partial \theta_r} & \frac{\partial \mathbf{h}[1+\frac{P-1}{P}]}{\partial \theta_r} & \cdots & \frac{\partial \mathbf{h}[L-1+\frac{P-1}{P}]}{\partial \theta_r} \end{array} \right].$$

It is sufficient to compute one of the blocks since the other blocks can be computed in a recursive manner:

$$\frac{\partial \mathbf{h}[k]}{\partial \theta_r} = \gamma_r \begin{bmatrix} \frac{\partial g(kTs-\tau_{r,1})}{\partial \theta_r} \\ \frac{\partial g(kT_s-\tau_{r,2})}{\partial \theta_r} \\ \vdots \\ \frac{\partial g\left(kT_s-\tau_{r,M}\right)}{\partial \theta_r} \end{bmatrix} \odot \mathbf{a}(\theta_r, \boldsymbol{\rho}) + \gamma_r \begin{bmatrix} g(kTs-\tau_{r,1}) \\ g\left(kT_s-\tau_{r,2}\right) \\ \vdots \\ g\left(kT_s-\tau_{r,M}\right) \end{bmatrix} \odot \frac{\partial \mathbf{a}(\theta_r, \boldsymbol{\rho})}{\partial \theta_r}.$$

If we further assume a uniform linear array, the algebra is straightforward and, at the nominal array perturbation, we get

$$\frac{\partial \mathbf{h}[k]}{\partial \theta_r} = \gamma_r \begin{bmatrix} 0 \\ \frac{\partial g\left(kT_s-\tau_r-\frac{\delta \sin \theta_r}{c}\right)}{\partial \theta_r} \\ \vdots \\ \frac{\partial g\left(kT_s-\tau_r-\frac{\delta(M-1)\sin \theta_r}{c}\right)}{\partial \theta_r} \end{bmatrix} \odot \mathbf{a}(\theta_r, \boldsymbol{\rho}_0) + \gamma_r \begin{bmatrix} g(kTs-\tau_r) \\ g\left(kT_s-\tau_r-\frac{\delta \sin \theta_r}{c}\right) \\ \vdots \\ g\left(kT_s-\tau_r-\frac{\delta(M-1)\sin \theta_r}{c}\right) \end{bmatrix} \odot \frac{\partial \mathbf{a}(\theta_r, \boldsymbol{\rho}_0)}{\partial \theta_r}.$$

The derivative of $g\left(kT_s - \tau_r - \frac{\delta \sin \theta_r}{c}\right)$ with respect to θ_r is shown in (B.1) at the top of the next page. The derivatives of the array steering vector can also be computed in a similar manner. For the above uniform linear array, under nominal perturbation values ($q_{m,0} = 1, \rho_m = 0$ for the pattern pertubation when the perturbation is not a function of the DOA, and $\rho_m = 0$ for the sensor position perturbation case), we have

$$\frac{\partial \mathbf{a}(\theta_r, \boldsymbol{\rho}_0)}{\partial \theta_r} = \frac{-j2\pi\delta \cos \theta_r}{\lambda} \begin{bmatrix} 0, & 1, & \ldots, & M-1 \end{bmatrix}^T \odot \mathbf{a}(\theta_r, \boldsymbol{\rho}_0).$$

The Jacobian of $\mathbf{h}$ with respect to $\boldsymbol{\tau}$, $\mathbf{D}_{\boldsymbol{\tau}}$ is

$$\frac{\partial g\left(kT_s - \tau_r - \frac{\delta \sin\theta_r}{c}\right)}{\partial \theta_r} =$$

$$\frac{\cos \pi\alpha(kT_s - \tau_r - \frac{\delta \sin\theta_r}{c})/T_s}{1 - 4\alpha^2(kT_s - \tau_r - \frac{\delta \sin\theta_r}{c})^2/T_s^2}\left(-\frac{\delta\cos\theta_r}{c}\right)\frac{\left(\cos\frac{\pi(kT_s - \tau_r - \frac{\delta\sin\theta_r}{c})}{T_s} - \mathrm{sinc}\frac{(kT_s - \tau_r - \frac{\delta\sin\theta_r}{c})}{T_s}\right)}{\left(\pi(kT_s - \tau_r - \frac{\delta\sin\theta_r}{c})/T_s\right)} +$$

$$\mathrm{sinc}\frac{(kT_s - \tau_r - \frac{\delta\sin\theta_r}{c})}{T_s}\frac{\delta}{c}\cos\theta_r\left[\frac{(1 - 4\alpha^2(kT_s - \tau_r - \frac{\delta\sin\theta_r}{c})^2/T_s^2)\frac{\pi\alpha}{T_s}\sin\pi\alpha(kT_s - \tau_r - \frac{\delta\sin\theta_r}{c})/T_s}{(1 - 4\alpha^2(kT_s - \tau_r - \frac{\delta\sin\theta_r}{c})^2/T_s^2)^2}\right.$$

$$\left. -\frac{8\alpha^2(kT_s - \tau_r - \frac{\delta\sin\theta_r}{c})/T_s^2\cos\pi\alpha(kT_s - \tau_r - \frac{\delta\sin\theta_r}{c})/T_s}{(1 - 4\alpha^2(kT_s - \tau_r - \frac{\delta\sin\theta_r}{c})^2/T_s^2)^2}\right]$$

$$\text{(B.1)}$$

$$\frac{\partial g(kT_s - \tau_{r,m})}{\partial \tau_{r,m}} = \frac{\cos\frac{\pi\alpha(kT_s - \tau_r)}{T_s}}{1 - \frac{4\alpha^2(kT_s - \tau_r)^2}{T_s^2}}\left(\frac{-\pi}{T_s}\right)\frac{\left(\cos\frac{\pi(kT_s - \tau_{r,m})}{T_s} - \mathrm{sinc}\frac{(kT_s - \tau_{r,m})}{T_s}\right)}{\pi(kT_s - \tau_{r,m})/T_s} +$$

$$\mathrm{sinc}\frac{(kT_s - \tau_{r,m})}{T_s}\frac{\left[\left(1 - \frac{4\alpha^2(kT_s - \tau_{r,m})}{T_s^2}\right)\sin\frac{\pi\alpha(kT_s - \tau_{r,m})}{T_s} - \frac{8\alpha^2(kT_s - \tau_{r,m})}{T_s^2}\cos\frac{\pi\alpha(kT_s - \tau_{r,m})}{T_s}\right]}{(1 - \frac{4\alpha^2(kT_s - \tau_{r,m})^2}{T_s^2})^2}$$

$$\mathbf{D}_{\boldsymbol{\tau}} = \left[\frac{\partial \mathbf{h}}{\partial \tau_{1,1}}, \frac{\partial \mathbf{h}}{\partial \tau_{1,2}}, \dots, \frac{\partial \mathbf{h}}{\partial \tau_{R,M-1}}, \frac{\partial \mathbf{h}}{\partial \tau_{R,M}}\right],$$

$$\frac{\partial \mathbf{h}}{\partial \tau_{r,m}} = \left[\begin{array}{c}\mathrm{Re}\left(\mathrm{vec}\left(\frac{\partial \mathbf{H}}{\partial \tau_{r,m}}\right)\right)\\ \mathrm{Im}\left(\mathrm{vec}\left(\frac{\partial \mathbf{H}}{\partial \tau_{r,m}}\right)\right)\end{array}\right],$$

$$\frac{\partial \mathbf{h}[k]}{\partial \tau_{r,m}} = \gamma_r \left[\begin{array}{ccccc}0 & \dots & \frac{\partial g(kT_s - \tau_{r,m})}{\partial \tau_{r,m}} & \dots & 0\end{array}\right]^T \odot \mathbf{a}(\theta_r, \boldsymbol{\rho}).$$

The derivative of $g\left(kT_s - \tau_{r,m}\right)$ with respect to $\tau_{r,m}$ is shown in (B.1) at the top of the next page. For a ULA, $\boldsymbol{\tau} = [\tau_1, \dots, \tau_R]^T$, $\tau_{r,m} = \tau_r + \delta(m-1)\sin\theta_r/c$ and the Jacobian can be derived in a straightforward manner. We can derive $\mathbf{D}_{\boldsymbol{\gamma}^{\mathrm{Re}}}$, $\mathbf{D}_{\boldsymbol{\gamma}^{\mathrm{Im}}}$ and $\mathbf{D}_{\boldsymbol{\rho}}$ from the following

expressions,

$$\frac{\partial \mathbf{h}[k]}{\partial \gamma_r^{\mathrm{Re}}} = \begin{bmatrix} g(kTs - \tau_{r,1}) \\ g\left(kT_s - \tau_{r,2}\right) \\ \vdots \\ g\left(kT_s - \tau_{r,M}\right) \end{bmatrix} \odot \mathbf{a}(\theta_r, \boldsymbol{\rho}), \ \frac{\partial \mathbf{h}[k]}{\partial \gamma_r^{\mathrm{Im}}} = j\frac{\partial \mathbf{h}[k]}{\partial \gamma_r^{\mathrm{Re}}},$$

$$\frac{\partial \mathbf{h}[k]}{\partial \rho_d} = \sum_{r=1}^{R} \gamma_r \begin{bmatrix} g(kTs - \tau_{r,1}) \\ g\left(kT_s - \tau_{r,2}\right) \\ \vdots \\ g\left(kT_s - \tau_{r,M}\right) \end{bmatrix} \odot \frac{\partial \mathbf{a}(\theta_r, \boldsymbol{\rho})}{\partial \rho_d}.$$

Let $\mathbf{e}_m \in \mathbb{R}^{M \times 1}$ be the unit vector with a 1 at the mth index. There are $2MR$ perturbation parameters in the case of pattern perturbation and $M-1$ parameters in the case of position perturbation. If we consider the pattern only perturbations with the pattern perturbation independent of the DOA, $\boldsymbol{\rho} = [\mathrm{Re}(\rho_1), \dots, \mathrm{Re}(\rho_M), \mathrm{Im}(\rho_1), \dots, \mathrm{Im}(\rho_M)]^T$ and

$$\left.\frac{\partial \mathbf{h}[k]}{\partial \mathrm{Re}(\rho_m)}\right|_{\boldsymbol{\rho}=\mathbf{0}} = \sum_{r=1}^{R} \gamma_r \begin{bmatrix} g(kTs - \tau_{r,1}) \\ g\left(kT_s - \tau_{r,2}\right) \\ \vdots \\ g\left(kT_s - \tau_{r,M}\right) \end{bmatrix} \odot \exp(-j2\pi(b_m \sin\theta_r + c_m \cos\theta_r)/\lambda)\mathbf{e}_m,$$

$$\left.\frac{\partial \mathbf{h}[k]}{\partial \mathrm{Im}(\rho_m)}\right|_{\boldsymbol{\rho}=\mathbf{0}} = j\left.\frac{\partial \mathbf{h}[k]}{\partial \mathrm{Re}(\rho_m)}\right|_{\boldsymbol{\rho}=\mathbf{0}}.$$

Similarly, for nominal uniform linear arrays with position perturbation only we have [110]

$$\left.\frac{\partial \mathbf{h}[k]}{\partial \rho_m}\right|_{\boldsymbol{\rho}=\mathbf{0}} = \sum_{r=1}^{R} \gamma_r \begin{bmatrix} g(kTs - \tau_{r,1}) \\ g\left(kT_s - \tau_{r,2}\right) \\ \vdots \\ g\left(kT_s - \tau_{r,M}\right) \end{bmatrix} \odot (j2\pi\delta \cos\theta_r/\lambda)\mathrm{diag}(\mathbf{a}(\theta_r, \mathbf{0})) \left(\sum_{k=1}^{M-m} k\mathbf{e}_{k+m}\right).$$

$$(B.2)$$

For arrays which are not uniform linear arrays, expressions for the derivatives can be derived in a manner similar to (B.2).

Appendix C

Proof of cross-correlation

We will prove that $\mathbb{E}\left[x_m q_n^*\right] \approx 0$, $\forall m, n$ following an approach similar to that in Appendix A of [27]. We can express $\mathbb{E}\left[x_m q_n^*\right]$ as

$$\mathbb{E}\left[x_m q_n^*\right] = \mathbb{E}_{r_n}\left[\mathbb{E}\left[x_m q_n^*|r_n\right]\right] = \mathbb{E}_{r_n}\left[\mathbb{E}\left[x_m|r_n\right] q_n^*\right], \tag{C.1}$$

where the last equality follows from the fact that $q_n = y_n - r_n$ is fixed for a given r_n. $\mathbb{E}\left[x_m|r_n\right]$ is the MMSE estimate of x_m given r_n. Since we assume that r_n is approximately a Gaussian random variable, the MMSE estimate of the Gaussian variable x_m will be approximately equivalent to the LMMSE estimate given by

$$\mathbb{E}\left[x_m|r_n\right] \approx \frac{\mathbb{E}\left[x_m r_n^*\right]}{\sigma_{r_n}^2} r_n. \tag{C.2}$$

Using (C.2) and the fact that r_n is uncorrelated with q_n, we have

$$\mathbb{E}\left[x_m q_n^*\right] \approx \frac{\mathbb{E}\left[x_m r_n^*\right]}{\sigma_{r_n}^2}\mathbb{E}_{r_n}\left[r_n q_n^*\right] = 0. \tag{C.3}$$

Therefore, $\mathbb{E}\left[x_m q_n^*\right] \approx 0$, $\forall m, n$ and hence $\mathbb{E}\left[\mathbf{x}\mathbf{q}^H\right] \approx \mathbf{0}$.

Appendix D

Linear model for two-bit regular ADCs

A fundamental difference between the standard and $\Sigma\Delta$ ADCs studied here is in selecting the output level $\alpha_{m'}$. For the case of $\Sigma\Delta$ ADCs, choosing an appropriate value for $\alpha_{m'}$ enabled us to control the amplitude of the input to the adjacent array element and is a crucial element in preventing the system from becoming unstable. However, in a standard ADC implementation, the output of the mth ADC is simply

$$y_m^{\mathrm{std}} = \mathcal{Q}_{m'}\left(\mathrm{Re}\left(x_m\right)\right) + j\,\mathcal{Q}_{m'}\left(\mathrm{Im}\left(x_m\right)\right), \tag{D.1}$$

where

$$\mathcal{Q}_{m'}\left(\mathrm{Re}\left(x_m\right)\right) = \frac{\sigma_{x_m}}{\sqrt{2}}\nu_i, \quad \text{if } x_m \in \left(\frac{\sigma_{x_m}}{\sqrt{2}}\nu_i^{\mathrm{lo}}, \frac{\sigma_{x_m}}{\sqrt{2}}\nu_i^{\mathrm{hi}}\right]. \tag{D.2}$$

As in the $\Sigma\Delta$ case, an element-wise Bussgang decomposition will be used and a linear model

for the output will be developed. More specifically,

$$y_m^{\text{std}} = \gamma_m x_m + q_m^{\text{std}}, \tag{D.3}$$

where previous definitions hold for γ_m and q_m^{std}, and the coefficients γ_m are not constrained to be 1. We can solve for γ_m to get

$$\gamma_m = \frac{\mathbb{E}\left[x_m \left(y_m^{\text{std}}\right)^*\right]}{\mathbb{E}\left[|x_m|^2\right]} = \sum_{i=2}^{4} \frac{(\nu_i - \nu_{i-1})}{\sqrt{2\pi}} \exp\left(-\frac{\left(\nu_i^{\text{lo}}\right)^2}{2}\right). \tag{D.4}$$

The resulting expression for γ_m is independent of m, so we define $\gamma \triangleq \gamma_m$. Finally, the output power and quantization noise powers are, respectively,

$$\sigma_{y_m^{\text{std}}}^2 = \frac{\sigma_{x_m}^2}{2} \sum_{i=1}^{4} \nu_i^2 \left(\Psi\left(\frac{\sigma_{x_m}}{\sqrt{2}}\nu_i^{\text{hi}}\right) - \Psi\left(\frac{\sigma_{x_m}}{\sqrt{2}}\nu_i^{\text{lo}}\right)\right),$$
$$\sigma_{q_m^{\text{std}}}^2 = \sigma_{y_m^{\text{std}}}^2 - \gamma^2 \sigma_{x_m}^2. \tag{D.5}$$

Let the ADC outputs be stacked in $\mathbf{y}^{\text{std}}$. Then, defining $\mathbf{C}_{q^{\text{std}}}$ as a diagonal matrix with $\sigma_{q_m^{\text{std}}}^2$ as its elements, the complete auto-correlation matrix of $\mathbf{y}^{\text{std}}$ is given by

$$\mathbf{C}_{y^{\text{std}}} = \gamma \mathbf{C}_x + \mathbf{C}_{q^{\text{std}}}. \tag{D.6}$$

The LMMSE channel estimate is then obtained by

$$\hat{\mathbf{g}}^{\text{std}} = \mathbf{C}_g \mathbf{\Phi}^H \mathbf{C}_{y^{\text{std}}}^{-1} \mathbf{y}^{\text{std}}. \tag{D.7}$$

Appendix E

Estimation error- Bartlett beamformer

The derivative of $f_{\mathrm{BF}}(\theta, \phi)$ evaluated at $[\theta_k, \phi_k]$ is given by

$$\left. \frac{\partial f_{\mathrm{BF}}(\theta, \phi)}{\partial \theta} \right|_{\theta=\theta_k} = -2\mathrm{Re}\left(\bar{\mathbf{g}}_k^\dagger \mathbf{W}^{-\frac{1}{2}} \hat{\mathbf{C}}_y \mathbf{W}^{-\frac{1}{2}} \mathbf{P}_{\bar{\mathbf{g}}_k}^\perp \bar{\mathbf{d}}_{\theta_k} \right). \tag{E.1}$$

Using (6.15) in the above equation and using the fact that $\bar{\mathbf{G}}^H \mathbf{P}_{\bar{\mathbf{g}}_k}^\perp \bar{\mathbf{d}}_{\theta_k} = \mathbf{0}$ due to the orthogonality assumption, we have

$$\left. \frac{\partial f(\theta, \phi)}{\partial \theta} \right|_{\theta=\theta_k} = -2\mathrm{Re}\left(\epsilon\sqrt{1-\epsilon^2}\, \mathbf{e}_k^T \mathbf{C}_s \tilde{\mathbf{A}}^H \mathbf{T}^H \mathbf{W}^{-\frac{1}{2}} \mathbf{P}_{\bar{\mathbf{g}}_k}^\perp \bar{\mathbf{d}}_{\theta_k} \right)$$
$$- 2\mathrm{Re}\left(\sqrt{1-\epsilon^2}\, \mathbf{e}_k^T \mathbf{C}_{sn} \mathbf{P}_{\bar{\mathbf{g}}_k}^\perp \bar{\mathbf{d}}_{\theta_k} \right) - 2\mathrm{Re}\left(\bar{\mathbf{g}}_k^\dagger \mathbf{W}_n \mathbf{P}_{\bar{\mathbf{g}}_k}^\perp \bar{\mathbf{d}}_{\theta_k} \right) \tag{E.2}$$

where we have ignored second-order error terms and $\mathbf{e}_k = [0, \ldots, 1, \ldots, 0]^T$ is a unit vector of length K with a 1 at the kth location. Then, let us define V_{1k}^θ, V_{2k}^θ and V_{3k}^θ as

$$
\begin{aligned}
V_{1k}^\theta &= -2\text{Re}\left(\epsilon\sqrt{1-\epsilon^2}\,\mathbf{e}_k^T\mathbf{C}_s\tilde{\mathbf{A}}^H\mathbf{T}^H\mathbf{W}^{-\frac{1}{2}}\mathbf{P}_{\bar{\mathbf{g}}_k}^{\perp}\bar{\mathbf{d}}_{\theta_k}\right) \\
V_{2k}^\theta &= -2\text{Re}\left(\sqrt{1-\epsilon^2}\,\mathbf{e}_k^T\mathbf{C}_{sn}\mathbf{P}_{\bar{\mathbf{g}}_k}^{\perp}\bar{\mathbf{d}}_{\theta_k}\right) \\
V_{3k}^\theta &= -2\text{Re}\left(\bar{\mathbf{g}}_k^\dagger\mathbf{W}_n\mathbf{P}_{\bar{\mathbf{g}}_k}^{\perp}\bar{\mathbf{d}}_{\theta_k}\right).
\end{aligned}
\tag{E.3}
$$

Further, we note that the expectation of each of the cross-terms in (E.2) is zero and make use of the following identities for arbitrary deterministic vectors $\mathbf{x}_1$, $\mathbf{x}_2$, $\mathbf{x}_3$ and $\mathbf{x}_4$ and for arbitrary scalars a and b [116]:

$$
\begin{aligned}
&2\text{Re}(a)\text{Re}(b) = \text{Re}\left(a^*b + ab\right) \\
&\mathbb{E}\left[\mathbf{x}_1^H\tilde{\mathbf{A}}\mathbf{x}_2\mathbf{x}_3^H\tilde{\mathbf{A}}\mathbf{x}_4\right] = 0 \\
&\mathbb{E}\left[\mathbf{x}_1^H\tilde{\mathbf{A}}^H\mathbf{x}_2\mathbf{x}_3^H\tilde{\mathbf{A}}\mathbf{x}_4\right] = \mathbf{x}_1^H\mathbf{x}_4\mathbf{x}_3^H\mathbf{x}_2 \\
\\
&\mathbb{E}\left[\mathbf{x}_1^H\tilde{\mathbf{C}}_{sn}\mathbf{x}_2\mathbf{x}_3^H\tilde{\mathbf{C}}_{sn}\mathbf{x}_4\right] = 0 \\
&\mathbb{E}\left[\mathbf{x}_1^H\tilde{\mathbf{C}}_{sn}^H\mathbf{x}_2\mathbf{x}_3^H\tilde{\mathbf{C}}_{sn}\mathbf{x}_4\right] = \frac{1}{T}\mathbf{x}_1^H\mathbf{x}_4\mathbf{x}_3^H\hat{\mathbf{C}}_s\mathbf{x}_2 \\
\\
&\mathbb{E}\left[\mathbf{x}_1^H\tilde{\mathbf{W}}_n\mathbf{x}_2\mathbf{x}_3^H\tilde{\mathbf{W}}_n\mathbf{x}_4\right] = \left(1 + \frac{\mu^2}{T}\right)\mathbf{x}_1^H\mathbf{x}_2\mathbf{x}_3^H\mathbf{x}_4 + \left(\frac{1}{T} + \mu^2\right)\mathbf{x}_3^H\mathbf{x}_2\mathbf{x}_1^H\mathbf{x}_4.
\end{aligned}
\tag{E.4}
$$

Then, $\mathbb{E}\left[V_{1k}^\theta V_{1k}^\theta\right]$, $\mathbb{E}\left[V_{2k}^\theta V_{2k}^\theta\right]$ and $\mathbb{E}\left[V_{3k}^\theta V_{3k}^\theta\right]$ can be evaluated to be

$$
\begin{aligned}
\mathbb{E}\left[V_{1k}^\theta V_{1k}^\theta\right] &= \\
&2\epsilon^2\left(1-\epsilon^2\right)\text{Re}\left(\mathbf{e}_k^T\mathbf{C}_s\mathbf{C}_s\mathbf{e}_k\bar{\mathbf{d}}_{\theta_k}^H\mathbf{P}_{\bar{\mathbf{g}}_k}^{\perp}\mathbf{W}^{-\frac{1}{2}}\mathbf{T}\mathbf{T}^H\mathbf{W}^{-\frac{1}{2}}\mathbf{P}_{\bar{\mathbf{g}}_k}^{\perp}\bar{\mathbf{d}}_{\theta_k}\right) \\
\mathbb{E}\left[V_{2k}^\theta V_{2k}^\theta\right] &= \frac{2}{T}\left(1-\epsilon^2\right)\text{Re}\left(\bar{\mathbf{d}}_{\theta_k}^H\mathbf{P}_{\bar{\mathbf{g}}_k}^{\perp}\bar{\mathbf{d}}_{\theta_k}\mathbf{e}_k^T\mathbf{C}_s\mathbf{e}_k\right) \\
\mathbb{E}\left[V_{3k}^\theta V_{3k}^\theta\right] &= 2\left(\frac{1}{T} + \mu^2\right)\text{Re}\left(\frac{\bar{\mathbf{d}}_{\theta_k}^H\mathbf{P}_{\bar{\mathbf{g}}_k}^{\perp}\bar{\mathbf{d}}_{\theta_k}}{\bar{\mathbf{g}}_k^H\bar{\mathbf{g}}_k}\right).
\end{aligned}
\tag{E.5}
$$

Computing the off-diagonal terms of $\mathbb{E}\left[\nabla f(\theta_k, \phi_k)\nabla f(\theta_k, \phi_k)^T\right]$ in a similar manner and taking the limit $T \to \infty$, we obtain $\mathbf{Q}_k$. For instance, the element $[\mathbf{Q}_k]_{11}$ is given by

$$[\mathbf{Q}_k]_{11} = 2\left(p_k + \frac{1}{\bar{\mathbf{g}}_k^H \bar{\mathbf{g}}_k}\right) \mathrm{Re}\left(\bar{\mathbf{d}}_{\theta_k}^H \mathbf{P}_{\bar{\mathbf{g}}_k}^\perp \bar{\mathbf{d}}_{\theta_k}\right) - 2\epsilon^2 p_k \mathrm{Re}\left(\bar{\mathbf{d}}_{\theta_k}^H \mathbf{P}_{\bar{\mathbf{g}}_k}^\perp \bar{\mathbf{d}}_{\theta_k}\right) + 2\frac{\mu^2}{\bar{\mathbf{g}}_k^H \bar{\mathbf{g}}_k} \mathrm{Re}\left(\bar{\mathbf{d}}_{\theta_k}^H \mathbf{P}_{\bar{\mathbf{g}}_k}^\perp \bar{\mathbf{d}}_{\theta_k}\right)$$

$$+ 2\epsilon^2 \left(1 - \epsilon^2\right) \mathrm{Re}\left(\mathbf{e}_k^T \mathbf{C}_s \mathbf{C}_s \mathbf{e}_k \bar{\mathbf{d}}_{\theta_k}^H \mathbf{P}_{\bar{\mathbf{g}}_k}^\perp \mathbf{W}^{-\frac{1}{2}} \mathbf{T}\mathbf{T}^H \mathbf{W}^{-\frac{1}{2}} \mathbf{P}_{\bar{\mathbf{g}}_k}^\perp \bar{\mathbf{d}}_{\theta_k}\right).$$

$$(\text{E.6})$$

Appendix F

Estimation error- MUSIC

The derivative of $f_{\mathrm{MU}}(\theta, \phi)$ evaluated at $[\theta_k, \phi_k]$ is given by

$$\frac{\partial f_{\mathrm{MU}}(\theta, \phi)}{\partial \theta}\bigg|_{\theta=\theta_k} = 2\mathrm{Re}\left(\bar{\mathbf{d}}_{\theta_k}^H \mathbf{P}_{\bar{\mathbf{g}}_k}^{\perp} \hat{\mathbf{E}}_n \hat{\mathbf{E}}_n^H \left(\bar{\mathbf{g}}_k^{\dagger}\right)^H\right). \tag{F.1}$$

Since $\hat{\mathbf{E}}_n \hat{\mathbf{E}}_n^H = \mathbf{I}_{MN} - \hat{\mathbf{E}}_s \hat{\mathbf{E}}_s^H$ and $\mathbf{P}_{\bar{\mathbf{g}}_k}^{\perp} \mathbf{E}_s = \mathbf{0}$, we have $\mathbf{P}_{\bar{\mathbf{g}}_k}^{\perp} \hat{\mathbf{E}}_s = \mathcal{O}(1/\sqrt{MN})$ and

$$\frac{\partial f_{\mathrm{MU}}(\theta, \phi)}{\partial \theta}\bigg|_{\theta=\theta_k} = -2\mathrm{Re}\left(\bar{\mathbf{d}}_{\theta_k}^H \mathbf{P}_{\bar{\mathbf{g}}_k}^{\perp} \hat{\mathbf{E}}_s \mathbf{E}_s^H \left(\bar{\mathbf{g}}_k^{\dagger}\right)^H\right). \tag{F.2}$$

Using the first-order relationship between $\mathbf{E}_s$ and $\mathbf{W}_n^{-\frac{1}{2}} \mathbf{C}_y \mathbf{W}_n^{-\frac{1}{2}}$ [117]

$$\mathbf{P}_{\bar{\mathbf{g}}_k}^{\perp} \hat{\mathbf{E}}_s \approx \mathbf{P}_{\bar{\mathbf{g}}_k}^{\perp} \mathbf{W}_n^{-\frac{1}{2}} \hat{\mathbf{C}}_y \mathbf{W}_n^{-\frac{1}{2}} \mathbf{E}_s \tilde{\mathbf{\Lambda}}^{-1}$$

we get

$$\frac{\partial f_{\mathrm{MU}}(\theta, \phi)}{\partial \theta}\bigg|_{\theta=\theta_k} = -2\mathrm{Re}\left(\bar{\mathbf{d}}_{\theta_k}^H \mathbf{P}_{\bar{\mathbf{g}}_k}^{\perp} \mathbf{W}_n^{-\frac{1}{2}} \hat{\mathbf{C}}_y \mathbf{W}_n^{-\frac{1}{2}} \mathbf{E}_s \tilde{\mathbf{\Lambda}}^{-1} \mathbf{E}_s^H \left(\bar{\mathbf{g}}_k^{\dagger}\right)^H\right). \tag{F.3}$$

As in the beamforming case, we can plug in the expression for $\mathbf{W}_n^{-\frac{1}{2}}\hat{\mathbf{C}}_y\mathbf{W}_n^{-\frac{1}{2}}$ and ignore second-order terms to get

$$
\begin{aligned}
\left.\frac{\partial f_{\mathrm{MU}}\left(\theta,\phi\right)}{\partial\theta}\right|_{\theta=\theta_k} &= -2\mathrm{Re}\left(\bar{\mathbf{d}}_{\theta_k}^H\mathbf{P}_{\bar{\mathbf{g}}_k}^{\perp}\mathbf{W}_n^{-\frac{1}{2}}\hat{\mathbf{C}}_y\mathbf{W}_n^{-\frac{1}{2}}\mathbf{E}_s\tilde{\boldsymbol{\Lambda}}^{-1}\mathbf{E}_s^H\left(\bar{\mathbf{g}}_k^{\dagger}\right)^H\right) \\
&= -2\mathrm{Re}\left(\bar{\mathbf{d}}_{\theta_k}^H\mathbf{P}_{\bar{\mathbf{g}}_k}^{\perp}\left[\epsilon\sqrt{1-\epsilon^2}\mathbf{W}_n^{-\frac{1}{2}}\mathbf{T}\tilde{\mathbf{A}}\mathbf{C}_s\bar{\mathbf{G}}^H + \sqrt{1-\epsilon^2}\,\mathbf{C}_{sn}^H\bar{\mathbf{G}}^H + \mathbf{W}_n\right]\mathbf{E}_s\tilde{\boldsymbol{\Lambda}}^{-1}\mathbf{E}_s^H\left(\bar{\mathbf{g}}_k^{\dagger}\right)^H\right).
\end{aligned}
\tag{F.4}
$$

Again, defining V_{1k}^{θ}, V_{2k}^{θ} and V_{3k}^{θ} as

$$
\begin{aligned}
V_{1k}^{\theta} &= -2\mathrm{Re}\left(\epsilon\sqrt{1-\epsilon^2}\bar{\mathbf{d}}_{\theta_k}^H\mathbf{P}_{\bar{\mathbf{g}}_k}^{\perp}\mathbf{W}_n^{-\frac{1}{2}}\mathbf{T}\tilde{\mathbf{A}}\mathbf{C}_s\bar{\mathbf{G}}^H\mathbf{E}_s\tilde{\boldsymbol{\Lambda}}^{-1}\mathbf{E}_s^H\left(\bar{\mathbf{g}}_k^{\dagger}\right)^H\right) \\
V_{2k}^{\theta} &= -2\mathrm{Re}\left(\bar{\mathbf{d}}_{\theta_k}^H\mathbf{P}_{\bar{\mathbf{g}}_k}^{\perp}\mathbf{W}_n\mathbf{E}_s\tilde{\boldsymbol{\Lambda}}^{-1}\mathbf{E}_s^H\left(\bar{\mathbf{g}}_k^{\dagger}\right)^H\right), \\
V_{3k}^{\theta} &= -2\mathrm{Re}\left(\sqrt{1-\epsilon^2}\bar{\mathbf{d}}_{\theta_k}^H\mathbf{P}_{\bar{\mathbf{g}}_k}^{\perp}\mathbf{C}_{sn}^H\bar{\mathbf{G}}^H\mathbf{E}_s\tilde{\boldsymbol{\Lambda}}^{-1}\mathbf{E}_s^H\left(\bar{\mathbf{g}}_k^{\dagger}\right)^H\right)
\end{aligned}
\tag{F.5}
$$

we can compute $\mathbb{E}\left[V_{1k}^{\theta}V_{1k}^{\theta}\right]$, $\mathbb{E}\left[V_{2k}^{\theta}V_{2k}^{\theta}\right]$ and $\mathbb{E}\left[V_{3k}^{\theta}V_{3k}^{\theta}\right]$ in a manner similar to (E.4) - (E.5) by using (6.29)

$$
\begin{aligned}
\mathbb{E}\left[V_{1k}^{\theta}V_{1k}^{\theta}\right] &= 2\epsilon^2\left(1-\epsilon^2\right)\mathrm{Re}\left(\bar{\mathbf{d}}_{\theta_k}^H\mathbf{P}_{\bar{\mathbf{g}}_k}^{\perp}\mathbf{W}^{-\frac{1}{2}}\mathbf{T}\mathbf{T}^H\mathbf{W}^{-\frac{1}{2}}\mathbf{P}_{\bar{\mathbf{g}}_k}^{\perp}\bar{\mathbf{d}}_{\theta_k}\mathbf{b}_k^H\tilde{\boldsymbol{\Lambda}}^{-1}\boldsymbol{\Lambda}_s\mathbf{B}^H\mathbf{B}\boldsymbol{\Lambda}_s\tilde{\boldsymbol{\Lambda}}^{-1}\mathbf{b}_k\right) \\
\mathbb{E}\left[V_{2k}^{\theta}V_{2k}^{\theta}\right] &= \tilde{\mu}^2\mathrm{Re}\left(\bar{\mathbf{d}}_{\theta_k}^H\mathbf{P}_{\bar{\mathbf{g}}_k}^{\perp}\bar{\mathbf{d}}_{\theta_k}\mathbf{b}_k^H\tilde{\boldsymbol{\Lambda}}^{-2}\mathbf{b}_k\right) \\
\mathbb{E}\left[V_{3k}^{\theta}V_{3k}^{\theta}\right] &= 2(1-\epsilon^2)\mathrm{Re}\left(\bar{\mathbf{d}}_{\theta_k}^H\mathbf{P}_{\bar{\mathbf{g}}_k}^{\perp}\bar{\mathbf{d}}_{\theta_k}\mathbf{b}_k^H\tilde{\boldsymbol{\Lambda}}^{-1}\boldsymbol{\Lambda}_s\tilde{\boldsymbol{\Lambda}}^{-1}\mathbf{b}_k\right),
\end{aligned}
\tag{F.6}
$$

where $\mathbf{b}_k$ is the kth column of $\mathbf{B}$.

Appendix G

Estimation error- ULAs

We use the following well-known sums of finite power series:

$$
\begin{aligned}
\sum_{k=1}^{n} k a^{k} &= \frac{1 - (n+1)a^{n} + na^{n+1}}{(1-a)^{2}} \\
\sum_{k=1}^{n} k^{2} a^{k} &= \frac{a + a^{2} - (n+1)^{2}a^{n+1} + (2n^{2} + 2n - 1)a^{n+2} - n^{2}a^{n+3}}{(1-a)^{3}}.
\end{aligned}
\tag{G.1}
$$

For the sake of convenience, we will also define $\omega = \exp\left(j2\pi d\sin(\theta)/\lambda\right)$. Subsequently, the term $\bar{\mathbf{g}}^{H}\bar{\mathbf{g}} = \mathbf{a}^{H}\left(\theta\right)\mathbf{W}_{n}^{-1}\mathbf{a}\left(\theta\right)$ can be represented by the sum

$$
\begin{aligned}
&\mathbf{a}^{H}\left(\theta\right)\mathbf{W}_{n}^{-1}\mathbf{a}\left(\theta\right) \\
&= \frac{1}{\lambda_{q}^{2}(1 + 2\sigma_{q}^{2})}\left(\sum_{m=1}^{N}\left(\sum_{k=1}^{m-1} l_{q}^{k}\,\omega^{-k} + \sum_{k=1}^{N-m} l_{q}^{k}\,\omega^{k}\right) + N\right) \\
&= \frac{1}{\lambda_{q}^{2}(1 + 2\sigma_{q}^{2})}\left(N + \sum_{m=1}^{N}\left(\frac{l_{q}\omega^{-1} - l_{q}^{m}\omega^{-m}}{1 - l_{q}\omega^{-1}} + \frac{l_{q}\omega - l_{q}^{N-m+1}\omega^{N-m+1}}{1 - l_{q}\omega}\right)\right) \\
&\approx \frac{N}{\lambda_{q}^{2}(1 + 2\sigma_{q}^{2})}\left(1 + \frac{2l_{q}\cos\left(2\pi d\sin\theta/\lambda\right) - 2l_{q}^{2}}{1 - 2l_{q}\cos\left(2\pi d\sin\theta/\lambda\right) + l_{q}^{2}}\right),
\end{aligned}
\tag{G.2}
$$

where we ignore the higher powers of l_q since $|l_q| < 1$. We evaluate the remaining terms in a similar manner.

$$\mathbf{d}^H(\theta)\mathbf{W}_n^{-1}\mathbf{a}(\theta)$$

$$= \frac{j2\pi d\cos\theta/\lambda}{\lambda_q^2(1+2\sigma_q^2)}\left(\frac{N(N-1)}{2} + \sum_{m=1}^{N}\left((m-1)\sum_{k=1}^{m-1}l_q^k\omega^{-k} + (m-1)\sum_{k=1}^{N-m}l_q^k\omega^k - \sum_{k=1}^{m-1}kl_q^k\omega^{-k} + \sum_{k=1}^{N-m}kl_q^k\omega^k\right)\right),$$

where

$$\sum_{m=1}^{N}(m-1)\sum_{k=1}^{m-1}l_q^k\omega^{-k} \approx \frac{N(N-1)}{2}\frac{l_q\omega^{-1}}{1-l_q\omega^{-1}},$$

$$\sum_{m=1}^{N}(m-1)\sum_{k=1}^{N-m}l_q^k\omega^k \approx \frac{N(N-1)}{2}\frac{l_q\omega}{1-l_q\omega},$$

$$\sum_{m=1}^{N}\sum_{k=1}^{m-1}kl_q^k\omega^{-k} \approx \frac{Nl_q\omega^{-1}}{(1-l_q\omega^{-1})^2}$$

$$\sum_{m=1}^{N}\sum_{k=1}^{N-m}kl_q^k\omega^k \approx N\frac{l_q\omega}{(1-l_q\omega)^2}$$

Lastly, following an approach similar to the above, we evaluate $\mathbf{d}^H(\theta)\mathbf{W}_n^{-1}\mathbf{d}(\theta)$ to get

$$\mathbf{d}^H(\theta)\mathbf{W}_n^{-1}\mathbf{d}(\theta) \approx \frac{(2\pi d\cos\theta/\lambda)^2}{\lambda_q^2(1+2\sigma_q^2)}\frac{N(N-1)(2N-1)}{6}\left(\frac{l_q\omega^{-1}}{(1-l_q\omega^{-1})} + \frac{l_q\omega}{(1-l_q\omega)} + 1\right). \quad \text{(G.3)}$$

Finally, using the equations (G.2)-(G.3) in (6.35), we obtain the result for the estimation error in (6.38).

Appendix H

Estimation error- Reg. ADCs

In this section, we derive the variance of the beamformer applied to the output of regular ADC quantizers. The element-wise Bussgang decomposition [103, 148] is applied in a similar manner to standard one- and two-bit ADCs. Then, denoting the output power and the quantization noise power of the regular quantized array by $\sigma_{y,r}^2$ and $\sigma_{q,r}^2$, respectively, we have

$$
\sigma_{y,r}^2 = \begin{cases} \frac{\pi}{2}\sigma_x^2, & b = 1, \\ \\ \sigma_x^2 \sum_{i=1}^{4} \nu_i^2 \left(\Psi\left(\frac{\sigma_x}{\sqrt{2}}\nu_i^{\mathrm{hi}} \right) - \Psi\left(\frac{\sigma_x}{\sqrt{2}}\nu_i^{\mathrm{lo}} \right) \right), & b = 2 \end{cases}
$$

$$
\sigma_{q,r}^2 = (k_r' - 1)\sigma_x^2
$$

$$
k_r' = \begin{cases} \pi/2,\ b = 1 \\ \sum_{i=1}^{4} \nu_i^2 \left(\Psi\left(\frac{\sigma_x}{\sqrt{2}}\nu_i^{\mathrm{hi}} \right) - \Psi\left(\frac{\sigma_x}{\sqrt{2}}\nu_i^{\mathrm{lo}} \right) \right),\ b = 2. \end{cases}
$$

(H.1)

Consequently, the equivalent additive plus quantization noise covariance matrix in the presence of mutual coupling is given by

$$\mathbf{W}_{n,r} = \mathbf{C}_n + (k'_r - 1)\sigma_x^2 \mathbf{I}_N. \tag{H.2}$$

The variance of the estimator is then given by (6.35) by plugging in $\mathbf{W}_{n,r}$ in place of $\mathbf{W}_n$. However, we will carry out the analysis similar to that in Appendix G for the simple case of negligible mutual coupling. For large N, (6.35) then becomes

$$\mathbb{E}\left[\hat{\theta} - \theta\right]^2 = \frac{(1 + (k'_r - 1)\sigma_x^2)}{2T\rho\left(\mathbf{d}^H(\theta)\mathbf{d}(\theta) - \frac{|\mathbf{d}^H(\theta)\mathbf{a}(\theta)|^2}{N}\right)} \approx \frac{(1 + (k'_r - 1)\sigma_x^2)}{\rho T\left(\frac{2\pi d\cos\theta}{\lambda}\right)^2 \frac{N^3}{6}} \tag{H.3}$$

Finally, the variance of the beamformer for the unquantized case is given by [142, 154]

$$\mathbb{E}\left[\hat{\theta} - \theta\right]^2 \approx \frac{1}{\rho T\left(\frac{2\pi d\cos\theta}{\lambda}\right)^2 \frac{N^3}{6}}. \tag{H.4}$$

The error floor in each case can be computed by setting $\sigma_x^2 = \rho$ and taking the limit $\rho \to \infty$. For standard quantization, the estimation error floor can be computed from (H.3) to get

$$\lim_{\rho \to \infty} \mathbb{E}\left[\hat{\theta} - \theta\right]^2 = \frac{(k'_r - 1)}{T\left(\frac{2\pi d\cos\theta}{\lambda}\right)^2 \frac{N^3}{6}}. \tag{H.5}$$

For ideal resolution, $\lim_{\rho \to \infty} \mathbb{E}\left[\hat{\theta} - \theta\right]^2 = 0$.